
**PHOTO-FRAGMENTATION AND
ELECTRON-DETACHMENT STUDIES OF
GAS-PHASE CHROMOPHORE IONS**



Dennis Bo Rahbek

Department of Physics and Astronomy
University of Aarhus, Denmark

PhD Thesis
July 2012

Contents

Preface	iii
Acknowledgements	iii
List of publications	v
Abstract	ix
Dansk Resume	xi
Outline of the thesis	xiii
1 Introduction	1
2 Experimental techniques	7
2.1 Ion production and trapping	8
2.2 ELISA	9
2.3 Detection systems	11
2.3.1 Laser systems	12
2.4 Experimental procedures - ELISA	13
2.4.1 Power dependence	15
2.4.2 Absorption spectroscopy	16
2.5 Photo-electron spectroscopy - SEPII	17
2.5.1 Detection systems and laser systems	21
2.5.2 Experimental procedures	21
3 Computational methods	25
3.1 Density functional theory	26
3.2 Time dependent density functional theory	27
3.3 The GAUSSIAN package	28

4	The photoactive yellow protein	29
4.1	Introduction	29
4.2	Absorption experiments	32
4.2.1	Experimental details	32
4.2.2	Results	34
4.2.3	Discussion	35
4.3	Photo-detachment experiments	44
4.3.1	Experimental details	44
4.3.2	Results	47
4.3.3	Discussion	50
4.4	Conclusion	54
5	The green fluorescent protein	57
5.1	Introduction	57
5.2	Photo-detachment experiments	61
5.2.1	Experimental details	61
5.2.2	Results	62
5.2.3	Discussion	63
5.3	Absorption experiments	66
5.3.1	Experimental details	66
5.4	Absorption experiments - Cations	67
5.4.1	Power dependences	67
5.4.2	Action absorption spectra	69
5.4.3	Discussion	71
5.5	Absorption experiments - Anions	74
5.5.1	Power dependences	74
5.5.2	Action absorption spectra	75
5.5.3	Discussion	78
5.6	Conclusion	83
6	Conclusion and outlook	85
	References	89

Preface

This thesis has been submitted to the Graduate School of Science and Technology at Aarhus University, Denmark, in order to fulfil the requirements for the PhD-degree. The work presented in this thesis has been performed under the supervision of Prof. Lars H. Andersen at Department of Physics and Astronomy, Aarhus University, in the period from August 2009 to August 2012.

Acknowledgements

Without the support and help of a large number of persons the work presented in this thesis would not have been possible. I would like to use this opportunity to acknowledge the people, whose assistance I have profited from and the people whom I have worked together with.

First and foremost, I would like to thank my supervisor Lars H. Andersen for giving me the opportunity to continue my studies of biomolecules as a PhD student. He has always taken the time to discuss the experimental results and to give a hand in the laboratory when needed.

Next, I highly appreciate the time Jyoti has spent in training and educating me in the art of experimental physics. I really appreciate our many hours together, both in the laboratory and in lunch breaks. On this note, I would like to thank Benedikte, Yoni and Hjalte. I really appreciate the countless hours we have spent in the lab together working on our projects. The last three years would not have been the same without you guys.

The interpretation of the experimental results have been taken to a different level through the discussions with Anastacia. I highly appreciate our many rewarding discussions on both experimental and theoretical results.

A thanks to Steen for always having the door open and for his willingness to discuss problems of both practical and theoretical nature.

At times when things in the laboratories were not behaving, I have benefited greatly by the expertise of Kristian and Annette. I'm grateful for the time they have spent helping me out with problems of all sorts.

I cannot keep track of the times I have needed the expertise and help from the workshops: electronic, mechanical, and vacuum lab. It is invaluable for an experimentalist to have such helpful, competent people around.

For some of my projects I have had the possibility of using the Grendel cluster at Danish Center for Scientific Computing, Aarhus University. Without this access these calculations would not have been possible for me to perform.

Most of the chromophore samples have been synthesized by international collaborators: M. B. Nielsen, M. Sheves and K. Solntsev. Without their expertise the project would not have been the same. On this note I would like to thank our many international collaborators who have contributed with ideas and taken part in discussions.

For three months, I had the pleasure of visiting the group of Mathias Weber at JILA in Boulder, Colorado. It was a good experience for me to do research in a quite different topic. I appreciate this opportunity and the daily discussions with Mathias. I would like to thank the members of the group: Sydney, Ben, and Casey, for making me part of their lives. It was always great fun to go for lunch or for a beer after work with you guys.

The mornings would not have been the same without the early morning coffee with Maj-Britt, Lisbeth, Benedikte, Kristian, Anette, Anne and Christian. I could not think of a better way of beginning a day at work.

I would like to thank my family and friends for their support during the years and for taking my head off my project.

Finally, a special thanks to Benedikte, Lisbeth, Yoni and Hjalte for proof-reading this manuscript at different stages in the process, for listening to my nonsense in good and bad times I'm going to miss working close to you.

List of publications

This thesis is based on the following work:

- I. T. Rocha-Rinza, O. Christiansen, **D. B. Rahbek**, B. Klærke, L. H. Andersen, K. Lincke, and M. B. Nielsen,
Spectroscopic Implications of the Electron Donor-Acceptor Effect in the Photoactive Yellow Protein Chromophore
Chem. Eur. J. **16**, 11977 (2010)
- II. Y. Toker, **D. B. Rahbek**, B. Klærke, A. V. Bochenkova, and L. H. Andersen,
Direct and indirect electron emission from the green fluorescent protein chromophore
Accepted to Phys. Rev. Lett.
- III. **D. B. Rahbek**, Y. Toker, A. V. Bochenkova, B. Klærke, and L. H. Andersen,
Electronic dynamics in photo-detachment channels of the PYP chromophore probed by photo-electron spectroscopy
In preparation
- IV. A. V. Bochenkova, J. Rajput, **D. B. Rahbek**, B. Klærke, and L. H. Andersen,
Nuclei versus electrons: a striking ultrafast dual photoresponse of biochromophores prompted by nature
Submitted to Nature Chemistry
- V. **D. B. Rahbek**, B. Klærke, Y. Toker, A. V. Bochenkova, and L. H. Andersen,
Inhomogeneous broadening in spectral shapes of the protonated GFP chromophores: para- versus meta-effects
In preparation

During my PhD-studies, I have furthermore performed a number of other experiments. These will lead to the following publications, but will not be discussed in this thesis:

- VI. B. Klærke, Y. Toker, **D. B. Rahbek**, L. Hornekær, and L. H. Andersen
Formation and stability of hydrogenated PAHs in the gas-phase
Accepted to Astronomy & Astrophysics

- VII. Y. Toker, **D. B. Rahbek**, H. V. Kiefer, J. Rajput, P. Dugourd, S. Brønsted Nielsen, A. V. Bochenkova and L.H. Andersen
Specificity in the fragmentation of the Retinal protonated Schiff-base chromophore
In preparation
- VIII. Y. Toker, **D. B. Rahbek**, B. Klærke, J. Rajput, A. V. Bochenkova, and L. H. Andersen
Photo-absorption and photo-electron spectra of the meta-HBDI chromophore
In preparation

Before my time as PhD-studies, I did my master's project within the same field. This work has resulted in the following publications:

- IX. T. Rocha-Rinza, O. Christiansen, J. Rajput, A. Gopalan, **D. B. Rahbek**, L. H. Andersen, A. V. Bochenkova, A. A. Granovsky, K. B. Bravaya, A. V. Nemukhin, K. L. Christiansen, and M. B. Nielsen,
Gas Phase Absorption Studies of Photoactive Yellow Protein Chromophore Derivatives
J. Phys. Chem. A **113**, 9442 (2009)
- X. J. Rajput, **D. B. Rahbek**, L. H. Andersen, T. Rocha-Rinza, O. Christiansen, K. B. Bravaya, A. V. Erokhin, A. V. Bochenkova, K. M. Solntsev, J. Dong, J. Kowalik, L. M. Tolbert, M. Å. Petersen, and M. B. Nielsen,
Photoabsorption studies of neutral green fluorescent protein model chromophores in vacuo
Phys. Chem. Chem. Phys. **11**, 9996 (2009)
- XI. K. Lincke, T. Sølling, L. H. Andersen, B. Klærke, **D. B. Rahbek**, J. Rajput, C. B. Oehlenschläger, M. Å. Petersen, and M. B. Nielsen,
On the absorption of the phenolate chromophore in the green fluorescent protein-role of individual interactions
Chem. Commun. **46**, 734 (2010)
- XII. G. Aravind, R. Antoine, B. Klærke, J. Lemoine, **D. B. Rahbek**, J. Rajput, P. Dugourd, and L. H. Andersen,
Sub-microsecond photodissociation pathways of gas phase adenosine 5'-monophosphate nucleotide ions
Phys. Chem. Chem. Phys. **12**, 3486 (2010)

- XIII. J. Rajput, **D. B. Rahbek**, G. Aravind, and L. H. Andersen,
Spectral Tuning of the Photoactive Yellow Protein Chromophore by H-Bonding
Biophys. J. **98**, 488 (2010)
- XIV. J. Rajput, **D. B. Rahbek**, L. H. Andersen, A. Hirshfeld, M. Sheves,
P. Altoè, G. Orlandi, and M. Garavelli
Probing and Modeling the Absorption of Retinal Protein Chromophores in Vacuo
Angew. Chem. Int. Ed. **49**, 1790 (2010)

Abstract

During my time as a PhD-student I have worked on increasing our knowledge of biologically relevant photoactive proteins. More specifically, I have studied chromophores that are found within some of these proteins. Upon absorbing a photon, the chromophore initiates a process within the protein. Depending on the function of the protein, this may result in human vision, emission of light at a higher wavelength, fluorescence, or harvesting of energy used as an energy source by bacteria, algae or plants.

The interaction between these chromophores and the surrounding protein is crucial for fine-tuning the absorption properties of the chromophore to match specific tasks. I have taken part in studying this by mimicking specific interactions by chemically altering the chromophore and observing the effect on the photo-physical properties. The work presented in this thesis deals with studying the photo-physical properties of two important bio-chromophores by investigating the properties of structural isomers of these molecules. The chromophores are the ones found in the green fluorescent protein and the photoactive yellow protein. The photo-physical properties have been studied experimentally in the gas phase by using action spectroscopy and photoelectron spectroscopy.

From the experimental results, we have realized that these two chromophores in the deprotonated form have important common photo-physical properties. For both models it is shown that the vertical detachment energy lies slightly above the vertical excitation energy. This results in a competition between de-excitation by internal conversion and electron emission. Both of these processes are of non-adiabatic character as they rely on coupling between electronic energy and energy in nuclear motion. Moreover, it is found that higher-lying states in the anionic forms serves as 'doorway'-states into the continuum of the neutral radical.

Regarding the structural isomeric forms of each of the chromophores

we find that the degree of electronic coupling between the subunits making up the chromophores is crucial for the tuning the absorption properties, both in terms of oscillator strength and excitation energies. Interestingly, the effects are similar for both of the chromophore families.

Dansk Resume

I min tid som Ph.D.-studerende har jeg arbejdet med at udvide vores viden omkring biologisk relevante fotoaktive proteiner. Mere specifikt har jeg studeret kromoforen fra nogle af disse proteiner. Når kromoforen, som er den lysfølsomme del af proteinet, absorberer en foton, så startes en proces i proteinet. Afhængig af proteinets funktion kan dette resultere i den proces der gør mennesket i stand til at se, emission af lys ved en længere bølgelængde, fluorescens, eller opsamling af energy til brug som energikilde for bakterier, algere eller planter.

Vekselvirkningen mellem disse kromoforer og det omsluttende protein er essentiel for at finjustere absorptionsegenskaberne. Jeg har taget del i at undersøge dette ved at efterligne specifikke vekselvirkninger, hvilket kan gøres ved at ændre kromoforerne kemisk og undersøge de fotofysiske effekter af dette. Denne afhandling omhandler studier af de fotofysiske egenskaber for to vigtige bio-kromoforer ved at undersøge egenskaber af flere af deres strukturelle isomerer. Disse to kromoforer findes i henholdsvis det grønne fluorescerende protein og det fotoaktive gule protein. Deres fotofysiske egenskaber i gas fase er blevet undersøgt eksperimentelt ved to forskellige opstillinger på Institut for Fysik og Astronomi, Aarhus Universitet. Egenskaberne er blevet studeret ved at observere de neutrale fragmenter efter absorption samt elektroner udsendt som følge af absorption.

Fra de eksperimentelle resultater har vi erfaret, at disse to kromoforer i deres deprotonerede form udviser vigtige fælles fotofysiske egenskaber. For begge modeller ligger den vertikale frigørelsesenergi umiddelbart over den vertikale eksitationsenergi. Dette resulterer i en konkurrence mellem intern omdannelse og udsendelse af en elektron. Begge disse processer er af ikke-adiabatisk karakter, eftersom de afhænger af koblingen mellem elektronisk energi og energi fra kernebevægelse. Ydermere er det fundet at

højereliggende tilstande i de anioniske former virker som åbningstilstande udi kontinuetsfor den neutrale radikal.

Angående de strukturelle isomerer for hver af de to kromoforer, så har vi vist, at graden af afkobling mellem de to undersystemer, der udgør kromoforen, er essentiel for fintuning af absorptionsegenskaberne. Det gør sig gældende for både oscillatorstyrken for overgangene og eksitationsenergiene. Interessant nok er effekterne ens for de to kromoforer.

Outline of the thesis

Chapter 1 introduces the field of photoactive proteins together with some important terms. The importance of studying the light-absorbing units of these proteins with the main focus on gas-phase experiments is discussed.

Chapter 2 presents the two experimental techniques employed in this work in order to obtain action absorption and photo-electron spectra for the gas phase chromophore ions. The electro-spray ionization technique used for producing gas phase ions is described, followed by an introduction to the experimental setups at the ELeCtrostatic Ion Storage ring in Aarhus and the photo-electron spectrometer at Separator II.

Chapter 3 deals with the experimental results from the experiments on model chromophores for the photoactive yellow protein. That is, the action absorption spectra of three anionic structural isomers are presented and discussed. Photo-electron spectra at several wavelengths of one of the isomers are hereafter presented and compared.

Chapter 4 is devoted to experiments on two structural isomers modelling the chromophore from the green fluorescent protein. Action absorption spectra of anionic and cationic forms of both isomers are presented and discussed. Photo-electrons were also measured at several wavelengths and these results are introduced and discussed.

Chapter 5 concludes the experimental results and the discussion hereof. Furthermore it serves as an outlook to possible future experiments.

Chapter 6 shortly summarizes the thesis.

CHAPTER 1

Introduction

That light has had quite a large influence on life on Earth and still has, can hardly be news to anyone. In old days many people worshipped the sun, in Egypt for instance the sun was prayed to through Ra, the sun-God. Nowadays, we may not make sacrifices to a sun-God in the same direct manner, instead the 'worship' for many has moved from the temples to the beaches, however, we all know that it affects life on Earth. Children in elementary school are taught that plants need sunlight in order to grow, every spring the media remind us to wear sunscreen to protect our skin from UV-radiation from the sun and in nature, the effect of the sunlight is on a larger scale seen in the changing of the seasons.

The sunlight is utilized in a myriad of ways in nature. Many flowers produce pigments that absorb parts of the visible spectrum leaving the petals in a colourful display to attract insects, all in order for the flowers to get their pollen spread. Many animals, in a similar manner produce pigments, to display colours in order to attract mates, to serve as camouflage or simply to scare off predators. However, for many people photosynthesis is probably the most obvious process if asked how light affects and is used in nature. In photosynthesis, the light is harvested and transferred into chemical energy used for plants and algae to grow. In plants and algae the light is primarily absorbed by the pigment chlorophyll, but also other light-absorbers like carotenoids are important. Furthermore, smaller living organisms, like some bacteria, also harvest sunlight. Some types of halobacteria harvest light from one part of the solar spectrum, while at the same time using other light antennas in the UV-range as a warning system against photo-damage.

The light, either for gathering energy for chemical processes or for initiating a specific action, is absorbed by photoactive proteins. It is not the whole protein as such, that is sensitive to light in a given wavelength range, more specifically it is a small part of the protein, called the chromophore, that absorbs the light. There are many different 'families' of molecules that act as chromophores in photoactive proteins. However, the same specific chromophore can be responsible for absorption of light. Three proteins are responsible for absorbing blue, green and red light, however they all contain the same chromophore, retinal. Thus the electronic properties of the chromophore are affected differently by the specific interactions in each of the proteins. Among the interactions are: electric charges on nearby amino acids, hydrogen bonds to nearby amino acids or water molecules and steric constraints.

Besides tuning the absorption properties of the chromophore, the above mentioned interactions may also affect the potential energy surfaces of the chromophore leading to specific processes upon light absorption. In the case of the chromophore from the photoactive yellow protein (PYP), excitation for instance leads to an isomerization process initiating a partly unfolding and refolding of the protein. This process ultimately serves to signal to the surrounding bacterium, that blue light has been absorbed, which drives the bacterium to move away - a process called negative phototaxis. In a similar manner, the chromophore found in the green fluorescent protein (GFP), also undergo isomerization upon excitation. However, for GFP this isomerization process is followed by emission of light at a slightly higher wavelength - fluorescence.

Altering the protein surroundings of the chromophore is one method of changing its absorption properties. Another effective way is by slightly modifying the chromophore itself. In this manner the photo-physical properties can be altered drastically. The family of fluorescent proteins of which the green fluorescent protein is the best known is a good example for this. The properties of this family of absorbers are not only perturbed and fine-tuned by the surroundings, but also by changes in the amino acid chain that constitutes the protein. In this manner the whole range of visible light is covered by different fluorescent proteins.

Changing the amino acid chain making up a protein, in order to adjust the environment around the chromophore, is one of the methods used by scientists to gain understanding of the functioning of the photoactive proteins, and this method is actually used to design proteins with desired properties [1–7]. However, these proteins are fairly large and complex sys-

tems, which makes the full proteins a difficult starting point if the properties of the bare chromophores are to be fully understood.

Instead, in order to gain knowledge of the photo-physical properties of the proteins, it is convenient to begin by studying smaller systems - the chromophores themselves. Experiments on a large number of these biochromophores are being performed with different techniques in a large variety of solvents [8–14]. Unfortunately, the solvent influences the chromophore, and these interactions is difficult to account for properly. A method to study the absorption properties and state-specific dynamics of these specific molecules, with and without protein interactions, is by computational methods [15–21]. With increasing computer power and development of new and improved methods, the accuracy has improved considerably during the last decade, however, it is nonetheless still a time-consuming process. Moreover, the theoretical methods all include several simplifications and assumptions necessary to lower the computational costs. Because of all these approximations, care has to be taken when concluding on the basis of calculations. Thus, in order to study the intrinsic properties of these chromophores, you need to truly isolate the individual chromophore in the experiments, to keep it free of any interactions. This can be achieved by transferring the chromophores to the gas phase.

Performing gas phase experiments is not trivial. In solution phase the concentration of absorbing units can be kept high enough, that experiments can be performed and evaluated on the basis of Lambert-Beers law. The concentration of absorbers in gas phase is much smaller, hence, it is practically impossible to measure absorption directly by the decrease in photon number. This is overcome by observing the outcome of absorption: emitted electrons, neutral or charged fragments or light - a method termed action spectroscopy.

The outcome of an absorption event depends on the energy of the photon and the properties of the chromophore ion. For cations, where emission of an electron generally requires higher energy than one or two visible photons contain, the action is most likely to be fragmentation. That is, the singly charged ion dissociates into a neutral and a charged fragment. Upon photon absorption, the chromophore is left in an excited state, from which it usually falls back into the ground state, through internal conversion, although it may also possible to reach a triplet state by intersystem crossing. Back in the ground state, the chromophore is now vibrationally hot. If the internal energy is sufficiently high to break one or more of the bonds, the chromophore can break apart. This process may require the energy of

more than one photon. For negatively charged ions the process of fragmentation is the same, however, the energy required to emit an electron is lower. Thus, fragmentation may be competing with electron emission. The process of electron emission can occur directly upon photon absorption, however, it may also occur following resonant excitation in the anion. The electron can be emitted from the excited state, or following internal conversion, from the vibrationally hot ground state.

Action spectroscopy has become a popular method of performing experiments on dilute molecular gases. Unfortunately, this approach also has its shortcomings. For one it may be troublesome to transfer the chromophores into the gas phase, moreover getting proper statistics can be difficult and, moreover, there is no guarantee that an absorption event results in any 'action'.

Action spectroscopy experiments can be performed using different experimental techniques, such as mass spectrometry [22–24]. The action is induced with different probing techniques and time-scales: with infrared multiple-photon dissociation spectroscopy [25], IR-UV double resonance spectroscopy [26], resonance enhanced multi-photon ionization (REMPI) [27, 28], fluorescence spectroscopy [23, 28], femtosecond spectroscopy [29] and photoelectron spectroscopy [29–31]. The different methods have their strengths and weaknesses and often probe different properties of the gas phase molecules. For the same reason care has to be taken when comparing results obtained with different techniques.

The experimental results presented in this work were obtained by action spectroscopy methods. The experiments have been performed at two experimental setups in Aarhus in which it is possible to study charged atoms and molecules.

In the first, an electrostatic storage ring, the gas phase ions are probed with laser light in the UV and visible range and the measurable action is photo-dissociation, specifically detection of neutral fragments. It is possible to monitor fragmentation for up to seconds, however, the experiment is primarily used to detect dissociation on the μs -ms time-scale. The use of a glass plate detector has allowed for measuring both prompt action and delayed action (statistical fragmentation). This has significantly improved the insights gained from the experiments.

In the second setup, the time-of-flight of neutral fragments can be measured together with the energy of emitted electrons. The experiment is sensitive to dissociation on the ns- μs time-scale. The setup has been changed slightly from its original design to achieve velocity map imaging condition.

Moreover, the setup has been adjusted to allow for detection of electrons emitted from the ions with low energy. This information is crucial in order to fully understand the properties of the chromophore ions.

This work presents experiments performed on models for the chromophores found in the green fluorescent protein and the photoactive yellow protein. The intrinsic photo-physical properties of the chromophores are examined by studying and comparing the photo-dissociation absorption spectra and photo-electron spectra of different isomeric forms of the chromophores. For PYP, three model chromophores: the *ortho*-, *meta*- and *para*-isomers are studied and for GFP it is *meta*- and *para*-isomers. These molecules may with a training as a physicist look very similar, however, as the work shows - what seems like a minor change may in fact alter the properties drastically. For the *meta*-isomer, the degree of the conjugation is affected by a change in the coupling between the phenol/phenolate and the rest of the chromophore.

CHAPTER 2

Experimental techniques

The main reason to do experiments on molecules in the gas-phase is the simple fact that it enables one to probe a molecule without interactions with a surrounding media. Moreover, experiments to monitor the effect from specific interactions can be performed, as is the case of e.g. micro-hydration and cluster experiments. Such gas-phase experiments provide important information on the intrinsic properties of the molecules, information that is harder to deduce from solution phase experiments.

Unfortunately, as is the case with most things in life, nothing comes for free. The gained knowledge from gas-phase experiments comes at the price of greater experimental effort.

The first challenge is transferring a desired charged or neutral molecule into the gas-phase. A wealth of different techniques have been developed throughout the years to overcome this hurdle, since there is no single technique to properly handle all molecules. In this work, the method of electro-spray ionization has been utilized to produce both positively and negatively charged gas-phase ions.

Second, a method for probing the gas-phase molecule is needed. Useful probes to obtain the desired information could be electrons, photons, electric/magnetic fields, another molecule or something completely different. As the purpose of the experiments in this work is to monitor the interactions between light and the gas-phase ions, a laser source has been used as a probe.

Thirdly, comes monitoring the outcome of the possible interaction between the molecule and the probe. The method of measuring a difference in transmission of light (Lambert-Beer (Ref)), does not apply to very di-

lute targets as gas-phase ions. The number of ions in the gas-phase is much lower than the number of photons, which means that the decrease in photon-number is too low to be measured. Hence, another method is needed. In this case the interaction is monitored by observing the possible action of neutralization of the gas-phase ion, either by dissociation or electron emission. This approach is termed action spectroscopy and was explained in the Introduction. In the following sections, the experimental setup and methods of this work will be explained in detail.

2.1 Ion production and trapping

Transferring the chromophore samples into the gas-phase has to be performed in a gentle manner in order not to chemically alter the sample. For the purpose of biomolecules, the electro-spray ionization (ESI) technique is a commonly used method. The invention of this technique [32] earned John Fenn the Nobel Prize in Chemistry in 2002. In this method, the relevant sample is first dissolved in a solvent. Depending on the sample, different solvents can be used, like acetonitrile, ethanol, mixtures of methanol and water. In the experiments presented here only methanol was used. Protonation or deprotonation of the sample can be improved by adding either an acid or a base, however, this was not done for the experiments that composes this thesis. By using a syringe positioned in a controllable syringe pump, the flow of the sample solution through a thin capillary to a metal tip can be controlled. This needle tip is positioned a short distance, roughly a centimetre, from another (heated) capillary, as depicted in Fig. 2.1. By applying a bias voltage of $\pm 2-4$ kV to the tip, the solution flowing out through the capillary forms a Taylor cone as a result of the electric field. The cone ends as a jet directed towards the heated capillary. On its way towards the heated capillary, the jet becomes small charged droplets, that undergo Coulomb explosions as the surface tension is too low to overcome the electrostatic repulsion between the ions [33]. The heated capillary is kept at a fixed temperature, optimizing the evaporation of the remaining solvent from the droplets. In the experiments mentioned in this work the capillary was heated to temperatures from 25-125 °C. This method of soft ionization allows for transferring the bio-chromophores to the gas phase.

From the heated capillary the ions pass through a skimmer and are guided through an octupole and focused by electrostatic lenses into a multi-

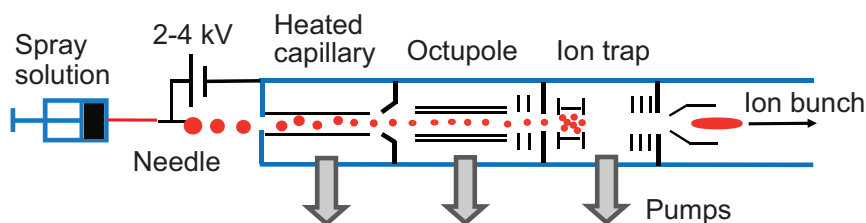


Figure 2.1: A schematic of the electro-spray ionization source used for the experiments.

pole ion trap (14-pole at ELISA, 22-pole at SEPII). The settings of the trap can be set to allow a continuous beam of ions to pass, however, in this manner the ion density from the ESI-source is too low to use for experiments. Moreover, it would not be possible to measure the lifetimes of the ions in direct beam mode. Thus, the trap is used to collect the ions continuously and create ion bunches. In the trap the ions are slowed down by collision with a helium buffer gas and trapped by an RF-field. The phase of the rapidly oscillating electric field (MHz-rate) is opposite for odd and even electrodes, effectively creating a trapping potential. The entrance and exit electrodes are during trapping kept at similar potentials, however, for extracting an ion bunch the voltage of the exit electrode is switched for 20–50 μs . If desired, the trap can be cooled by using liquid nitrogen, whereby temperatures down to $-120\text{ }^\circ\text{C}$ can be achieved. Depending on the sample and the settings of the ion source an ion bunch consists of up to $\sim 10^5$ ions.

2.2 ELISA

At the ELeCtrostatic Ion Storage ring in Aarhus (ELISA), shown in Fig. 2.2, the ions can be stored in a storage ring for up to several seconds, however, the usual storage time is 100 ms. Usual experiments at ELISA involve measuring the action absorption spectra of the gas-phase ions, measuring the decay time upon laser excitation and measuring the fragment masses after photo-excitation. Moreover, it is possible to compare the collisional lifetime of ions. This is done by recording and comparing the typical storage spectra of different ions. With a typical revolution time of $\sim 50\ \mu\text{s}$, dynamics of ions can be studied at the μs -ms time-scale. ELISA has been

described in detail [34–36].

The ion source is kept on a high voltage platform. The platform is kept at 22 kV in order to accelerate the ion bunches, when they leave this ion source. The pressure in this acceleration region is on the order of 10^{-7} mbar. The ions are hereafter focused by an Einzel lens and guided by electrostatic deflectors into a dipole magnet. This magnet serves as a mass filter, as the bending radius depends on the mass to charge ratio. Only ions with the right m/q -ratio are bend directly towards the opening of the storage ring. The relation between the required magnetic field, B , acceleration voltage, V , bending radius and m/q is

$$B = \sqrt{\frac{m}{q}} \sqrt{\frac{2V}{R^2}}. \quad (2.1)$$

The mass selected ion bunch are then directed by electrostatic deflectors and quadrupoles through a ~ 4 m long differential pumping region to the entrance of the storage ring.

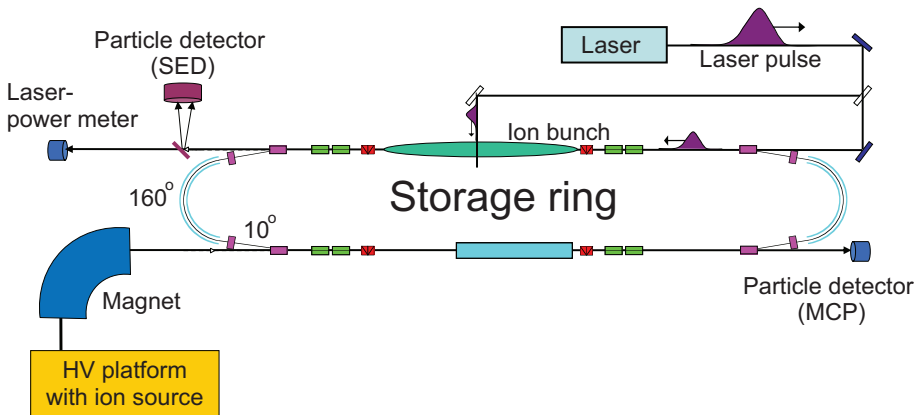


Figure 2.2: A schematic of the ELeCtrostatic Ion Storage ring in Aarhus, ELISA.

The storage ring, kept at a pressure of 10^{-11} mbar, is shaped like a race track as seen in Fig. 2.2 and has a circumference of 7,6 m [35]. In each end of the ring, two 10° and one 160° electrostatic deflectors bend the ions to circulate in the ring. When entering the ring the voltage of the first 10° deflector is momentarily switched off and on again to allow the ions to

pass unaffected through. Throughout the ring several sets of electrostatic deflectors (vertical and horizontal) and quadrupoles steer the ion bunch safely through the ring.

One great advantage of guiding and storing the ions by electric fields is that experimental settings of the ring are independent of mass. This is the case since the electric field, E , required to achieve a given bending radius is independent of mass

$$E = \frac{2V}{R}. \quad (2.2)$$

Furthermore, the electrostatic deflectors does not suffer from hysteresis as is the case for magnets. Another advantage is that the power used to keep the deflector-plates at a constant potential is lower than keeping a current running in a dipole-magnet to maintain a given magnetic field.

2.3 Detection systems

At ELISA a detector is positioned after the first straight section, see Fig 2.2. If an ion dissociates in this straight section any neutral fragment passes unaffected through the 10° deflector and hits the micro channel plate (MCP) detector. At the back of the MCP a phosphor plate, held at a higher potential (~ 2 kV), is positioned. The electrons are accelerated from the back of the MCP to the phosphor plate which light up when hit. A charge coupled device (CCD) camera monitors the phosphor plate, and the positions of the neutral fragments could in principle be recorded. The camera is, however, primarily used to monitor the neutral yield during beam optimization and measurements.

At the end of the second straight section another detector can be lowered into the path of the neutral fragments. This detector, shown schematically in Fig. 2.3 consists of a glass plate with a coating of tin doped indium oxide (ITO). The ITO layer emits secondary electrons when hit by an energetic particle (or photon). As the glass plate is biased by a negative voltage, the emitted electrons are accelerated towards and through the grid, kept at ground potential, and towards a channeltron. When the electrons hit the inside of the channeltron a cascade of electrons are emitted creating an avalanche effect, similarly to the MCP detectors. The advantage of using this detector is that it is transparent to light, at least in the visible region. Thus, the laser pulse passes unaffected through the glass and this detector

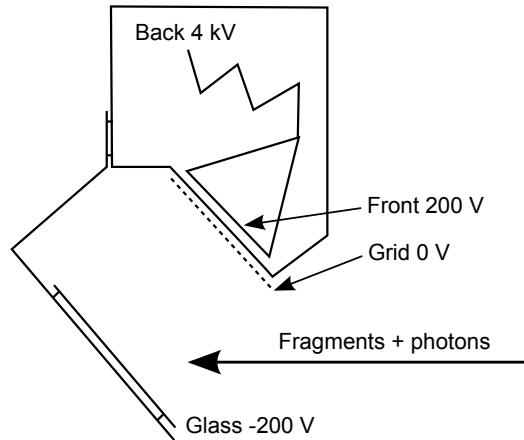


Figure 2.3: A schematic of the secondary electron detector, SED.

can be used in both longitudinal and crossed beam experiments. Unfortunately, the coating is destroyed by UV-light which rules out the use of this detector for longitudinal experiments at wavelengths lower than 355 nm.

In order to get estimates of the relative absorption cross sections at different wavelengths a measure of the number of photons is needed. This is found by measuring the laser pulse energy. At ELISA a power meter is usually positioned at the end of the second straight section, however, for cross beam experiments, it is position below the storage ring, where the light leaves the interaction position.

2.3.1 Laser systems

A source of light is needed to examine the interaction between the gas-phase ions and light. For the experiments for this project, both at ELISA and SEPII, the primary source for laser pulses has been the commercial EK-SPLA NT342/C/3/UV laser system. This laser system, a user-friendly table-top laser, delivers 3-5 ns laser pulses in the wavelength range of 210-2300 nm at a rate of up to 20 Hz. The laser pulses at 1064 nm created by the lasing unit, a Nd:YAG rod pumped by two flash-lamps, are converted to the third harmonic, 355 nm, in two non-linear crystals. The third harmonic is fed into an optical parametric oscillator (OPO), where two other non-linear crystals split the 355 nm photons into two, the signal and idler. Depending on the angles of these two crystals, the signal varies in wave-

length from 420-710 nm and the idler from 2300-710 nm. These photons can be coupled out to be used in the experiments. The signal and idler can, if UV-photons are needed, be guided through an additional set of non-linear crystals to be frequency doubled, enabling experiments in the 210-420 nm range. Due to all these non-linear processes, the pulse energy is somewhat lower in the UV range, down to 0.1 mJ, although, which is usually sufficient for experiments. In the visible range the pulse energy is well above 1 mJ. In most cases the pulse energy is best kept in the 0.2-0.3 mJ range to avoid saturation and consecutive photon absorption and still maintaining a reasonable yield of neutral fragments.

The second laser system, a Spectra-Physics Quanta-Ray Nd:YAG laser, essentially works in the same way as the other laser system, however, changing wavelength is more cumbersome, for which reason it is used for specific wavelength regions only.

2.4 Experimental procedures - ELISA

Although the gas-phase ions can be stored in the storage ring for several seconds, the rate with which experiments are performed is usually kept at a rate of 10 Hz. Thus, the ion trap is emptied every 100 ms and an ion bunch of $\sim 30 \mu\text{s}$ is let into the storage ring. For the first few milliseconds the yield of neutral fragments is a little higher than at later times as can be seen on the typical storage spectrum in Fig. 2.4. The higher yield of neutrals in the first milliseconds is due to fragmentation of hot ions. Some ions are vibrationally heated due to collisions with the residual gas at the acceleration stage. At later times the neutral yield stems from collisionally induced dissociation due to the residual gas in the storage ring. After storage for 100 ms the ions are dumped and a new ion bunch is loaded.

From a typical spectrum, as shown in the top graph of Fig. 2.4, a measure of the neutral fragment yield can be found. The counts in the green part before laser interaction, B , is used as a background measure of the number of ions in the bunch, while the counts in the red part, S , are the laser induced neutrals. The number of neutral counts in the signal window, S , would have been smaller without laser interaction, and this expected fraction is subtracted by finding a relation between the counts in the same time windows, S_0 and B_0 , without laser interaction. Hence, for each spectrum a measure of the yield at a given laser pulse energy and

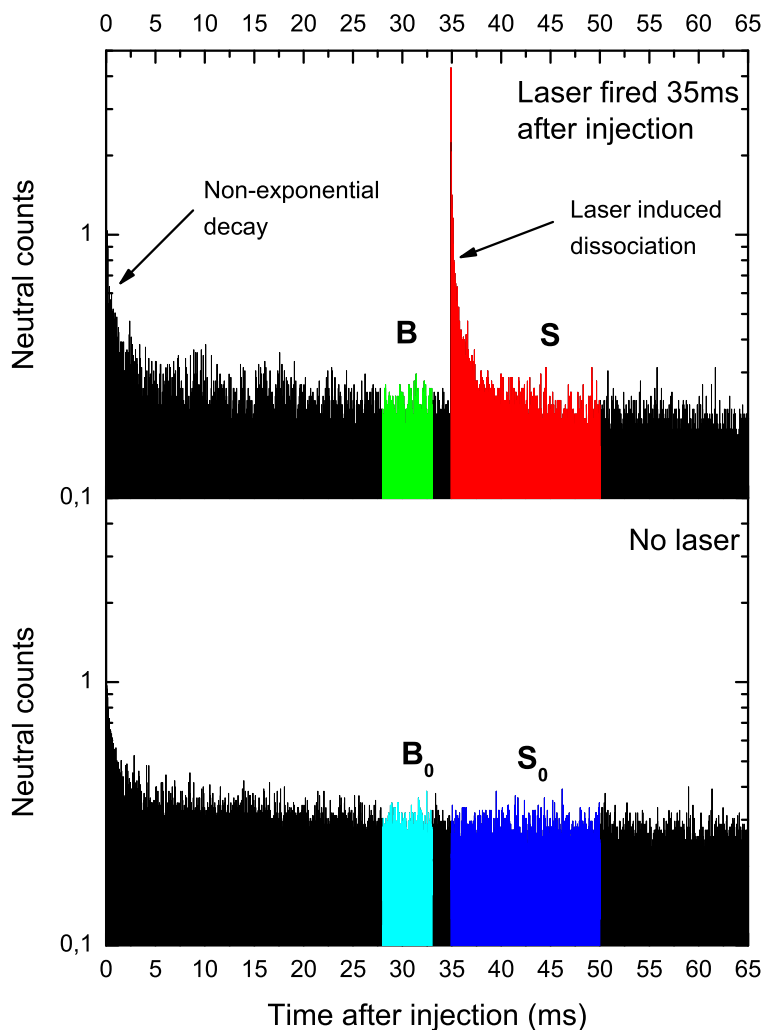


Figure 2.4: Two typical storage spectra at ELISA. The bottom graph shows the typical neutral yield on the MCP detector as a function of storage time without laser interaction. The top figure shows the neutral yield on the MCP detector with the laser fired after ~ 35 ms. An increase in neutral fragments is clearly observed for several ms after laser interaction. The higher number of neutral fragments in the first ms after injection, the non-exponential part, are due to ions produced with higher internal energy in the source and acceleration region.

wavelength is found by

$$N_{yield} = \frac{S - B \cdot \frac{S_0}{B_0}}{B} \quad (2.3)$$

By measuring the yield of neutral fragments at a fixed wavelength and varying the laser pulse energy, a measure of the power dependence of the fragmentation channel of the chromophores can be found. Moreover, by scanning the wavelength a measure of the absorption profile of the chromophore can be found.

2.4.1 Power dependence

A power dependence essentially determines how many photons are required to cause the ion to dissociate, being it by electron emission or fragmentation. The number of photons needed to cause dissociation vary from ion to ion due to the difference in barriers and energetics of the possible decay pathways for each ion. It may be that an ion only requires the energy of one photon at a given wavelength to dissociate, however, if this process occurs on the second-time-scale, it may be hard (if not impossible) to monitor at ELISA. The frequency (10 Hz) of the experiment is too high if the lifetime is very long, but although this can be changed, the main problem is that the time-scale of radiative cooling is usually shorter than 100 ms.

The power dependence is usually performed around the maximum of absorption for a given ion. If the ions have more than one absorption maximum, the dependence at the peak at highest wavelength is found first. For a power dependence the laser is kept at a fixed wavelength and the laser pulse energy is varied by inserting neutral density filters into the laser beam path, hereby attenuating the pulse energy. The average pulse energy is found by the power meter and the storage spectrum is measured. This is repeated for several combinations of filters until a reasonably number of experimental points have been found.

The absorption of photons is expected to follow Poisson statistics. That is, the yield of neutral fragments as a function of laser pulse energy can be fitted to

$$f(n, \nu) \propto \frac{\nu^n \cdot e^{-\nu}}{n!} \quad (2.4)$$

where ν is the average number of photons absorbed during the interaction time [37]. n is the index determining whether dissociation is 1, 2 or 3 pho-

tons. This approach does not take saturation of the ion bunch into account, however, it is not problematic, as long as the laser energy is kept low.

If the laser energy is not kept low it may be difficult to distinguish between a true 1-photon dependence and a 2-photon dependence affected by saturation. That is, a true 1-photon dependent process will look linear up until a point where saturation sets in. A 2-photon dependent process may look like linear in an energy-regime, where the combined effect of the requirement of the energy of 2 photons and a beginning saturation, effectively results in a linear response. To avoid misinterpretations, the power dependence has to be performed at laser pulse energies where saturation effects are minimal.

If the result of a power dependence shows a two-photon dependence at a high wavelength peak, it is necessary to perform one or more additional power dependences if other absorption peaks are found at lower wavelengths. This is needed as the dependence may change as the photon energy increases at lower wavelengths.

2.4.2 Absorption spectroscopy

To measure action absorption spectra at ELISA is not much different than performing a power dependence. The difference is that only one storage spectrum is measured for each wavelength, and that the wavelength is scanned instead of the average laser pulse energy. Just like for a power dependence, a spectrum without laser interaction is used to find a factor used for subtracting the collisionally induced fragments from the spectra with laser on. That is, in the signal time window with the laser on, some of the counts are due to collisions and not laser interaction. To subtract these a spectrum without laser interaction is recorded, from which the number of neutral fragments in the signal window relative to the number of fragments in the background window can be found. With this relation the number of neutral fragments expected to arise from collisions can be subtracted from a spectrum with the laser on.

The measurements of absorption spectra have been more or less automated. The wavelength of the EKSPLA laser system is shifted by the control program, and the relevant information is stored as the experiments are running. The analysis of the data depends on the number of photons that are required to induce dissociation of the ions.

The number of neutral fragments N_{neu} are found from

$$N_{neu} = S - B \cdot \frac{S_0}{B_0} \quad (2.5)$$

. The dependence between the number of neutral fragments and the cross section $\sigma(\lambda)$ is

$$N_{neu}(\lambda) \propto \sigma(\lambda) \cdot N_{phot} \cdot N_{ion} \quad (2.6)$$

where N_{phot} is the number of photons, found from the laser pulse energy E_{las} and the wavelength λ , and N_{ion} is a measure of the number of ions in the ion bunch, B . By combining Eq. 2.3 and 2.6 an expression for the relative action absorption cross section for a one photon dependence is found

$$\sigma(\lambda) \propto \frac{N_{neu}(\lambda)}{N_{ion}} \frac{1}{E_{las} \cdot \lambda} \quad (2.7)$$

If dissociation requires the energy of two photons, the three terms on the right side of Eq. 2.6 are squared and the expression for the cross section changes into

$$\sigma(\lambda) \propto \frac{\sqrt{N_{neu}(\lambda)}}{N_{ion}} \frac{1}{E_{las} \cdot \lambda} \quad (2.8)$$

Although much of the data acquisition has been automated, not everything can be controlled from the control system. Obtaining a good overlap between ion bunch and the laser pulse requires some patience. Moreover, the mirrors that guides the laser light into the storage ring are changed when using UV-light. As this procedure inevitably changes the overlap between the laser light and the ion bunches, care has to be taken when matching spectra taken above and below 420 nm.

2.5 Photo-electron spectroscopy - SEPII

With the setup at separator II (SEPII), the dynamics of the gas-phase ions can be studied on time-scales of ns- μ s, 10^3 times shorter than possible at ELISA. Besides monitoring the neutral fragments, it is furthermore possible to measure detached electrons.

Similarly to the setup at ELISA, the extracted ion bunches at SEPII are accelerated by a potential of 20 kV, focused by a lens and mass selected

by a dipole magnet. Hereafter, the ions are guided through a differential pumping stage and deflected 3° by an electrostatic deflector as shown in Fig. 2.5. The purpose of this deflector is to avoid having too much background noise on the detector from collisionally induced fragments in the differential pumping stage. The ions are deflected towards the interaction region, while the neutral fragments continue straight forward.

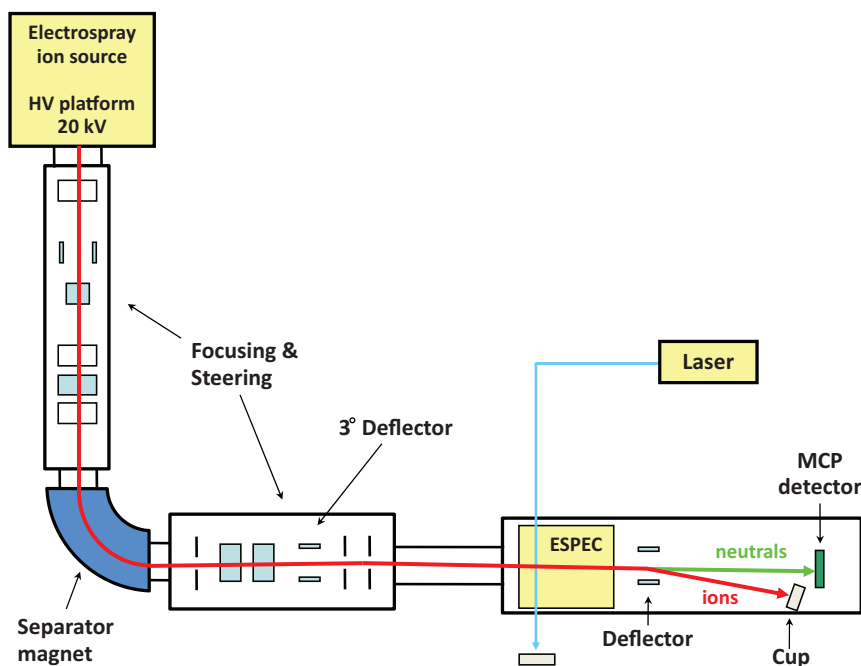


Figure 2.5: A schematic of the setup at Separator II (SEPII).

The interaction region consists of 25 equally spaced circular plates connected by resistors, initially used to form a constant potential slope throughout the spectrometer [38]. A laser pulse can be let through windows between plates 7 and 8 to interact with the ion beam, as depicted in Fig. 2.6. The potential difference between the entrance and the exit of the spectrometer serves two purposes:

Firstly, the potential serves to raise or lower (depending on the polarity of the potential) the kinetic energy of the ion bunch at the entrance to the spectrometer. The velocity of the ion bunch now reduces or increases

throughout the spectrometer. The ion bunch is deflected by an electrostatic deflector 0.45 m downstream. By measuring the time-of-flight (TOF) of the neutral fragments on the neutral detector (n-MCP), the dissociation time can be found. The information obtained in this way has not been used in this work.

Secondly, the potential is used to accelerate emitted electrons towards the electron detector (e-MCP) at the end of the spectrometer. This detector has a hole in the middle to allow passage of the ion bunch and neutral fragments. In order to measure electrons emitted with a low kinetic energy and to improve the resolution, the voltages of the spectrometer have been altered to consist of two constant potential slopes and a magnetic field has been applied [39]. Plates 1-10 have a decreasing potential slope, however, the potential slope from plate 11 to 25 is steeper, see Fig. 2.6. With the right ratio between these voltages, electrostatic focusing onto the plane of the e-MCP detector is achieved, hereby fulfilling the criteria for velocity-map-imaging (VMI). The applied magnetic field in the y-direction acts as a drift force on the emitted electrons and shifts the position in the x-direction. Thus, the centre of the electron distribution is shifted away from the hole and onto the detector.

The shift in x-direction is found by the Lorentz force $\vec{F} = q(\vec{E} + \vec{v} \times \vec{B})$, which can also be written as $\vec{F} = m\vec{a} = m(\ddot{x}\hat{x} + \ddot{y}\hat{y} + \ddot{z}\hat{z})$. This gives the following equations to be solved

$$m\ddot{x} = -qB\dot{z} \quad (2.9)$$

$$m\ddot{y} = 0 \quad (2.10)$$

$$m\ddot{z} = -qE - qB\dot{x} \quad (2.11)$$

Due to its smaller size, the contribution in the z-direction from the magnetic field is omitted. By integrating Eq. 2.11 twice the relation between time of flight and the z-position is found to be

$$z = -\frac{qE}{2m}t^2 + \dot{z}_0t + z_0 \quad (2.12)$$

By combining the above equations an expression of the x- and y-position is found

$$x = \frac{q^2BE}{6m^2}t^3 - \frac{qB}{2}\dot{z}_0t^2 + \dot{x}_0t + x_0 \quad (2.13)$$

$$y = \dot{y}_0t + y_0 \quad (2.14)$$

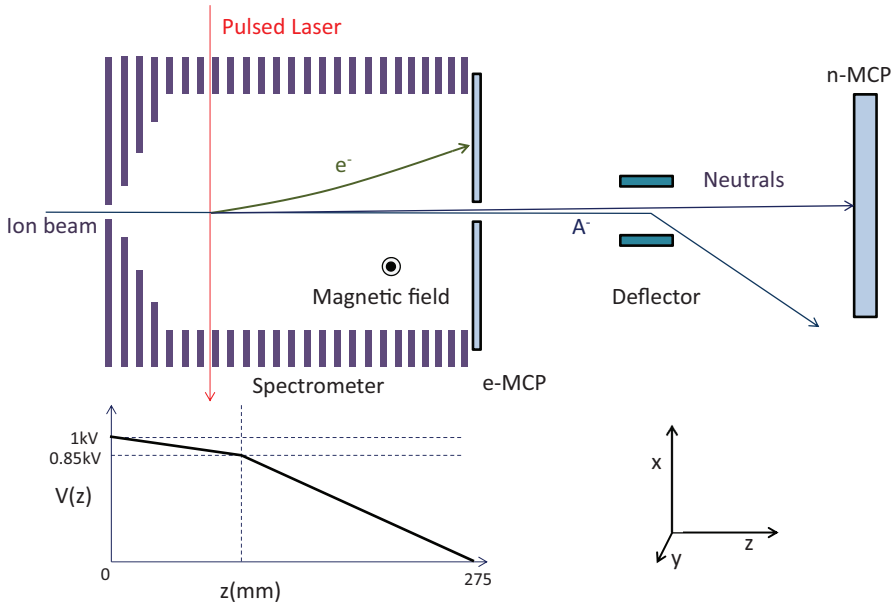


Figure 2.6: A view of the interaction region.

Since the magnetic field is in the y -direction, there is no effect on the y -position from this. By assuming that only the t^3 -term in Eq. 2.13 and the t^2 -term in Eq. 2.12 have the highest influence the final x -position is

$$x = \sqrt{\frac{2qL^3}{9m}} \frac{B}{\sqrt{E}} t^3 \quad (2.15)$$

All of the above assumes a constant electric field in the z -direction and shows that the x -position is linear with the applied magnetic field but scales inversely to the square root of the electric field. This relation has been checked by numerical simulation using SIMION [40]. Furthermore, it was verified that the focusing effect was also valid with the applied magnetic field.

2.5.1 Detection systems and laser systems

The detection of neutral fragments and electrons at SEPII are done similarly to at ELISA. The two detectors, n-MCP and e-MCP, function like the MCP at ELISA, however the main difference is that the position of the hits on the detector are recorded for these two detectors. This position information is needed for the data analysis.

The laser system used at SEPII is also the EKSPLA laser system, and similarly the laser pulse energy is recorded for each laser pulse.

2.5.2 Experimental procedures

For the photo-electron spectroscopy experiments performed at SEPII, the limit for the frequency with which the experiments can be performed is limited by the rate at which the laser can be fired. As the EKSPLA laser system was used for the experiments, this rate is 20 Hz. With the laser running at 20 Hz, the trap in the ESI source is emptied at a rate of 10 Hz. By having ions every second laser shot, every other measurement can be used as a measure for the background count of electrons and neutrals. These electrons come from laser light interaction with the residual gas in the spectrometer and the surfaces of the spectrometer, e.g. the plates and the windows. This background measurement is important especially at lower wavelengths where background electrons are hard to avoid. Since the wavelength of the laser can be changed, experiments were conducted at several wavelengths.

For each measurement, the time of arrival of any neutral fragments and any electrons are recorded together with the positions from the CCD-camera. In addition, the time of the laser pulse is measured by the signal from a photo-diode monitoring the scattered laser light on the power meter. By combining these timing data and the position on the CCD-cameras, electron kinetic energy distributions can be constructed.

Firstly, only injections where one electron is measured are chosen for further analysis. The reason for this is that it is not possible to determine which timing signal belong to which position if several electrons are observed. A typical distribution of electrons on the e-MCP detector is shown in Fig. 2.7. Next, the centre of the distribution of one-hit electrons on the e-MCP is chosen and a distribution of electron yield as a function of radius from this centre is found. Such a typical r-distribution can be found in Fig. 2.7. As the figure shows, the number of electron hits initially increases

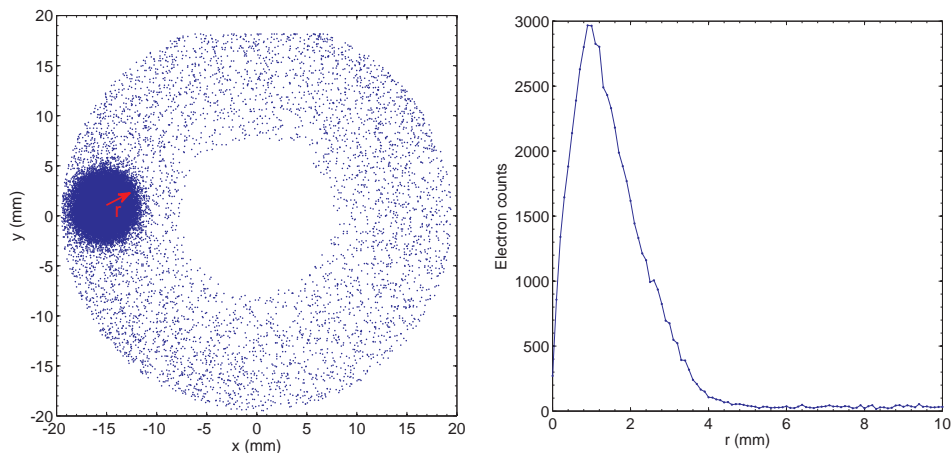


Figure 2.7: The figure to the left shows the individual electron hits on the MCP-detector. The full blue circle is the region where the electrons emitted from the anions. To the right the number of electron hits on the detector as a function of radius, with the radius measured from the centre of the intense blue circle.

with r , but then falls off at higher radii. The reason that the r -distribution goes to 0 in $r = 0$, is that the area $dA = \pi((r + dr)^2 - r^2)$ is small for small r .

In order to get the energy distribution of the electrons from a given distribution of r 's, the data points are first smoothened once, whereafter a Monte Carlo (MC) algorithm is used to fit an electron energy distribution to the r -distribution. An example of a MC-fit is seen in Fig. 2.8 together with the corresponding electron distribution in Fig. 2.8. In this manner, the kinetic energy release (KER) of the electrons can be reconstructed from the initial positions on the camera.

In order to find the transformation factor from the radial distribution into the energy distribution, the setup has been calibrated with O^- . O^- was chosen since its electron detachment properties are well known and since this ion is produced in abundance with a cold cathode plasma ion source [41]. The radial distribution was found at 550 nm and 600 nm and fitted to the theoretical distribution. In this manner the proper conversion factors were found.

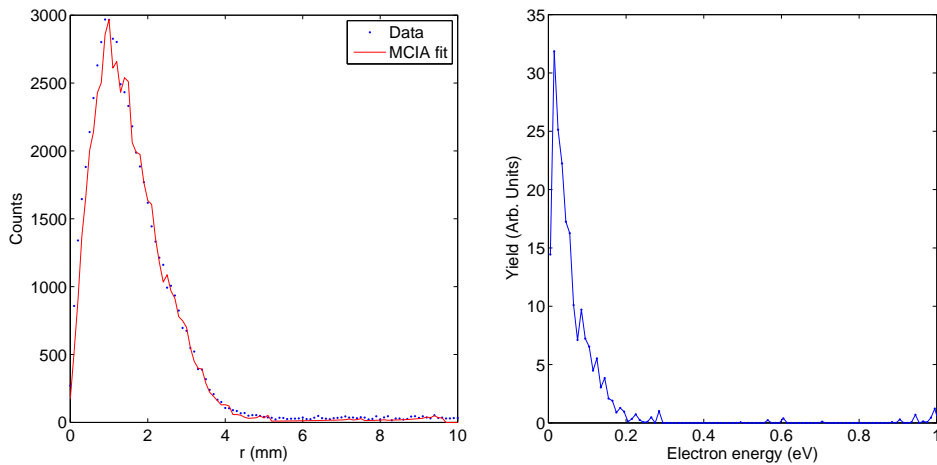


Figure 2.8: To the left the Monte Carlo fit is shown together with the corresponding r -distribution. To the right resulting electron kinetic energy distribution obtained from the Monte Carlo algorithm.

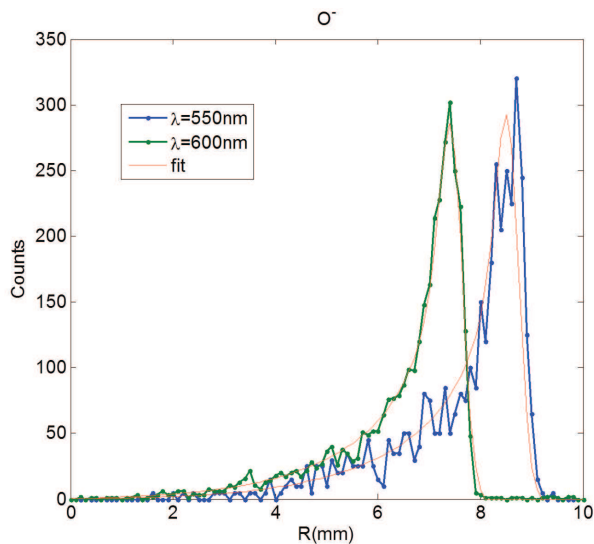


Figure 2.9: The experimental r -distributions of the O^- ions shown together with the theoretical fit to the data from which the conversion from radial distribution to energy was found.

CHAPTER 3

Computational methods

Though it is possible to conclude and learn much about the studied species from experimental results alone, it can often take the basic understanding and the conclusions to a higher level if it is supported by theoretical considerations. For some of the experiments presented in this thesis, the results are discussed on the basis of *ab initio*-calculations. The calculations have been performed with the Gaussian 03 and 09 packages [42, 43]. Besides the calculations performed with Gaussian, results obtained with more involved theoretical methods will be mentioned in this work, however, these results are the work of Anastasia Bochenkova.

Essentially, Quantum Chemistry deals with solving the Schrödinger equation

$$\left[-\frac{1}{2}\nabla^2 + V \right] \Psi(\mathbf{R}, \mathbf{r}) = \mathcal{E}\Psi(\mathbf{R}, \mathbf{r}), \quad (3.1)$$

where the two terms in the parentheses on the left is the operator for the kinetic energy and the potential, respectively, Ψ is the wavefunction and \mathcal{E} the energy. Unfortunately, it is not possible to solve this analytically for even the simplest molecule, H_2^+ . Thus, a number of approximations have to be applied to render calculations on molecular systems possible. One such approximation is the Born-Oppenheimer approximation, that takes advantage of the fact that the electrons are much lighter than the nuclei, for which reason they move much faster. This is implemented by splitting the wavefunction into two parts, one for the nuclei, and one for the electrons moving in the electric field of the 'fixed' nuclei.

In terms of approaches for calculating the properties of the systems the probably best known method is the Hartree-Fock (HF) approach. Within

the HF-approximation, the electron-electron interaction is initially neglected to simplify the problem, that now is about of solving one-electron Hamiltonians. The electron-electron interaction is then taken into account by considering the electric field from all electrons as one central field. Since the development of the HF-method other methods have been developed.

3.1 Density functional theory

A very popular method, due to its reasonably low computational costs and relatively good accuracy for many problems, is the density functional theory (DFT) method. DFT makes use of the electron probability density instead of the electron positions, which reduces the computational costs. The reason for the relatively low computational costs is that the number of coordinates boils down to the three spatial coordinates for the electron cloud. Within DFT the ground state energy can be found from the electron density

$$\rho(\mathbf{r}) = \sum_{i=1}^n |\Psi_i(\mathbf{r})|^2. \quad (3.2)$$

The Hohenberg-Kohn theorems state that the total energy for electrons moving in an external potential is a unique functional of the electron density ρ , and that the ground state energy can be obtained by the variational principle [44]. The ground state energy is found from the electron kinetic energy, the Coulomb interactions between the separate electron clouds, V_C , the electron clouds and the nuclei, V_N and finally a term called the exchange-correlation (V_{XC}) term [45]. These last three terms are called the effective potential (essentially V in the Schrödinger equation), V_{eff} ,

$$V_{eff} = V_C + V_N + V_{XC}. \quad (3.3)$$

The V_{XC} -functional accounts for the Pauli exclusion principle (spin) and the Coulomb correlation takes the repulsion of the electrons (although they have different spin) into account. It is called a functional since it uses the gradient of the exchange correlation energy E_{XC} as input and returns a scalar,

$$V_{XC} = \frac{\partial E_{XC}(\rho(\mathbf{r}))}{\partial \rho(\mathbf{r})}. \quad (3.4)$$

Since the electrons are regarded as non-interacting the Schrödinger equation, Eq. 3.1 simplifies to a set of one electron equations, the Kohn-Sham

equations

$$\left[-\frac{1}{2}\nabla^2 + V_{eff} \right] \psi_i(\mathbf{r}) = \epsilon_i \psi_i(\mathbf{r}), \quad (3.5)$$

Solving the equations deals with finding the electron distribution that results in the lowest energy of the system. This is done in an iterative process, since the effective potential depends on the electron density and hence the electron wavefunctions, which are part of the solution. Thus, the solution is found by the self-consistent field (SCF) method. In this method, an initial guess, based on standard orbitals, on the electron density is used to construct the effective potential. The obtained Kohn-Sham equation is then solved and new electron densities are calculated. These are compared to the previously used densities. This process is repeated until the densities are identical, within a given precision.

In the calculations for this work, the DFT method has been used with the widely used B3LYP functional [46, 47]. The B3LYP functional is a hybrid functional consisting of parts of other functionals. It makes use of Hartree-Fock theory, the correlation functional LYP and the Becke 88 exchange functional [46, 48]. Like all DFT-functionals, B3LYP functional has its drawbacks; dispersion forces as van-der-Waals forces are not accounted for. However, for many purposes this functional gives reasonably precise results. The accuracy of the method typically increases with larger basis-sets. For this work the 6-31+G(d,p) and the 6-311++G(d,p) basis-sets have been applied in the calculations. These basis-sets sizes have been chosen to keep the computational costs at a reasonable level while still maintaining good accuracy.

3.2 Time dependent density functional theory

The excitation energies for transitions to higher-lying states can also be calculated by density functional theory, however not in the time-independent form presented above. Instead, the time dependent Schrödinger equation

$$\hat{H}\psi_i(t) = i\frac{\partial\psi_i(t)}{\partial t} \quad (3.6)$$

has to be solved. With the Hamiltonian being time-dependent, due to a time-dependent field (electric or magnetic) the electron density is now both dependent on the spatial coordinates and time. The theory behind solving

this problem is build on the Runge-Gross theorems, which essentially corresponds to the Hohenberg-Kohn theorems for the time-independent DFT. These theorems state that the exact time-dependent electron density can be found by an action functional. This action functional does not have a minimum, as was the case within DFT, but instead a stationary point. By solving the time-dependent version of the Kohn-Sham equation, Eq. 3.7, with a now time-dependent effective potential $V_{eff,s}(\rho(\mathbf{r}, t))$ and once again by an iterative process, a measure for e. g. the excitation energy can be found [49, 50].

$$\left[-\frac{1}{2}\nabla^2 + V_{eff,s}(\rho(\mathbf{r}, t)) \right] \psi_i(t) = i\frac{\partial}{\partial t}\psi_i(t). \quad (3.7)$$

For the purpose of this work, these excitation energies are only used for following the general trend in excitation energies, not to determine the specific energies. Similarly, to determining ground state structures and energies with DFT, TD-DFT also has its weaknesses. Care has to be taken with transitions that are of charge-transfer character with the TD-DFT method.

3.3 The GAUSSIAN package

The theoretical calculations have been performed by the GAUSSIAN 03 and 09 packages [42, 43]. GAUSSIAN is a commercial program package by which it is possible to perform a variety of electronic structure computations. The package makes use of Gaussian-type atomic functions for the atomic orbitals, rendering faster computations possible. The orbitals are of the form:

$$g(\alpha, \mathbf{r}) = c \cdot x^n \cdot y^m \cdot z^l \cdot e^{-\alpha r^2} \quad (3.8)$$

where x, y and z makes up \mathbf{r} . n, m and l are integers, while α determines the radial extent of the orbital and c is used for normalization [51]. A p_y -type orbital would for instance be:

$$p_y(\alpha, \mathbf{r}) = \left(\frac{128\alpha^5}{\pi^3} \right)^{(1/4)} y e^{-\alpha r^2}. \quad (3.9)$$

With the GAUSSIAN program package it is possible to perform calculations with a large variety of methods: molecular mechanics, semi-empirical calculations, Hartree-Fock, DFT, coupled cluster and many other approaches. With these methods properties like: geometries, vibrational frequencies, state energies, potential energy surfaces and excitation energies can be found.

The photoactive yellow protein

4.1 Introduction

A photoactive protein that has shown to be of great significance in protein research throughout the last decades is the photoactive yellow protein (PYP). The protein was discovered in 1985 by T. E. Meyer [52] in a study of 'soluble cytochromes, ferredoxins and chromophoric proteins from the halophilic phototropic bacterium *Ectothiorhodospira halophila*'. This bacterium, now called *Halorhodospira halophila*, thrives in highly saline environments and shows interesting behaviour when subjected to light. The bacteria gather in areas with green and infra-red light, but more interestingly, they retract from areas with blue light, that is they show negative phototaxis to blue light. It has been shown by Sprenger *et al.* [53] that this negative phototaxis towards blue light is initiated by the small protein called the photoactive yellow protein.

PYP is a water soluble protein that consists of 125 amino acids. This fairly small size makes it a useful model system for studying the interaction between light and chromophore. It is one of the reasons, that PYP has been and is being studied extensively both theoretically and experimentally. The structure of the protein was first found by X-ray crystallography in 1998 [55], since then the resolution has been improved and the experiments repeated. The structure can be seen in Fig. 4.1.

The chromophore found within the photoactive yellow protein is *trans* 4-hydroxycinnamyl linked to the protein by a thiol bond [58] as shown in both Figs. 4.1 and 4.2. The small chromophore is deprotonated on the phenol and is connected to the protein by the thiol bond (the C–S-bond) to

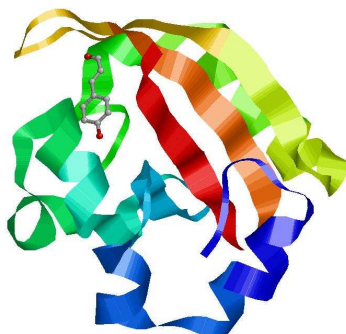


Figure 4.1: The structure of the photoactive yellow protein. The chromophore is shown by ball and sticks within the protein. Figure created with Rasmol from PDB ID: 2QJ5 [54].

Cys69. Moreover, the negative charge of the chromophore is stabilized by two hydrogen bonds from the hydroxy-oxygen to Glu46 and Tyr42 as is shown schematically in Fig. 4.2.

When situated within the protein, the chromophore absorbs maximally at 446 nm. The absorption of a photon initiates a reversible photo-cycle, shown in 4.3, during which a signal is sent to the bacterium to begin moving away [59, 60]. Depending on protein temperature, there are different relaxation pathways for the excited chromophore, however they end at the same intermediate state, I_1 [11]. This process of getting to I_1 happens on a time-scale of 3 ns and during this the chromophore undergoes a *trans-cis*-isomerization and the absorption is shifted to 465 nm [61]. The next step is a proton-transfer from Glu46 to the chromophore [62], which leaves it neutralized. This state, I_2 , is long lived - 500 ms, absorbs at 355 nm and is the state responsible for signalling [63]. In this state the protein is to a large extent unfolded and the chromophore is exposed to the solvent [64, 65]. From this state the protein can initiate the process that leads to the observed movement away from blue light [57]. In the last step, the chromophore is deprotonated, and isomerizes back to the *trans*-state and the protein refolds to its initial structure[66] on a time-scale of less than a second.

The photo-physical properties of the chromophore within PYP has been studied by various methods. The influence on the chromophore by the surrounding amino acids has been tested in mutational studies. By substitution of the amino acids participating in the hydrogen bonding, T50 and Y42, the absorption of the chromophore is red shifted by up to 30 nm

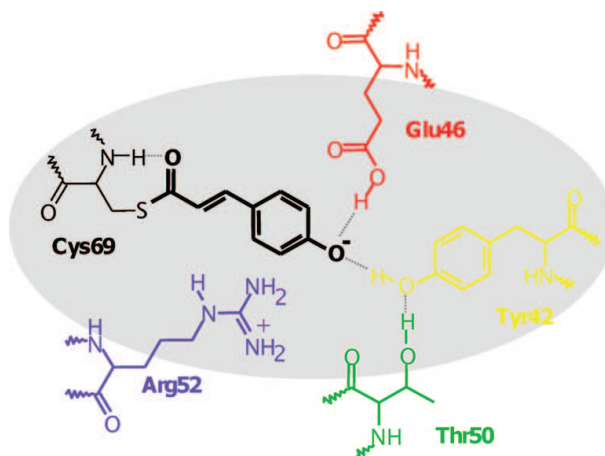


Figure 4.2: pCA^- and surrounding amino acids within the protein pocket. Reprinted from [56]

[4, 5, 7], due to an increase in the electron density on the aromatic ring. Models for the PYP chromophore have also been studied in solution phase [9, 13]. In these studies the dynamics of the chromophore upon excitation has been studied. The studies suggest that the chromophore not only isomerizes from *trans* to *cis* in the protein but also when in solution.

The isomerization process of the chromophore anion has been proposed to occur in the gas-phase [29], suggesting that this is an intrinsic property of the chromophore and not protein-induced. Thus the protein-pocket appears to work as a vacuum for the chromophore. This study also found the threshold for electron detachment to be 2.9 eV. Another gas-phase study has included a neutral version of the chromophore [27]. Absorption spectra for anionic models have shown the absorption maximum to be 460 nm for *trans*-thiophenyl-*p*-coumarate, pCT^- , while a model with sulphur replaced by oxygen, *trans-p*-coumaric acid, pCA^- , it was shifted to 430 nm. As a comparison pCT^- has its absorption maximum at 395 nm in aqueous solution [9]. Hence, it seems, that the protein is a gentler environment than a polar solvent.

The experiments performed on full proteins or on chromophores either in solution or gas-phase are both backed and countered by theoretical approaches. However, due to the size of the protein the focus of theoretical studies is primarily on the chromophore. Several studies have been conducted to understand the excitation properties of the chromophore with

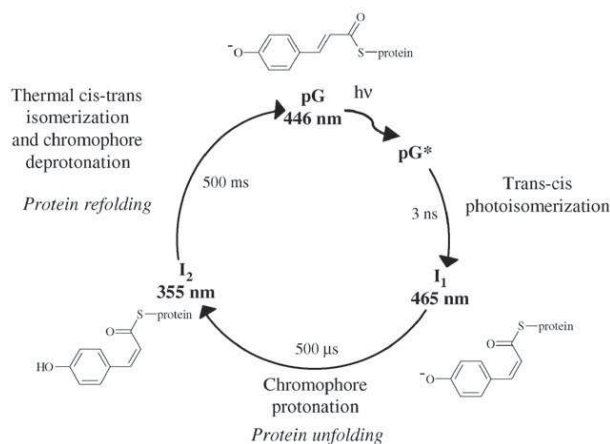


Figure 4.3: A schematic of the processes upon photo-excitation in the photoactive yellow protein [57]. Reproduced by permission of The Royal Society of Chemistry.

and without the immediate protein surroundings [15, 18, 19, 21, 67, 68]. Most theoretical methods agree on a detachment threshold of ~ 2.9 eV for the anionic chromophore, a threshold that is raised by the interaction with Arg52 in the protein. On the excitation energy for the anionic chromophore the methods on the other hand does not agree. Some works, predict this energy to lie above the detachment threshold [18, 21], while one finds the vertical excitation energy to be either above or below, depending on the theoretical method [69]. The relative positions of these levels is, however, important for understanding the complete picture of the photo-physical properties of the chromophore.

In this study, the approach is to study different models for the PYP chromophore in order to gain new insight into the photo-physical properties of both chromophore and protein. This is achieved by performing action absorption spectroscopy and photo-electron spectroscopy on anionic models in the gas-phase.

4.2 Absorption experiments

4.2.1 Experimental details

In order to investigate the photo-physical properties of the chromophore of the photoactive yellow protein a study on three models, three different

methyl-coumarate isomers, for the chromophore has been conducted at ELISA. The three models, shown in Fig. 4.4, have been synthesized by Prof. M. B. Nielsen and co-workers at the University of Copenhagen. By studying these three models, *ortho*-, *meta*- and *para*-CMe, the effect of the position of the phenolate can be studied. In the protein, the chromophore is found as a *para*-variant, however, the knowledge gained by studying various isomeric forms, may help increasing the understanding of the importance of the interplay between the phenol ring and the ester group (COOCH_3). In the *para*-version the degree of electronic delocalization is large, and the communication between the phenolate and ester group is effective. This can also be shown by the fact that it is possible to draw two resonance forms covering the whole of the chromophore for $p\text{CMe}^-$. For $o\text{CMe}^-$ it is similarly possible to draw two, while this is not possible for $m\text{CMe}^-$. This can be thought of as $m\text{CMe}^-$ being described by one ‘wavefunction’, while the other two isomers both are a linear combination of two ‘wavefunctions’. For this reason, it is expected that the *meta*-isomer will show a quite different photo-physical behaviour.

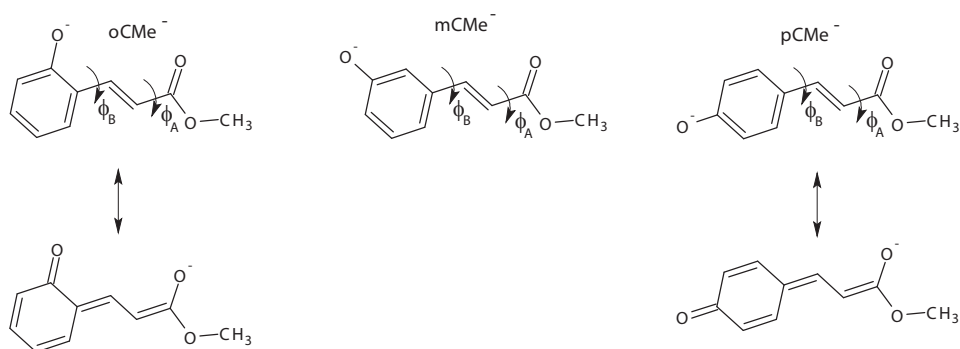


Figure 4.4: The three PYP model chromophores, $o\text{CMe}^-$, $m\text{CMe}^-$ and $p\text{CMe}^-$. Rotation about the two dihedral angles, ϕ_A and ϕ_B , change the extent of the conjugated system.

The experiment was performed at ELISA with a crossed beam setup. The laser beam crossed the ion bunch in the central part of the second straight section of the storage ring, see Fig. 2.2. The reason for not doing this with parallel beams was that the absorption of the *meta*-isomer was expected to be in the UV-region. This combined with the fast photo-response, dissociation within μs , requires the use of the prompt detector, the SED, in order to observe any photo-fragments. Unfortunately, by crossing the

beams in this manner, only a very small part of the ion bunch is subject to laser irradiation, increasing the time spent getting reasonable statistics.

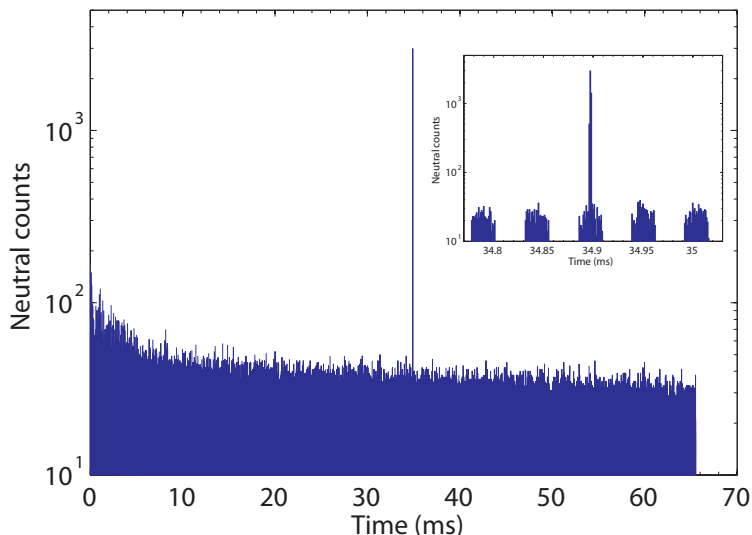


Figure 4.5: An experimental lifetime spectrum of $pCMe^-$ at 430 nm in ELISA. The inset shows the laser-induced fragments more clearly.

A typical experimental lifetime spectrum of the ions in ELISA is shown in Fig. 4.5. In this figure the increase in neutral counts are clearly seen, however, it is even clearer in the insert, where it is also observed that only a small part of the ion bunch is affected by the laser light. That is, only the tiny part of the ion bunch can be excited by the photons. From this figure it is also evident that the lifetime is too short for the excited ions to survive for the time of a revolution.

4.2.2 Results

The action absorption spectra, measured at ELISA for the other three model chromophores, $oCMe^-$, $mCMe^-$ and $pCMe^-$, shown in Figure 4.6. The first striking difference is in the position and strength of the visible absorption band labeled 1 in the figure. Especially the *meta*-isomer differs from the other two, as was expected from the lower electron delocalization. The relative cross section for the three model chromophores can be roughly compared to each other, as the experiments were conducted with the same settings and laser overlap. This was possible as the models have the same

mass.

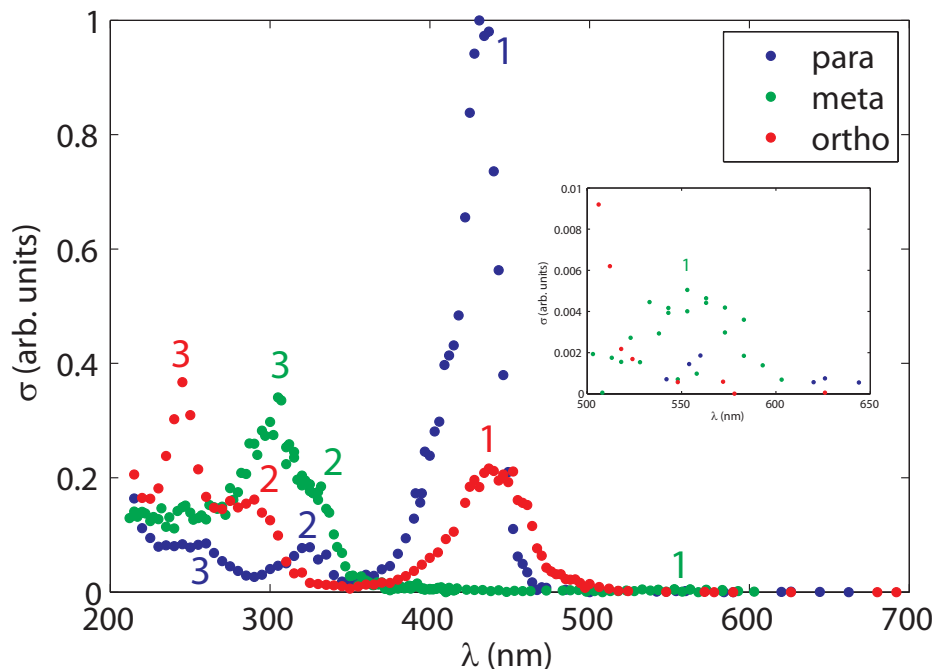


Figure 4.6: The ELISA action absorption spectra of $oCMe^-$, $mCMe^-$ and $pCMe^-$. The three data sets are scaled to each other, so the relative cross sections can be compared.

The absorption maxima are listed in Table 4.1. The maxima for $oCMe^-$ is estimated to be 439 nm, 290 nm and 245 nm. $pCMe^-$ has a peak at 432 nm and two less intense peaks at 323 nm and 260 nm. $mCMe^-$, on the other hand, shows no absorption in the 430-440 nm region but very weak absorption around 550 nm, as can be seen in the inset.

4.2.3 Discussion

As the HOMO and LUMO, found in Fig. 4.7, of the three chromophore models show, the electron density is shifted from the phenolate part to the methyl propenoate upon excitation [68]. These sub-systems are shown separately in Fig. 4.8. The phenolate serves as a donor and the ester as an acceptor. This is expected to have quite a pronounced effect on the excitation energies, when the oxygen position is shifted from *para* to *meta*

	Peak 1	Peak 2	Peak 3
$oCMe^-$	439 nm	290 nm	245 nm
$mCMe^-$	~550 nm	330 nm	302 nm
$pCMe^-$	432 nm	323 nm	260 nm

Table 4.1: The experimentally found absorption maxima for the three PYP model chromophores.

and *ortho*. For both $oCMe^-$ and $pCMe^-$, two resonance forms covering the whole chromophore can be drawn, as shown in Fig. 4.4. That this is not possible for $mCMe^-$, suggests that the electronic delocalization is much lower. The effect from this decoupling on the absorption spectrum is quite dramatic as seen in Fig. 4.6. The experimental spectrum will be discussed in the next sections.

Why *meta*-absorption differs from *para* and *ortho*

The lower degree of electronic delocalization for the *meta*-isomer is a result of a lower degree of coupling between the two 'sub-systems' of $mCMe^-$. If the coupling between these two subsystems, the phenolate and the methyl propenoate, is not adequate for the electronic states to couple strongly, then the excitation energy of $mCMe^-$ is quite different compared to $oCMe^-$ and $pCMe^-$. This is shown schematically in Fig. 4.8. This figure shows the highest occupied molecular orbital (HOMO) and lowest unoccupied molecular orbital (LUMO) of the two sub-systems for the three model chromophores. The lowest energy transition of the uncoupled systems is a charge transfer (CT) transition, while the $\pi \rightarrow \pi^*$ (bright) transitions occur on each sub-system. In Fig. 4.9 the effect of increasing coupling between two energetically close systems can affect the CT-degree of the first transition in the collected system.

$mCMe^-$ is expected to have a charge transfer transition with a low oscillator strength. The oscillator strength is low due to a very low overlap between the electronic wavefunctions ψ_4^I and ψ_4^{II} as shown in Fig. 4.8. Instead, the $\pi \rightarrow \pi^*$ transitions located on each of the two sub-systems are expected to have a higher oscillator strength.

The $mCMe^-$ absorption at 550 nm is the charge transfer transition, where electron density is shifted from the phenolate towards the ester. The transition energy is as expected lower than the bright transition at 430-440 nm for

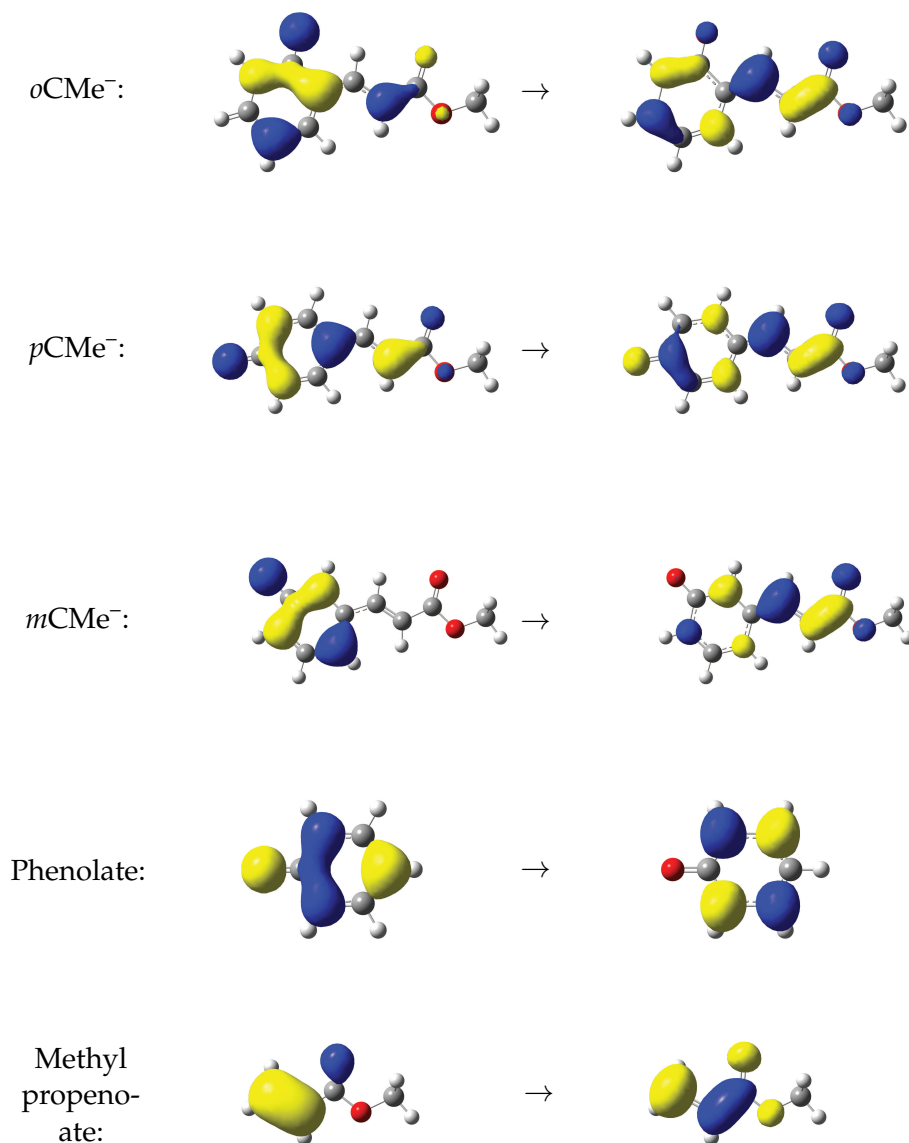


Figure 4.7: The HOMO- and LUMO-orbitals, left and right respectively, of $o\text{CMe}^-$, $p\text{CMe}^-$, $m\text{CMe}^-$, phenolate and methyl propenoate.

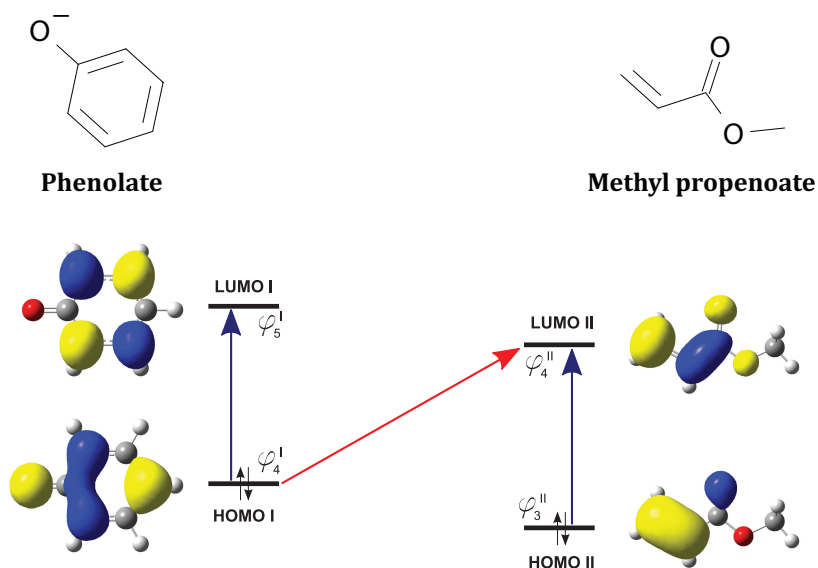


Figure 4.8: Topmost the two sub-systems are shown separately. Below a schematic showing the lowest energy transitions for two weakly coupled systems. The transition from system 1 to 2 (red arrow) is a charge transfer transition, while the two blue arrows indicate the transitions on the two separate π -systems. The orbitals found from the DFT-calculations are inserted next to the relevant orbital.

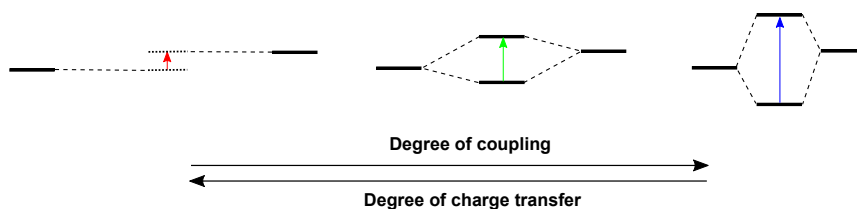


Figure 4.9: The figure shows the effect on the charge transfer character as an effect of increasing coupling from left to the right. The degree of charge transfer decreases as the coupling increases.

para and *ortho*, but at the cost of oscillator strength. Besides a lower oscillator strength, the photon energy at 550 nm could be too small to break apart the ion or to detach an electron. If two photons are required to cause dissociation, then the yield of neutrals would be expected to be lower. However, loss of CH₂O from *p*CMe⁻ has recently been found theoretically to cost 1.29 eV. Unfortunately, the laser power was not adequate at these wavelengths to perform a power dependence, see Section 2.4.1.

The main orbitals involved in the energetically lowest transitions for the 3 models found by DFT-calculation, show the charge transfer character of the transition, especially for *p*CMe⁻. These orbitals (HOMO and LUMO) are shown in Fig. 4.7. Except for the position of the phenyl oxygen, the orbitals for *p*CMe⁻ and *o*CMe⁻, are more or less identical. The orbitals for *m*CMe⁻, are on the other hand quite different on account of the lower degree of electron delocalization. The lower degree of coupling between the two sub-systems is clear by the electron cloud being localized on the phenolate only in the HOMO, while it is shifted to the methyl propenoate in the LUMO. Moreover, this is supported by the HOMO and LUMO orbitals of the phenolate and the methyl propenoate. These orbitals, found in Fig. 4.7, show that the HOMO of *m*CMe⁻ is identical to the HOMO of the phenolate sub-system. And the LUMO consists primarily of the LUMO of methyl propenoate. This supports the idea of thinking of this *meta* model as two very weakly connected sub-systems. From the HOMO and LUMO of *p*CMe⁻ and *o*CMe⁻, it is clear that the degree of electron delocalization is much larger, as is suggested by their valence resonance structures, see Section 4.2.1. This mixing of the orbitals of the separate systems results in a bright transition at a lower wavelength than the CT transition that was seen for *m*CMe⁻, however, with a higher oscillator strength.

A theoretical calculation for the transition energies of *m*CMe⁻ at the TD-DFT B3LYP/6-311+g(d,p) level of theory (see results in Tbl. 4.2) finds the lowest energy transition to lie at 683 nm with an oscillator strength of 0.02. The low oscillator strength matches nicely with the very weak absorption that was found around 550 nm. It is important to remember, that B3LYP functional has its problems with transitions of charge transfer character, for which reason it is not expected to precisely match the experimental value. The most intense absorption peak for *m*CMe⁻ appears at 302 nm, with a shoulder around 330 nm. From the simple picture in Fig. 4.8 these transitions would be the $\pi \rightarrow \pi^*$ transitions on each of the two sub-systems. In the theoretical approach, the orbitals mainly involved in the two bright transitions in the UV are found to partly agree with the idea of two separate

systems. The first transition, the shoulder, at 330 nm is calculated to 320 nm with an oscillator strength at 0.40. The orbitals involved in this transition (shown in Fig. 4.10), HOMO-1 (the second highest occupied molecular orbital) to LUMO, and show that the electron cloud is more delocalized in HOMO-1 than is the case for HOMO, which may explain the higher oscillator strength of this transition. The orbitals on the methyl propenoate part of the chromophore are close to identical to the HOMO-LUMO transition in the lone sub-system, although the phenolate part plays a role in the transition for the full chromophore.

	Peak 1	Peak 2	Peak 3
Exp.	~550 nm	330	302 nm
Theory	683 nm (0.02)	320 nm (0.40)	303 nm (0.19)

Table 4.2: The experimental and calculated absorption maxima (with corresponding oscillator strength) for the $m\text{CMe}^-$ PYP model chromophore.

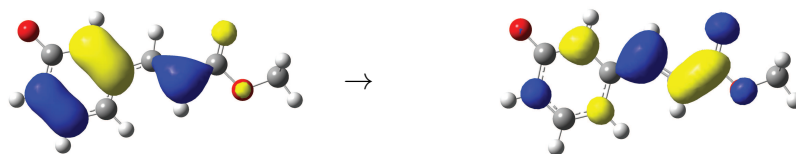


Figure 4.10: The orbitals involved in the transition at 320 nm in $m\text{CMe}^-$.

The theoretical estimate for the transition at 302 nm, is calculated to be 303 nm with an oscillator strength of 0.19. The orbitals involved in this transition can be seen in Fig. 4.11. It is evident from these orbitals that this transition occurs primarily on the phenolate part of the $m\text{CMe}^-$ chromophore, and they are practically identical to the HOMO and LUMO orbitals of the phenolate. Hence, this transition is located solely on this sub-system due to the low degree of coupling between the two. The calculated transition at the same level of theory for the phenolate is 318 nm, which is not far from the 303 nm found for the transition in $m\text{CMe}^-$.

In a study similar to the one presented above, the absorption properties for *ortho*-, *meta*- and *para*-isomers for the nitrophenolate anion were studied

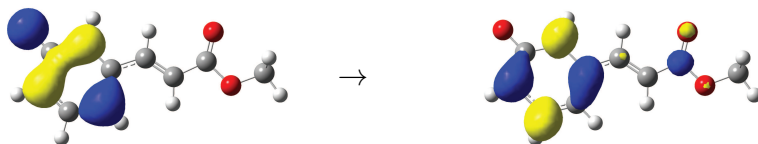


Figure 4.11: The orbitals involved in the two transition at 303 nm in $mCMe^-$.

[70]. The study found the *ortho*- and *para*-isomers to display similar absorption properties, while the absorption for the *meta*-isomer was found to be blueshifted. There was on the other hand no sign of a weaker redshifted transition, probably due to the low oscillator strength. The explanation for the blueshift of the bright transition is, as discussed above for the model chromophores for PYP, that the electronic coupling between the electron acceptor and donor parts is smaller than for the other two isomers.

Oscillator strengths

The two other models, $pCMe^-$ and $oCMe^-$, have the $S_0 \rightarrow S_1$ transitions (S_0 is the electronic ground state, while S_1 is the first excited state) very close to each other, 432 nm and 439 nm, respectively. However, the absorption cross section and the width of the absorption profile in the visible region are different. The relative absorption intensity of the three models can be compared, and it seems that the *para*-isomer has an absorption cross section roughly 5 times that of the *ortho*-isomer. This is not entirely true though, as the width of the $oCMe^-$ -peak is larger than for $pCMe^-$. By calculating the area under the absorption profile of the two peaks, a more realistic measure for the difference in cross section can be found. Such a comparison gives a 2.7 times higher cross section for $pCMe^-$. Hence the *para*-isomer appears to absorb stronger in the visible region. A TD-DFT B3LYP/6-311+g(d,p) calculation gave oscillator strengths of 0.91 and 0.35 for $pCMe^-$ and $oCMe^-$, respectively. This suggests that the *para*-isomer absorbs 2.6 times stronger, essentially the same as the experiment showed.

In the protein and hence in its natural surroundings, the chromophore is found as a *para*-isomer. Thus, in nature the chromophore is found in its

most light-sensitive form. This is of course only the case if the interaction with the surrounding protein does not change the absorption cross section of the *ortho*- and *meta*-isomers. If it is surprising or not, that the chromophore found in the protein in nature is the most light sensitive one, is probably a matter of belief. It is nonetheless convenient for the bacterium, for which the photoactive yellow protein serves as a warning system against photo-damage, that the proteins are as efficient as possible, as fewer proteins are then needed.

Rotamers

The absorption profiles for the $S_0 \rightarrow S_1$ transitions of $pCMe^-$ and $oCMe^-$ are not equally broad, as was noted above. The reason for this is most probably the possible presence of several rotamers in the ion bunches and shallow potentials for rotation about the two dihedral angles ϕ_A and ϕ_B shown in Fig. 4.4. By rotating about these bonds, four different rotamers/isomeric forms of $oCMe^-$ are possible, while only two forms are possible for $pCMe^-$ as a 180° rotation in ϕ_B does not result in a new isomer.

The barriers for rotation has been estimated by performing geometry optimizations at the DFT B3LYP/6-311+g(d,p) level of theory in steps of 15° for each of the dihedrals. Only one parameter has been changed at a time. For $oCMe^-$, this results in two potential energy curves, as seen in Fig. 4.12. This shows that the barrier for rotation is on the order ~ 0.5 eV for the ϕ_A dihedral, while it is somewhat higher ~ 0.7 eV for the ϕ_B dihedral. Similarly, the barrier for the ϕ_B dihedral of $pCMe^-$ is found to be ~ 0.8 eV and for $mCMe^-$ it is as low as ~ 0.4 eV as shown in Fig. 4.13.

These barrier heights have to be compared to the internal vibrational energy of the ions at 300 K. This is estimated on the basis on the calculated vibrational modes of the models by the following equation:

$$\langle E \rangle (T) = \sum_j \frac{h\nu_j}{\exp\left(\frac{h\nu_j}{k_B T}\right) - 1} \quad (4.1)$$

where ν_j is the vibrational modes and T the temperature. By this method the internal energy is estimated to be 0.26 eV at room temperature on average. This amount of internal energy is not enough to rotate freely around the two bonds in the gas-phase, however, it may be that this rotation can happen in the solution phase or in the spray process. Nonetheless, this amount of internal energy is enough for the $oCMe^-$ chromophore to rotate

up to 45° for both dihedrals if all the vibrational energy is located in this mode.

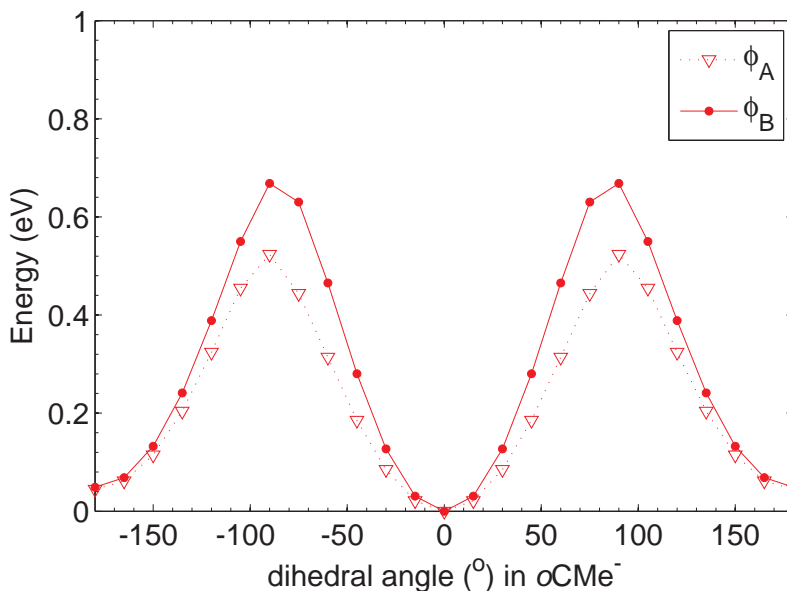


Figure 4.12: The ground state energy of $oCMe^-$ as function of dihedral angles ϕ_A and ϕ_B .

If the *para*- and *ortho* chromophores are not planar upon excitation, then the excitation energy is changed. The reason for this is that once the planarity is broken, then the electron delocalization across the chromophore is also lowered. The expected impact on the transition energy is a red-shift of the lowest energy transition together with a lowering of the oscillator strength. Thus, for a large dihedral angle, the character of the transition of $oCMe^-$ and $pCMe^-$ becomes more like the transition of $mCMe^-$. This is supported by TD-DFT calculations performed as a function of the ϕ_B angle. The calculated transition energies with corresponding oscillator strengths are displayed in Fig. 4.14. It is clear that the oscillator strengths become lower as the planarity is broken and practically vanishes when the angle is 90° . And as expected, the excitation wavelengths shifts towards the red as the angle increases. Also interestingly, the transition energy changes from 412 nm with $\phi_B = 0^\circ$ to 443 nm at 180° .

If $oCMe^-$ is created in the ion source in both these isomeric forms, then this itself might explain the broader profile, although, the barrier is some-

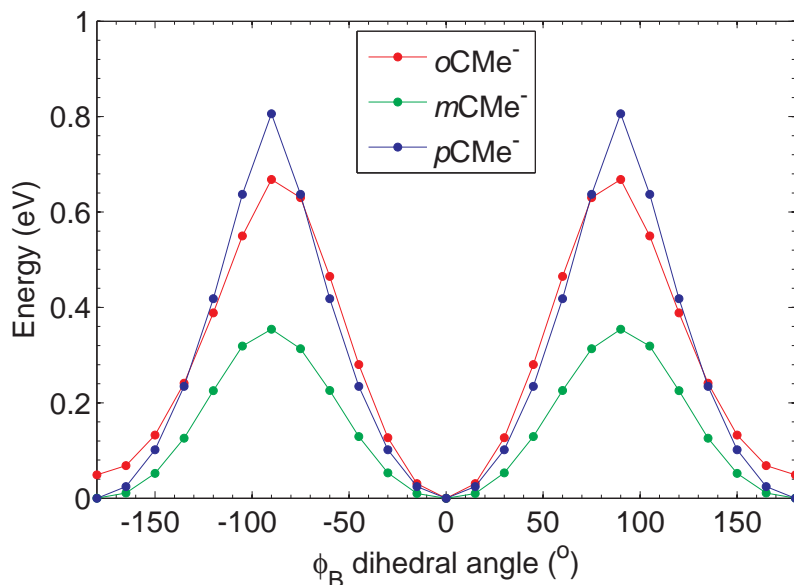


Figure 4.13: The ground state energy as function of ϕ_B for $oCMe^-$, $mCMe^-$ and $pCMe^-$.

what high for that. Both $oCMe^-$ and $pCMe^-$ can rotate up to 45° with the internal vibrational energy at 300 K, however, the change in excitation energy from 0° to 45° is a little larger for the *ortho*-isomer, almost 45 nm, while the shift for *para* is lower than 30 nm. Thus a small rotation has a larger effect on broadening the spectrum for $oCMe^-$ compared to for $pCMe^-$.

The de-coupling of the $oCMe^-$ that happens as ϕ_B increases is also visible in the calculated HOMO and LUMO orbitals. As shown in Fig. 4.15, the orbitals with ϕ_B at 75° are very similar to the HOMO and LUMO of $mCMe^-$, where the de-coupling was large. Moreover, as the angle increases, the absorption is redshifted and the corresponding oscillator strength is lowered, just like the absorption of $mCMe^-$, where the decoupling is 'built-in'.

4.3 Photo-detachment experiments

4.3.1 Experimental details

The experimental setup at ELISA does allow observation of some of the fragmentation channels, however, due to the large acceptance of the stor-

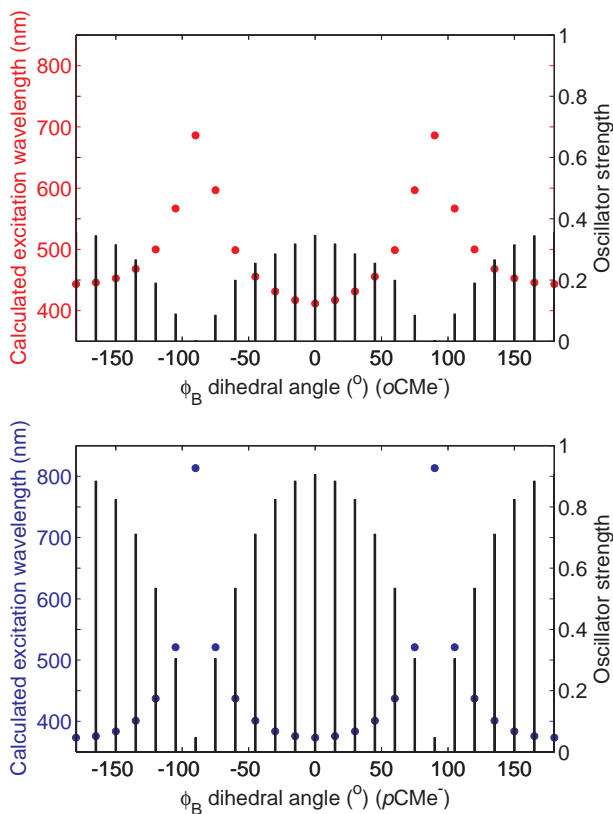


Figure 4.14: On the top is the calculated excitation energies of $oCMe^-$ and the corresponding oscillator strengths as a function of ϕ_B . Below the same is displayed for $pCMe^-$.

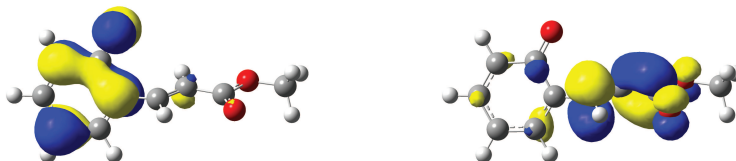


Figure 4.15: The HOMO and LUMO orbitals of $oCMe^-$ with $\phi_B = 75^\circ$.

age ring it is not possible to distinguish fragment masses close the parent mass. In order to observe electron emission, the setup at Separator II is used. The electron spectrometer allows for detection of emitted electrons, even for electrons with very low kinetic energy release (KER). Information about the threshold of electron detachment and the distribution of electron KER's is essential to fully understand the photo-physical properties of the chromophore of the photoactive yellow protein. As mentioned in Sec. 4.1, a vertical detachment energy (VDE) of 2.9 eV has been found by A. H. Zewail and co-workers [29], and most theoretical approaches agree on this value. However, the process by which the electrons are emitted is not clearly explained, neither by experiment nor theory. While the different theoretical methods may agree on the VDE, they diverge when it comes to the excitation energy for the anionic chromophore. Some methods find it to be below VDE and some above, varying from 2.8 eV to 3.4 eV [67]. The process of electron emission is expected to be different depending on which is it. A VDE lower than the transition energy from $S_0 \rightarrow S_1$, means that the excited state in the anion is located in the neutral continuum, and would hence be expected to be unstable towards electron detachment.

The ELISA action absorption spectroscopy experiments does not distinguish between electron loss or fragmentation, however, monitoring the electron KER-distribution as a function of wavelength at SEPII can shed light on the relative position of the states in both the anionic chromophore and its neutral radical. For this purpose the distribution of electron KER's has been measured for the $pCMe^-$ model chromophore, as seen in Fig. 4.16. The experiments were performed at thirteen different wavelengths from 320 nm to 460 nm. Based on the action absorption spectrum for $pCMe^-$, shown in Fig. 4.6, and the available laser intensity, the experiments were performed from 425 nm to 460 nm at 5 nm intervals and at 390 nm, 400 nm and 410 nm, to monitor if the electron KER varies in the $S_0 \rightarrow S_1$ absorption regions. Moreover, the photo-electron experiments were performed at 355 nm, as the laser output is very high at the third harmonic of the YAG, and at 320 nm, since the ELISA experiments revealed a minor absorption maximum at this wavelength. Unfortunately, due to a reconstruction of the laboratory, the time was not enough to allow for long measurements to improve statistics.

Before the reconstructing of the electron kinetic energy distribution for each wavelength, the r-distributions data were smoothed once. This process does not smear out small vibrational features of the electron kinetic energy distributions, since the internal energy of the ion at room temper-

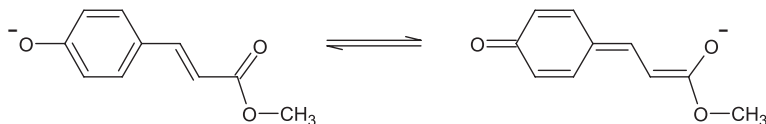


Figure 4.16: The two main resonance structures of the $p\text{CMe}^-$ model chromophore.

ature is in itself high. However, it does improve the general quality of the distributions.

4.3.2 Results

The electron kinetic energy distributions were measured at thirteen different wavelengths. The experimental results at these wavelengths are split into two figures. The first, Fig. 4.17, displays the results with wavelengths from 390 nm to 460 nm, while the second, Fig. 4.19 shows the results at 355 nm and 320 nm.

The observed electron kinetic energy distribution at 460 nm, shown in Fig. 4.17, has a narrow peak at approximately 0.03 eV with a FWHM of roughly 0.07 eV, thus most electrons leave with low kinetic energy. The distribution has a tail towards higher energies, up to 0.25-0.3 eV, that looks exponential. On a log-scale it is close to linear as shown in Fig. 4.18, which indicates an exponential tendency. It is worth noting that the internal energy of the chromophore in the gas-phase at room temperature was found to be 0.26 eV, as shown in Sec. 4.2.3. The electrons emitted at 460 nm, both in the peak and the tail, are emitted through an indirect process, which will be elaborated on in Sec. 4.3.3.

The electron kinetic energy distributions measured at somewhat higher photon energies, at wavelengths from 460 - 425 nm (2.7 - 2.92 eV), look strikingly similar to the spectrum at 460 nm, despite the higher energy of the photons. These spectra display the same narrow peak at low electron energies together with a tail towards higher energies. Although the exponential-looking tails vary a little, the variations are small compared to what happens at higher photon energies. The similarity of the distribution of energies suggest, that the emission channel is the same for all these wavelengths. The difference in energy between a 425 nm photon and a 460 nm photon is 0.22 eV. There is definitely no sign of shifts of electron energy of this order.

However, for wavelengths 390 to 410 nm additional features in the en-

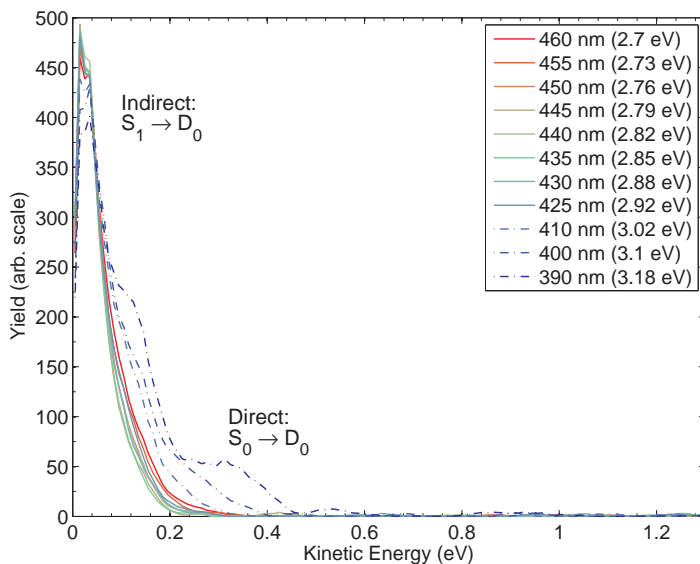


Figure 4.17: The electron kinetic energy release for the $pCMe^-$ model chromophore at select wavelengths from 390 nm to 460 nm.

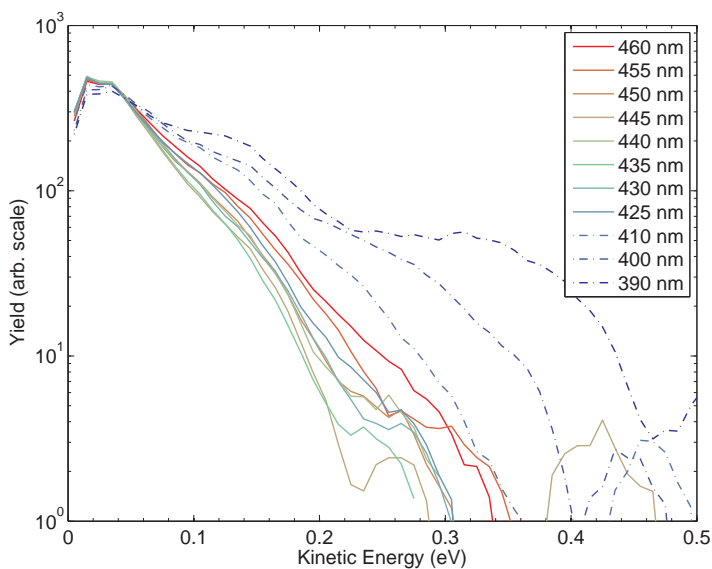


Figure 4.18: The electron kinetic energy release for the $pCMe^-$ model chromophore at wavelengths from 390 nm to 460 nm presented on a log-scale. For wavelengths down to 425 nm the distribution of energies fall more or less linearly from 0.05 eV to 0.25 eV.

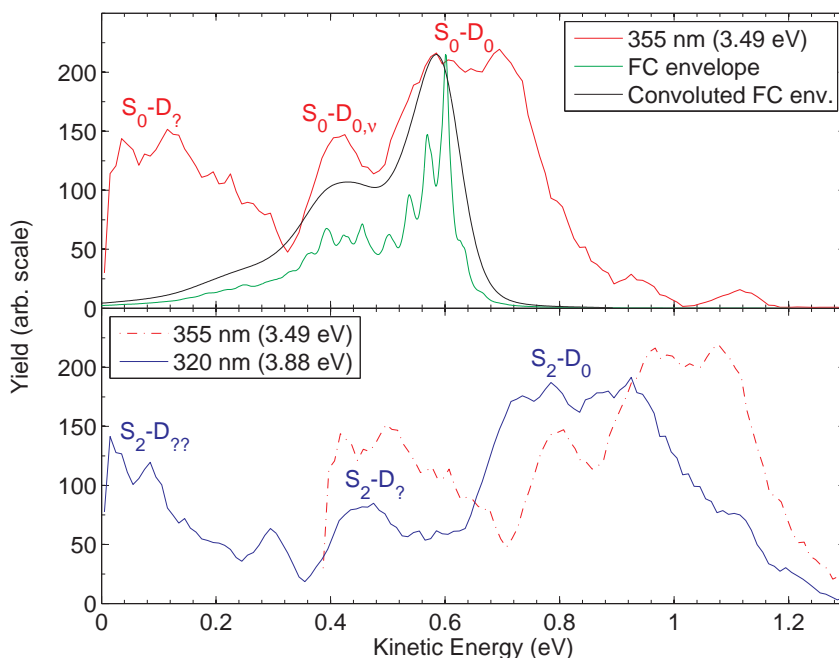


Figure 4.19: The electron kinetic energy release for the $p\text{CMe}^-$ model chromophore at wavelengths 355 nm (top) and 320 nm (bottom). The spectrum at 355 nm has been added to the lower graph with the energy axis shifted with the difference in photon energy between 355 and 320 nm. The calculated Franck Condon envelope is added to the 355 nm spectrum together with the convoluted FC envelope (broadened with the experimental resolution of 0.06 eV).

ergy distribution appear. At 410 nm there appears a shift in the intensity of the tail, while both intensity and the maximum energy increases at 400 nm. At 390 nm a complete shoulder is found from 0.2 - 0.4 eV. The main intensity for these three wavelengths is still in the narrow low energy peak, nevertheless, the appearance of the additional features indicate a change in the emission process. The fact that the electron energy increases with photon energy hints that these are from a direct emission channel. Moreover, it seems that the ratio between direct and indirect electrons increase with higher photon energies. This will be discussed further in Sec. 4.3.3.

As shown in the top graph in Fig. 4.19, at even higher photon energies (355 nm), the electron distribution changes significantly. The narrow peak at low energy and the exponential tail are no longer seen, however, other

interesting features appear. These consist of a broader peak up to ~ 0.35 eV, another broad peak from 0.55 to 0.75 eV, and in between a narrow peak is found at 0.42 eV. From the action absorption spectrum measured at ELISA, it is clear that the absorption cross section is very low at 355 nm. It was, nonetheless, possible to measure electron emission due to the high intensity of the third harmonic of the YAG at 355 nm. Thus, the low cross section for absorption was compensated for by using an intense photon beam.

The results obtained at ELISA together with the observed electron energies, suggest that the process of emission at 355 nm is through a direct channel. The low cross section indicates the lack of a resonant channel. The vertical detachment energy can hence be found from the electron distribution. By matching the experimental spectrum with a Franck-Condon calculation of the theoretical profile for the direct electron emission, then the VDE for the $S_0 \rightarrow D_0 + e^-$ is determined to be 2.88 ± 0.1 eV (431 nm). The theoretical Franck Condon envelope is found by matching the vibrational modes and the geometry for S_0 and D_0 and is shown together with the experimental data in Fig. 4.19. The electrons observed with higher energy at 355 nm are expected to be due to the internal vibrational energy of the chromophore at room temperature.

For even higher photon energy, at 320 nm, the electron energy spectrum once again changes character. Like the distribution found with 355 nm photons, there are three main peaks, a peak in the 0.1 eV region, a peak at 0.45 eV and a broad feature from 0.7 to 1 eV. At a first glance this might look like a shifted version of the 355 nm distribution. The 355 nm distribution shifted by the energy difference between 355 nm and 320 nm photons added to the 320 nm spectrum, however, disproves that idea. Thus the emission channel at 320 nm is different than the direct channel at 355 nm.

4.3.3 Discussion

Returning to the remarkably similar electron distributions at from 425 nm to 460 nm. The process is expected to be due to an indirect emission channel since the electron energy does not increase with increasing photon energy and due to the high cross section for absorption. The exponential tail could suggest the process of emission to be due to thermionic emission from a hot ground state, that is excitation from S_0 to S_1 followed by internal conversion to a vibrationally hot ground state from where the electron is emitted. However, the time-scale of electron emission rules this possible emission channel out. From the ELISA experiment, neutral fragments

were only observed at the prompt detector, which puts an upper limit of the detachment process of $10 \mu\text{s}$. Moreover, the positions of electrons observed in the SEPII experiment indicate that this upper bound is less than nanoseconds. If the electron emission occurred on a time-scale slower than some nanoseconds, then this would show up in the electron distribution on the eMCP detector as a trail of electron-hits towards the centre of the detector. As shown in Fig. 4.20, this is not observed, thus the emission time-scale must be shorter. Moreover, the time-scale for electron emission observed for another PYP chromophore model was on the ps time-scale [29].

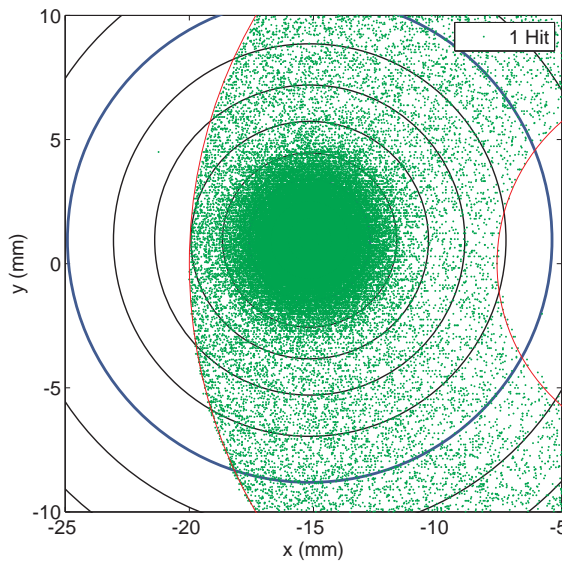


Figure 4.20: The distribution of electron one electron hits on the detector. The red circles show the inner and outer edges of the MCP-detector. The other circles, with centres in the electron hit centre, show the electron energy increasing with 0.1 eV steps.

The emission process was shown not to be thermionic emission, however, the internal vibrational energy of the chromophore does actually play an important role in the emission process. As the VDE is found to be $2.88 \text{ eV} \pm 0.1 \text{ eV}$ (431 nm), emission of electrons would not be expected at wavelengths higher than this value. Electrons are, despite the apparent lack of energy, emitted at lower energy. This is possible due to the internal vibrational energy of the chromophore before excitation. Thus, when

entering the electronically excited S_1 -state, the ~ 0.26 eV of vibrational energy can be redistributed around the chromophore and coupled into electronic energy allowing emission of an electron from the excited state, a process known as vibrational auto-detachment (VAD). Below the VDE, the process of VAD is needed for detachment, above VDE however, this process is not necessarily needed, since the photon in itself carries enough energy. The distribution of electron energies nonetheless stay the same up to 425 nm, which means that even with extra vibrational energy, the emission channel between S_1 and D_0 is the same. For higher photon energies, 410 nm to 390 nm, the direct emission channel begins to show in the spectra. The reason it appears in this region, can be explained by the difference in dipole transition moment for the resonant process of excitation into the S_1 state compared to the direct process of emission from S_0 into $D_0 + e^-$. $|\langle \Psi_{S_0} | \bar{\mu} | \Psi_{S_1} \rangle|^2$ vs. $|\langle \Psi_{S_0} | \bar{\mu} | \Psi_{D_0} \Psi_{e^-} \rangle|^2$. Thus, when the Frank-Condon overlap between the S_0 and S_1 states is not negligible, the indirect process of electron emission dominates. At 355 nm the FC-overlap is negligible, which is why the direct emission channel is the main electron emission channel.

Since the emission process down to at least 400 nm is primarily by detachment through the excited state in the anion, it is not possible to get a proper estimate for the VDE from these electron energy distributions. The reason is that the coupling for higher wavelengths borrows energy from vibrations to emit the electron, while excess energy at lower wavelengths are left as vibrations in the neutral radical. Hence if the VDE was found from the spectrum at 460 nm (2.7 eV) one would get a VDE of 2.6 eV (2.7 eV $-$ 0.1 eV), while the same procedure at 400 nm (3.1 eV) would yield a VDE of roughly 2.9 eV (3.1 eV $-$ 0.2 eV). Neither matches exactly the value estimated from the 355 nm experiment, where the electron detachment occurs via the direct channel. By measuring the electron spectra at only one wavelength, where the process of electron emission can possibly be from a non-direct channel, it is simply not possible to confidently pinpoint the vertical detachment energy. It may help to cool the ions before probing with photons, but it does not solve the issue with indirect channels perturbing the picture.

From the electron spectra at wavelengths where the indirect channel dominates, it is possible to learn about the coupling between the anionic states and the neutral radical states. The process at 320 nm is expected to be primarily indirect, that is, through the excited S_2 state of the anion. The

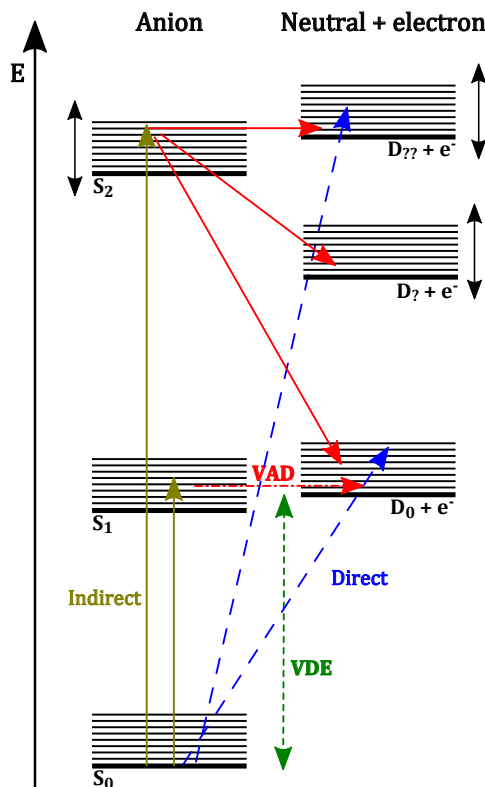


Figure 4.21: A diagram displaying the relative energies of ground and excited states in both anion and neutral radical of the $pCMe^-$ chromophore. Relevant transitions for the photo-electron energies have been added.

electrons are primarily emitted with high energy, leaving the neutral radical in the ground state, $S_2 \rightarrow D_0$, as seen in Fig. 4.19. The feature attributed to this emission channel is very broad, which indicates a broad FC-overlap between the second excited state in the anion and the ground state in the neutral. The electron kinetic energies at both 355 nm and 320 nm indicate that one or more excited states in the neutral radical are available with these higher energies. This however, needs to be verified or disproved by theoretical calculations. The anion can thus end up in one of these neutral radical states D_7 and D_{77} , however, with lower probability. A very interesting piece of information gained from this spectrum, is that the narrow peak at low energy is not really visible in the 320 nm spectrum. Besides emitting an electron, another decay channel from the S_2 -state is internal conversion

to S_1 (and then S_0). However, this process seems to be less likely than emitting an electron from S_2 , since the signature of electron emission from S_1 , the narrow peak at low energies, is not seen. The above mentioned transitions can be found schematically in Fig. 4.21.

In a previous experiment at ELISA, it has been shown that the $pCMe^-$ chromophore ion can fragment upon excitation [69]. Thus electron detachment is not the only decay channel for the excited anion. The fragment at 430 nm was found to have a mass to charge ratio of 146 ± 2 amu/e, and from a theoretical approach it is most probably due to loss of CH_2O . Fragmentation is a statistical process that occurs after internal conversion to the vibrationally excited ground state, while the process of electron detachment happens from the excited state. This implies that there is a competition in the excited S_1 state of the anion between internal conversion and electron emission. It has been shown for a similar PYP model chromophore, with CH_3 instead of OCH_3 , that 20% of the time the excited chromophore decay by electron emission at 400 nm, while the main decay pathway is internal conversion [29]. For another model chromophore, with OH instead of OCH_3 , it was shown that 69% of molecular decays upon photo-excitation occurs at a rate of 2 ns with a no recoil, which most likely is electron loss. These combined results show that both internal conversion and electron emission occur with more or less the same probability.

4.4 Conclusion

Measuring the photo-electron spectra of the chromophore from PYP at several wavelengths has given insight into the process by which the electrons are emitted. It was argued that due to the similarity of the electron energy distributions in the region from 460 nm to 425 nm and the shape of the distributions, the electrons are emitted from the excited S_1 state by an indirect process. The vertical detachment energy was found at 355 nm to be 2.88 ± 0.1 eV (431 nm). At wavelengths above this value the photon energy itself is thus not enough to cause electron detachment, however, it is possible due to vibrational auto-detachment. Upon excitation, the internal vibrational energy of ~ 0.26 eV at room temperature is redistributed through out the molecule, and some of the energy can be coupled into electronic energy in the process of auto-detachment. At wavelengths 410 nm to 390 nm, the cross section for resonant absorption into S_1 lowers, which shows as an increase in the number of electrons with higher energy. The in-

direct channel through the excited state is, nonetheless, still the dominant emission process. At 355 nm the indirect channel is closed and detachment occurs directly into the neutral radical from the anion ground state. At even higher photon energies, at 320 nm, another resonant absorption channel is open, the $S_0 \rightarrow S_2$ transition. This is evident by the increase in the action absorption spectra, but also in the distribution of electron energies. The electron energies measured at 320 nm are primarily due to emission from the S_2 state into one of several neutral radical states, thus the spectra deliver information about the relative energies of the states and the FC-overlap between them.

Interestingly it is evident from the electron distributions from 460 - 400 nm, that it is not possible to determine the vertical detachment energy at these energies, since the process is not direct. The vibrational energy of the anion and neutral radical is part of the process of electron emission. thus by estimating the VDE from these wavelengths, anything from 2.6 eV to 2.9 eV could be found.

The experimental action absorption cross section spectra for the three PYP chromophores have shown that within the visible region, the *para*- and *ortho*-isomers absorb similarly, whereas the *meta*-isomer has a dramatic change in the absorption profile. This was argued to be because of a lower electronic coupling for $mCMe^-$ between the two sub-systems making up the three chromophores. The result of this decoupling was a red-shift of the first transition, a CT-transition, with a very low oscillator strength. Moreover, it was argued that the bright absorption band seen in the UV-region for $mCMe^-$, was more or less localized on the two sub-systems. For $oCMe^-$ and $pCMe^-$ the absorption maximum in the visible were almost coinciding, however with a three times larger oscillator strength for $pCMe^-$. Moreover, the wider profile of the $S_0 \rightarrow S_1$ -band of $oCMe^-$ was attributed to the possible presence of several different rotamers in the ion bunch.

The green fluorescent protein

5.1 Introduction

The discovery of fluorescent proteins, especially the green fluorescent protein (GFP), has had a huge impact on biological research. By using the fluorescent proteins as markers, it is possible to follow biological processes in living cells, making a broad variety of interesting experiments possible [2]. The discovery of the green fluorescent protein was reported in 1962 as a side benefit in a study on the bioluminescence of another protein, aequorin [71], both found in the jellyfish, *Aequorea victoria*. The genes expressing the GFP in the cell were since cloned and used to express fluorescence in different species [72, 73]. The fact that it the GFP protein does not need any specific enzymes to form and that it does not otherwise influence the cell in which it is expressed, is one of the advantages of GFP for use as a bio-marker.

Since it was shown that GFP could safely be expressed in other cells, it has been used for a wide variety of studies. The possibility to track processes in living cells allow for gaining better insight into the dynamics of cells, for instance cancer cell growth [74, 75]. And with the advances in experimental techniques, GFP can be used for sub-diffraction limit microscopy [76]. Or if one so desires, it is possible to clone green fluorescent mice [77] and even to buy fluorescent zebrafish [78].

By altering the chain of amino-acids that composes the GFP, the photo-physical properties of the protein also changes. In this manner a myriad of GFP-like proteins have been designed rendering it possible to find a fluorescent probe to match most experiments. The importance of the finding

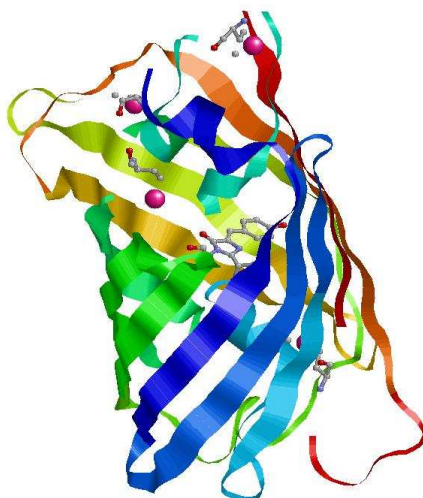


Figure 5.1: The green fluorescent protein. Inside the β -barrel, the chromophore is depicted as a ball and stick model. Figure created with RasMol from PDB ID: 1EMA [79].

of and the work done on GFP was manifested by the Nobel committee in 2008. The Nobel Prize in chemistry was this year given to Professor O. Shimomura, M. Chalfie and R. Y. Tsien ‘for the discovery and development of the green fluorescent protein, GFP’ [80].

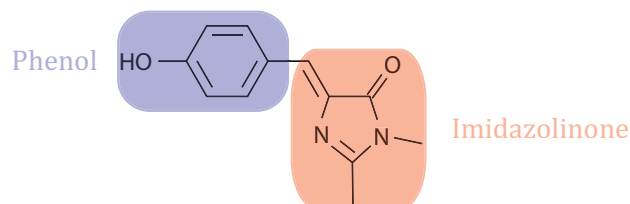


Figure 5.2: The neutral version of the chromophore as found inside the green fluorescent protein. The chromophore consists of two units: a phenol- and an imidazolinone-part, linked together by a C-bridge.

The green fluorescent protein consists of 238 amino acids that fold into an 11-stranded β -barrel, in which the chromophore is positioned in an α -helix as shown in Fig. 5.1. The chromophore found within the protein is a *p*-hydroxybenzylideneimidazolinone moiety *p*HBI [72, 81], that is formed

from three of the amino acids, S65, Y66 and G67 [72]. the neutral version of the most studied model for the chromophore as depicted in Fig 5.2. The absorption profile of the protein displays two distinct absorption peaks at 395 nm and 475 nm [82]. Excitation at one of these two wavelength-regions is followed by fluorescence with peaks at 503 nm (475 nm absorption) and 508 nm (395 nm absorption) [83]. The fluorescence quantum yield is remarkably high - 0.77 [84]. The first of the two absorption maxima, 395 nm, is attributed to the chromophore being in its neutral form, A, and the other, 475 nm, to the deprotonated form, B, as shown in Fig. 5.3 [83].

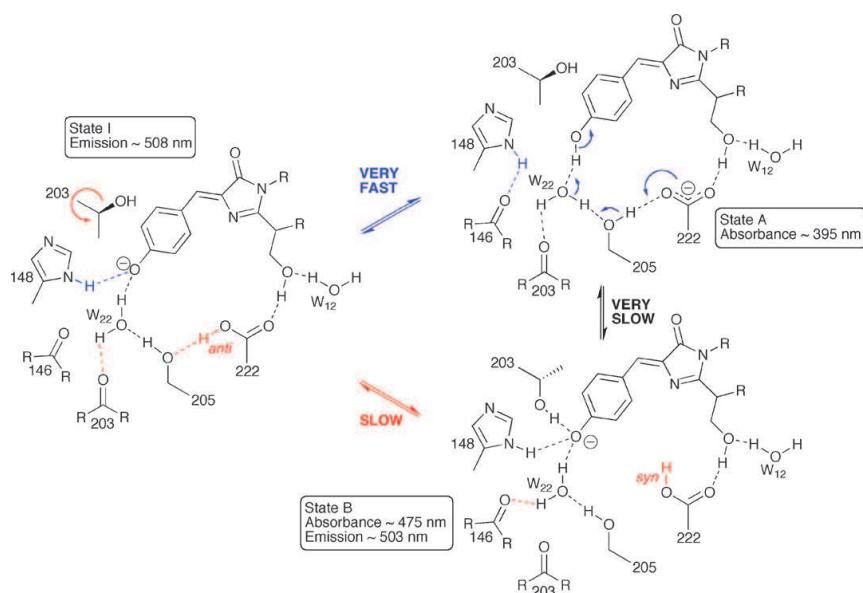


Figure 5.3: The states, A, B and I, responsible for the absorption and fluorescence of the green fluorescent protein. Reprinted from [83].

Upon excitation in this neutral state, A* the chromophore acts as a photo-acid, and the network of hydrogen bonds surrounding the chromophore changes, leaving the chromophore in an anionic state, I*. In this state, the chromophore emits light $I^* \rightarrow I$ and returns to the neutral state $I \rightarrow A$ [85]. In some cases, however, the excited intermediate I^* ends up in another excited anionic state, B*. This state, B, is responsible for the 475 nm absorption. By prolonged exposure to light at 395 nm, the intensity of the 475 nm absorption peak increases, while the 395 nm peak lowers in intensity [86]. Thus, following intense exposure to 395 nm light most of the proteins end up in the the anionic state B at the expense of the neutral state

A.

To gain insight into the photo-physical properties of the green fluorescent protein it is useful to isolate the chromophore and study it without the protein surroundings. For this purpose the *p*HBDI model chromophore has been studied in various solvents [8, 12]. For both the neutral form and the anionic form the general trend is that the solution phase spectra show a blueshifted absorption compared to the protein spectra.

The photo-physical properties of GFP has also been studied by means of theoretical methods. A lot of effort have been put into understanding the excitation process, $S_0 \rightarrow S_1$, and the dynamics in the excited state of the chromophore [87, 88], adding information that is hard to get by experiments alone. The value for the excitation energy has been a point for comparing the theory to experiment. Different approaches can yield very different results for the transition wavelength, 284 nm to 558 nm [89–91]. A recent approach calculate the vertical excitation energy to be 475 nm (2.61 eV) [67]. The vertical detachment energy of the anionic chromophore has also been a point of interest. The value for VDE for the bare chromophore in three recent works was calculated to be 2.54 eV [92], 2.5 eV [93] and 2.62 eV [94]. Thus they agree with each other within the uncertainties of the calculations (0.2 eV). Interestingly it is also shown that the surrounding protein stabilizes the anionic chromophore against electron detachment [93] by increasing the vertical detachment energy without perturbing the vertical excitation energy. Although the protein is found to stabilize against photo-detachment, the value of the vertical detachment of the bare chromophore is of great interest. First, as a comparison point between theory and experiment, but second and more importantly, for the general understanding of the dynamics in the excited state of the chromophore anion. Moreover, it has recently been shown, that electron transfer within GFP can be driven by light [95].

Another method to study the chromophore without the protein surrounding is by isolating the chromophore in the gas phase. In this manner the intrinsic properties of the chromophore can be studied. Gas-phase action absorption experiments have been performed on the *p*HBDI model, both as anion and cation. The absorption maximum of the protonated version of *p*HBDI showed a maximum at 406 nm [36]. From a study of six ‘neutral’ models with a positive spectator charge, the absorption maximum for the neutral chromophore has been estimated to be 349 nm or 399 nm, depending on theoretical method. In the anionic form *p*HBDI has been shown to have an absorption maximum in the region of 479–482.5 nm

[36, 37, 96–100]. This maximum practically coincides with the value for the protein, 475 nm, which suggest that the protein pocket might serve as a very gentle environment for the chromophore. A recent experiment by Forbes *et. al* [97, 99] has found the shape of this peak to be quite different from what was shown by the storage ring experiments [36, 37, 96, 98, 100]. The storage ring experiments show a single peak at ~ 480 nm, while the absorption profile found in the quadrupole ion trap mass spectrometer experiment shows features down to wavelengths below 400 nm. These extra features were attributed to electron detachment.

Recently, the photo-electron spectrum of the anionic chromophore has been measured in different experiments. One experiment estimates the vertical detachment energy to be 2.8 eV (443 nm), while the adiabatic detachment energy is 2.6 eV (477 nm) [31], suggesting that the excited state in the anion lie just below the threshold for electron detachment. The other experiment find that the VDE is 2.85 eV, while the adiabatic detachment energy is 2.8 eV [30].

Within the protein, the chromophore is being perturbed by the surrounding amino acids. In order to study how the interactions between the chromophore and the protein affects the photo-physical properties of the chromophore, a useful approach is to study chemically modified versions of the molecule. This has been done by adding a charged ‘tail’ to the *p*HBDI model, in an effort to study the ‘neutral’ chromophore when influenced by a spectator charge. Combining the experimental results with theoretical models yield an estimate for the absorption of the neutral chromophore of 349 nm and 399 nm, depending on the theoretical method [101]. On the same note, the effect of a hydrogen bond in the anionic chromophore and a substitution of a hydrogen with bromine on the phenolate showed no change in the absorption maxima [98].

5.2 Photo-detachment experiments

5.2.1 Experimental details

The photo-electron spectra of the *p*HBDI anion was, identically to the experiment conducted on the PYP chromophore anion, measured at several wavelengths at SEPII. The experiments were performed concurrently with the photo-electron experiments on the GFP chromophore anion in two other laboratories [30, 31]. The photo-electrons were measured in the same manner as the photo-electrons for the PYP chromophore, however

at slightly different wavelengths. The experiment was performed with the following wavelengths: 500 nm, 480 nm, 440 nm, 425 nm, and 355 nm. With these wavelengths, electrons from both the red and the blue part of the $S_0 \rightarrow S_1$ absorption peak were measured, together with electron at a wavelength far from this resonant transition.

5.2.2 Results

The experimental results for the photo-electron experiments on deprotonated *p*HBDI are shown in Fig. 5.4. The similarity to the experimental results for the PYP chromophore model is striking. At 500 nm, 480 nm and 440 nm most electrons are emitted with a low energy, with the peak of the distribution found at ~ 0.05 eV. Similarly to the results for *p*CMe⁻, the distribution has a tail towards higher energies, for *p*HBDI out to roughly 0.4 eV. This matches the internal energy of *p*HBDI at room temperature ~ 0.3 eV, estimated on the basis of calculated vibrational energies. The electrons emitted at these wavelengths are most likely due to an indirect emission channel through resonant excitation to the S_1 -state followed by electron emission.

The distribution of energies at 425 nm still has a peak at ~ 0.05 eV, however, it shows a higher probability of emission of electrons with energies of 0.15 eV - 0.4 eV than at higher wavelengths. The rise in the number of electrons at these energies is probably due to direct emission. Thus, at this wavelength there is a competition between the transition to S_1 and direct electron emission due to a poorer FC-overlap between S_0 and S_1 further away from the resonance.

At 355 nm the observed spectrum shows no sign of electrons with low energy. The distribution of electron energies is shifted to have a maximum close to 0.8 eV. This distribution of energies is due to electrons emitted in a direct process, $S_0 \rightarrow D_0 + e^-$. The spectrum at 355 nm for *p*HBDI contains only one peak, quite differently from what was seen for *p*CMe⁻, although this spectrum was also expected to be due to direct detachment. The vertical detachment energy of *p*HBDI can be found from the convoluted FC distribution and the experimental data. This convolution of the theoretically calculated FC-spectrum has to be performed due to the lower resolution of the experiment. Hence, the theoretical points are widened by Gaussian distributions with a width of 0.06 eV. The convoluted data can only determine the shape of the spectrum, not the energy. From the correlation between the theoretical and experimental distribution, the VDE can be estimated to

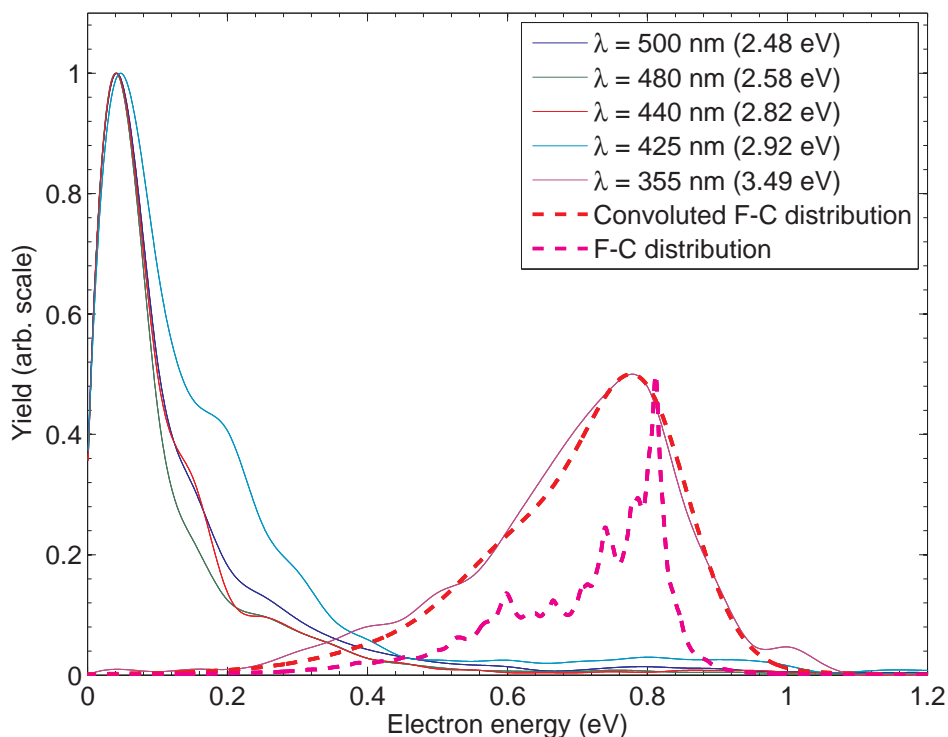


Figure 5.4: The photo-electron energy distributions for the *p*HBDI anion. The experimental data are shown together with the calculated distribution at 355 nm. The calculated distribution Franck-Condon distribution is shown both with and without a convolution with the experimental energy resolution (0.06 eV).

be 2.68 ± 0.1 eV. Had the VDE been estimated from the peak position only, the estimate would have been 2.72 eV.

5.2.3 Discussion

The vertical detachment energy of $2.68 \text{ eV} \pm 0.1 \text{ eV}$ corresponds to a wavelength of 463 nm. Thus, electron emission would not be expected at 480 nm or 500 nm, since the photon energy is too low. Nonetheless, electrons are observed at photon energies below the VDE. The electrons emitted with wavelengths from 440 to 500 nm are primarily emitted from the excited state of the anion, S_1 . This indirect emission process together with the in-

ternal energy of a little more than 0.3 eV, are the reasons that it is possible to emit electrons at photon energies below the VDE.

Similarly to what was seen for the PYP chromophore anion, electrons can be emitted from the excited S_1 -state in *p*HBDI by vibrational auto-detachment. As was discussed in Sec. 5.1, electron emission is not the only reaction pathway from this excited state, internal conversion to the vibrationally hot ground state possibly followed by fragmentation is also possible. This channel does, however, become less prominent as the photon energy increases and above the VDE (463 nm) the primary decay mechanism from S_1 is by electron emission, see Sec. 5.5.3. The electron distribution is, nonetheless very similar from 500 nm to 440 nm, which suggest, that the electron emission is indirect although 440 nm is above the VDE.

At 425 nm the electron kinetic energy distribution starts to show contribution from direct detachment, indicated by the shoulder at ~ 0.2 eV, extending out to 0.5 eV. Most electrons are still emitted through the resonant indirect channel, however, as the Franck-Condon overlap between the S_0 and S_1 electronic states lowers, the direct channel becomes more prominent. This is evident at 355 nm, where the contribution from the resonant transition is expected to be vanishing. The distribution of electron energies, shows no sign of low energy electrons, however, a broad peak with the maximum just below 0.8 eV has appeared. This is the signature of the direct emission from S_0 into $D_0 + e^-$.

The distribution of electron energies at 355 nm have also been measured by Horke *et. al* [31]. Although, the two spectra are very similar they estimate the VDE to be 2.8 ± 0.1 eV (and get the same value with 268.1 nm and 201.5 nm), which is 0.12 eV higher than the estimate based on the spectrum presented in Fig. 5.4 and the theoretical FC envelope. From the experimental data presented in this figure, the VDE based on the maximum of the 355 nm spectrum would be somewhat higher than 2.68 eV, but not 2.8 eV. Mooney *et. al* has also measured the electron kinetic energies of the GFP model chromophore, but at 269 nm and 330 nm [30]. They estimate the VDE to 2.9 eV from detachment at 330 nm and 2.85 eV at 269 nm, with their best estimate of the VDE being 2.85 eV. Common for all these values is that the neutral radical ground state D_0 lies above the first excited state in the anion S_1 , which is found to be 2.6 eV theoretically [91] and from the experiments to be ~ 2.58 eV (~ 480 nm) [96, 97].

In the other two works on the photo-electron spectroscopy on the GFP chromophore anion, the possibility of emitting electrons from the vibrationally hot ground state (following excitation, internal conversion and

internal vibrational redistribution) - thermionic emission. Although this might be possible, the time-scale for the process of electron emission is very fast for GFP. The time-of-flight from laser interaction until the ion bunch has passed through the hole in the electron MCP detector can be estimated to be roughly 1.5 μs for the GFP anions. Since no smearing towards the hole in the electron MCP detector is seen for the GFP electron data, then the electron emission is expected to happen on a much faster time-scale ($<\text{ns}$). Although it may be possible to funnel this much energy from the nuclear motion into electronic energy on a short time-scale, it probably requires some specific coupling mode for this to be possible. Moreover, the fact that fragmentation is observed and occur with a lifetime of $\sim 30 \mu\text{s}$ after absorption of two 430 nm photons, does not match the idea of having fast thermionic emission from a hot ground state after absorption of one photon. If thermionic emission occurs (much) faster than 1.5 μs after absorption of one photon, then one would expect this to be much faster with the energy of two photons, leaving no chance of fragmentation.

In this work, no sign of higher lying states in the neutral radical are seen. This is, however, simply because the photon-energy is too low to reach these states. When probing with photons at 268.1 nm and 269 nm the signature of the first excited state in the neutral radical is seen as electrons with lower energy. From the experiments, the binding energy of the electron is estimated to be 4.1 eV [31] and 4.08 ± 0.1 eV [30]. Moreover, Horke *et. al* [31] shows by probing with 201.5 nm photons, that further neutral excited states can be reached. The photo-electron results for the model chromophore for PYP discussed in Sec. 4.3.3, showed that care has to be taken with photo-electron spectra where higher-lying states in the anion are reachable with the photon-energy. As the action absorption spectra measured at ELISA shows, Fig. 5.13 in Sec. 5.5.2, the cross section increases at ~ 340 nm to reach a maximum at ~ 315 nm (3.95 eV). This peak is due to the opening of S_2 and S_3 in the anion and D_1 in the neutral radical [102]. The possibility of reaching higher-lying states with the photon-energy could be the reason that the photo-electron spectra at 201.5 nm and 268.1 nm in the work of Horke *et. al* [31] have quite different shapes. Furthermore, the possibility of reaching the second excited state and emitting electron from this state, as is also discussed by Mooney *et. al*, might explain the increase in electron counts on the high energy part of the D_0 -channel at 268.1 nm and 269 nm, when compared to distributions at 355 nm and 330 nm, as seen in [30, 31].

From the experiments presented in this work and the two above men-

tioned experimental works, it is evident that a VDE below 2.6 eV is hard to match with the data. This would require the FC envelope in Fig. 5.4 to be shifted towards higher electron kinetic energies. However, then the match between the experimental and the calculated shape is not good. Thus the VDE is most likely higher than 2.6 eV. This means that the first excited state of the anion, S_1 , lies lower in energy than the neutral radical ground state, D_0 .

5.3 Absorption experiments

5.3.1 Experimental details

The chromophore from the green fluorescent protein, *p*HBDI, has been studied previously at ELISA [36, 37, 96] as both anion and cation. These experiments were performed in the visible region and with the use of the MCP-detector. Thus, any prompt action was not seen in the experiments. In order to study this prompt process of the anionic form of *p*HBDI and its *meta*-derivative, *m*HBDI, the experiment has been repeated with the use of the prompt detector, the glass plate detector, SED. Similarly, to study the *meta/para*-effect in both the anionic form and the cationic form, deprotonated and protonated that is, the action absorption spectra of both cationic isomers have been measured. All spectra have been measured in both the visible and the UV-region. Structures for the four models are shown in Fig. 5.5.

For the cationic forms, the experiment have been performed by using the MCP detector only. This was chosen, since the experiments in the UV-region are very time consuming to perform using the prompt detector, as the experiments have to be performed with crossed beams in order not to destroy the coating on the glass plate. The spectra were measured from 210 nm and up, with a gap from 355 nm to 380 nm. In this region the available energy of the laser pulses was not adequate to perform the experiments.

For the anionic forms, the possibility of electron detachment required that the experiments were performed with use of the prompt detector, thus the experiment was performed with crossed beams in order to protect the detector.

Furthermore, power dependences were performed at selected wavelengths in order to establish the number of photons were required to cause

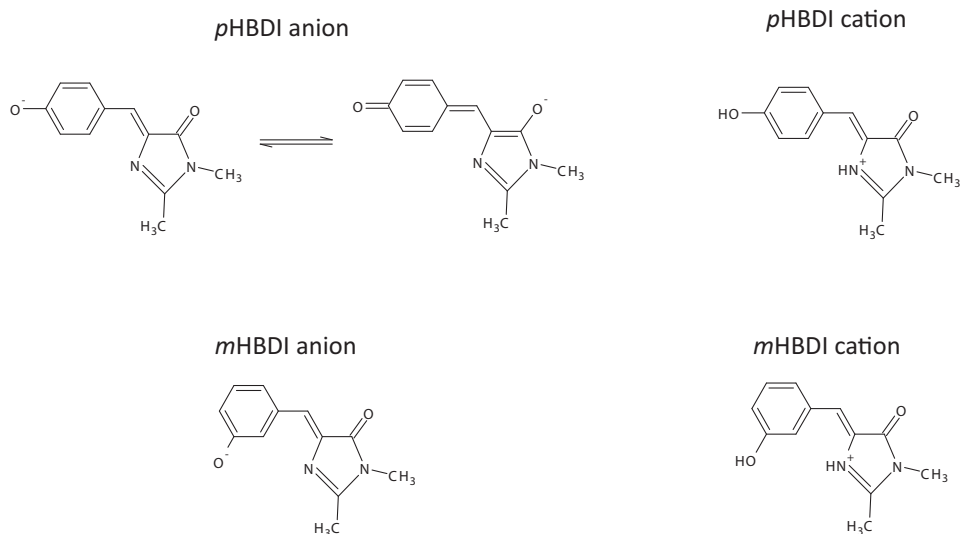


Figure 5.5: The structures of the models for the chromophore from the green fluorescent protein. The *para* HBDI anion is shown with both the two main valence resonance structures.

neutralization. This is important for the treatment of the data for the action absorption cross sections.

5.4 Absorption experiments - Cations

5.4.1 Power dependences

The power dependence of the *m*HBDI model chromophore was performed at two wavelengths, 263 nm and 430 nm. It would have been good to have performed several power dependences in the wavelength region between these values, but unfortunately a combination of low laser output and/or low cross section did not allow for this. The power dependence of the *p*HBDI cation was performed at 410 and 430 nm, with different laser systems. It was previously shown to be dependent of wavelength and that at 410 nm, two photons are required to cause dissociation.

The power dependences for *m*HBDI are shown in Fig. 5.6. The yield at 430 nm have been fitted to a Poisson distribution, see Eq. 2.4, with $n = 2$, while the yield at 263 nm fits with a distribution with $n=1$. This means that in between these wavelengths the decay changes from requiring the en-

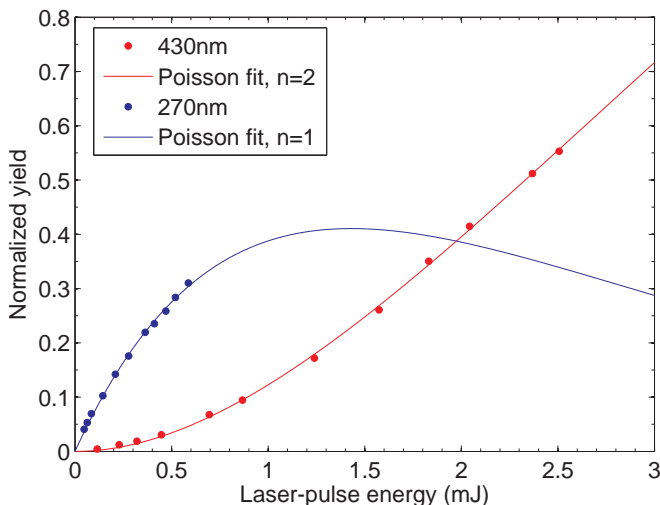


Figure 5.6: The power dependences of protonated *m*HBDI performed at 263 nm (blue) and 430 nm (red).

ergy of two photons for dissociation to happen to requiring only one photon. It is also clear from typical storage spectra in ELISA, that the number of photons required to cause dissociation does change with wavelength. Two typical storage spectra are shown in Fig. 5.7. At 430 nm the lifetime is $\sim 30 \mu\text{s}$, while the lifetime at 270 nm, somewhat counter-intuitively, is $\sim 450 \mu\text{s}$. The longer lifetime at higher photon-energy is explained by the power dependences. Two photons at 430 nm has more together than one at 270 nm, actually more than one eV in excess, 5.79 eV vs. 4.59 eV .

The power dependence performed on the *m*HBDI chromophore at a wavelength of 430 nm shows a clear two-photon dependence, see Fig. 5.6. The fit to a Poisson distribution fits perfectly with $n=2$. This tendency is clearly supported by the shorter lifetime found at 430 nm than at 270 nm.

The *p*HBDI model was previously shown to require the energy of two photons to dissociate. The power dependence was repeated at 410 nm and 430 nm and at both wavelengths it was concluded that energy of two photons were required to cause dissociation. From typical storage spectra it was clear that the tendency for *p*HBDI was the same as for *m*HBDI when going towards shorter wavelengths.

In the analysis of the action absorption results, the data for both isomers have been treated as a two-photon dissociation process at wavelengths

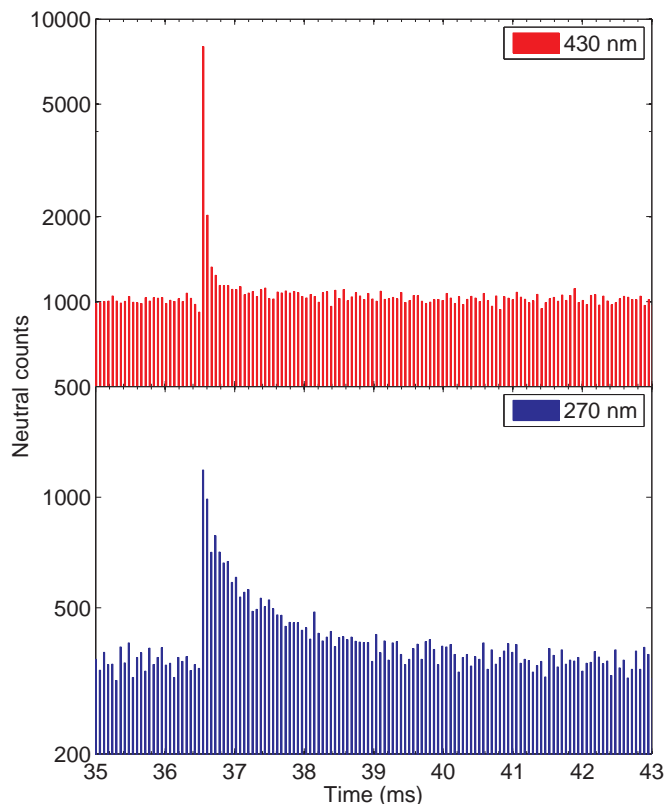


Figure 5.7: A typical storage spectrum of *m*HBDI at 270 nm and 430 nm. The lifetime upon absorption of one 270 nm photon is $\sim 450 \mu\text{s}$, while two photon absorption at 430 nm results in a lifetime of $\sim 30 \mu\text{s}$ for the chromophore.

above 380 nm, while for wavelengths below 355 nm they have been treated as a one photon process.

5.4.2 Action absorption spectra

On the basis of the power dependences, the experimental results for 380 nm and higher wavelengths have been treated as requiring two photons to cause dissociation. The results of the action absorption experiments in the visible range are found in Fig. 5.8.

The spectrum for *p*HBDI shows two close-lying absorption peaks. The

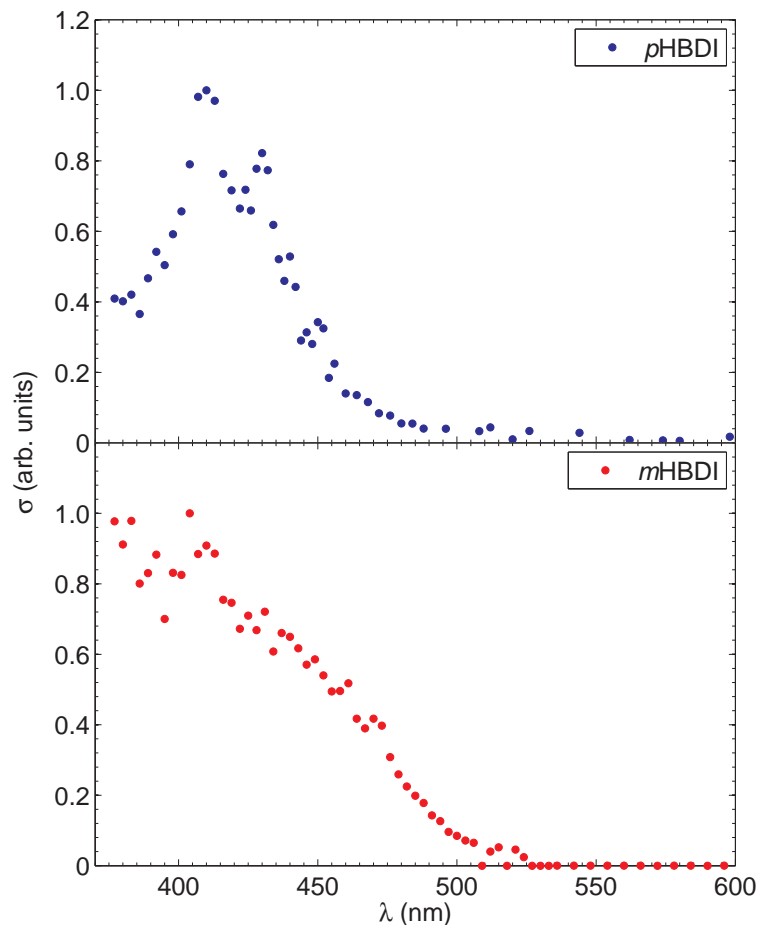


Figure 5.8: Action-absorption spectra of the two protonated chromophore samples at visible wavelengths. The upper graph shows the spectrum for *p*HBDI, the lower displays *m*HBDI.

most intense absorption is found at 410 nm (3.02 eV), while the second peak has its maximum at 430 nm (2.88 eV). The cross section for absorption falls towards smaller wavelengths, but is non-zero at 380 nm. At higher wavelengths the absorption is practically zero from 480 nm and upwards. The presented action absorption spectrum for *p*HBDI, does not completely agree with the previously measured spectrum [36]. In the older spectrum, only one peak at 406 nm was resolved. The difference in the two spectra

can be explained by the different laser setup being used. With the old laser setup, a spectrum below 410 nm could be obtained without changing the overlap of laser and ion bunch, and similarly a spectrum above 410 nm. Thus the experimental spectra have to be merged at this wavelength. This could be a reason why the 430 nm was not resolved earlier. Unfortunately, with the current EKSPLA laser setup a similar merging of spectra has to be performed at 420 nm. For this reason the experiments were repeated with another laser setup, the SPECTRA Physics laser system. For this system the merging is done at 440 nm. Fortunately, the spectra with both current laser systems, EKSPLA and SPECTRA Physics, could resolve both peaks.

The action absorption spectrum of protonated *m*HBDI does not show the same features as was seen for the *p*HBDI isomer. The absorption profile is very broad, extending out to 500 nm and with absorption down to 380 nm. There is a small peak at 410 nm (3.02 eV), although it does not clearly stand out from the broad peak.

The action absorption spectra measured at wavelengths below 355 nm have been treated as being one-photon dependent. The observed cross sections in the UV range are displayed in Fig. 5.9. The spectrum for *p*HBDI shows no sign of absorption from 300 nm to 355 nm, however there are two peaks at 257 nm (4.82 eV) and 229 nm (5.41 eV).

The action absorption spectrum of *m*HBDI shows, that the cross section is low, however, it does not go to zero in the range from 290 nm to 355 nm. From typical storage spectra it is evident, that this is not due to a bad background-subtraction. This model chromophore also has two absorption peaks in the UV range. One at 262 nm (4.73 eV) and another broader peak at \sim 214 nm (5.79 eV).

5.4.3 Discussion

The spectrum for *p*HBDI in the visible range, Fig. 5.8, shows two close-lying absorption maxima. As explained in the previous section, these have not been resolved in the earlier experiment [36] due to the laser setup used for that experiment. These two peaks can be assigned the two isomeric forms of the cation. By an isomerization around the C=C double bond to the imidazolinone ring two the model changes its absorption properties. The size of the conjugated system does essentially not change, however, due to steric constraints one is planar and the other not. This is due to the proton added to the nitrogen, which means that it is not energetically favoured to be in the planar configuration in the *cis*-configuration.

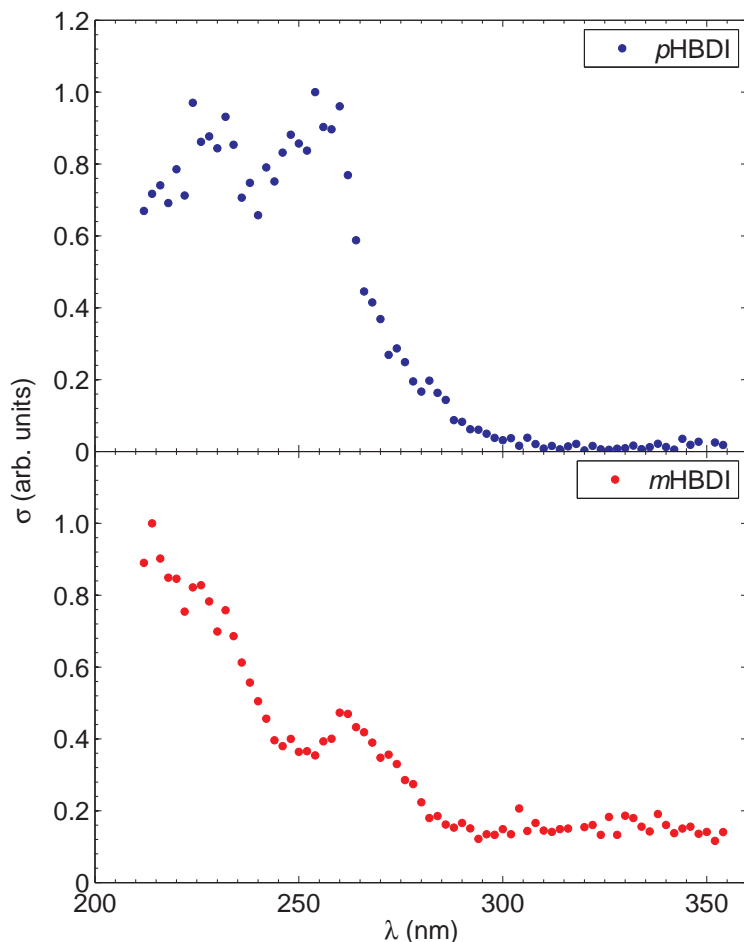


Figure 5.9: Action-absorption spectra of the two protonated chromophore models in the UV range. The upper graph shows the spectrum for $pHBDI$, the lower displays $mHBDI$.

As shown in Fig 5.10, for the non-planar *cis* the excitation energy can be calculated to be 418 nm, whereas the planar *trans* is redshifted compared to this, with a calculated absorption of 448 nm.

The barrier for performing this isomerization process in the gas phase have been estimated at the B3LYP 6-311+G(d,p) level of theory. These numbers are meant as guidelines only, as a multi-reference approach is needed to achieve precise barriers. As is shown in Table 5.1, the barrier for rotating

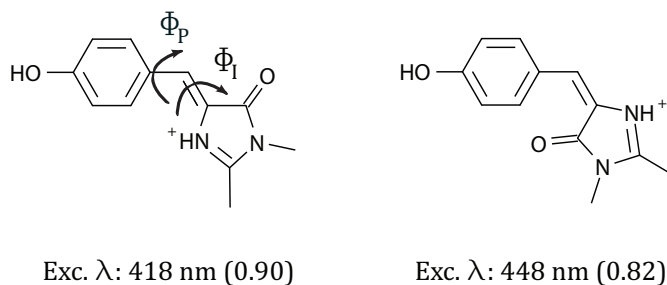


Figure 5.10: The computed excitation wavelengths with corresponding oscillator strengths for the two isomers of *p*HBDI.

	Φ_I	Φ_P
<i>m</i> -HBDI	2.2 eV	0.25 eV
<i>p</i> -HBDI	2.0 eV	0.35 eV

Table 5.1: Computed barrier for rotation around the bonds at the DFT B3LYP 6-311+G(d,p) level of theory. These serve as rough estimates only. For a more precise barrier a multi-reference method needs to be applied.

about the double bond is 2.0 eV for *p*HBDI, while it is only 0.35 eV for the single bond. Thus it may not be feasible to perform the isomerization in the gas phase with an internal energy of roughly 0.3 eV. The question is then whether or not the sample comes in the form of pure *cis* or perhaps both isomeric forms.

With the internal energy of 0.3 eV and the barrier of 0.35 eV for the single bond, the chromophore will span some angles at room temperature. This will of course change the absorption properties, and is most likely to have a broadening effect in the spectra of the individual isomeric forms.

For the *meta*-isomer, the absorption spectrum in the visible range is broader than for *para*. This can be attributed to a combination of effects. First, the absorption for the *cis*- and *trans*-isomers is expected to be shifted for the same reasons as for *p*HBDI, the steric constraint due to the proton. The barrier for *m*HBDI this isomerization is somewhat higher than for *p*HBDI, 2.2 eV as shown in Table 5.1. On top of this effect on the spectral shape of the absorption profile, the rotation about the C–C single bond to the phenolate, results in two different rotamers. The effect on the absorp-

tion properties of this may not be huge, however, with a barrier of 0.25 eV the broadening in the may be pronounced.

In the UV region the spectra are quite different. For *p*HBDI, the fact that no action is seen above 300 nm together with the fact that from 300 nm to 355 nm for *m*HBDI action is visible, can possibly be explained by the lower barrier for rotation for *m*HBDI. Combined with the difference in the rotamers, the lower barriers could be the reason that the absorption apparently does not go to zero in this range. The possibility of finding the *meta*-isomers at larger dihedral angles (resulting in a change of the absorption properties) may be the reason for this. At lower wavelengths, the different absorption profiles are attributed to different energies of the higher-lying excited states of the two different structural isomers.

5.5 Absorption experiments - Anions

5.5.1 Power dependences

Just like for the protonated GFP model chromophores, the number of photons needed to cause dissociation of the anions has been performed. For the *meta*-isomer, *m*HBDI, the dependence of laser-pulse energy was performed at 480 nm and 650 nm. As shown in Fig. 5.11, the experimental results at 650 nm matches a Poisson distribution with $n=2$. Thus, the energy of two photons are needed in order for neutral fragments to be created. However, at 480 nm the energy of one photon seems adequate to create neutral fragments. Common for both wavelengths is that the neutral fragments are only distinguishable in the first channel of the SED following laser interaction. The dissociation thus occurs on a time-scale shorter than $\sim 10 \mu\text{s}$.

For the *para*-isomer, *p*HBDI, the power dependence was performed at a wavelength of 480 nm. This has been studied before, using the MCP detector, with different results, both a one-photon dependence [37] and a two-photon dependence [36]. This time it has been performed using both the SED and the MCP detector. The experimental results together with theoretical fits are displayed in Fig. 5.12. The experimental data from the MCP detector clearly fits better with a Poisson distribution with $n=2$, than with $n=1$, suggesting that the delayed dissociation has a two-photon dependence. The data from the SED are separated into two parts. The neutral fragments created promptly (within the first $\sim 10 \mu\text{s}$), arrive in the first peak after laser interaction on the SED. The power dependence of this

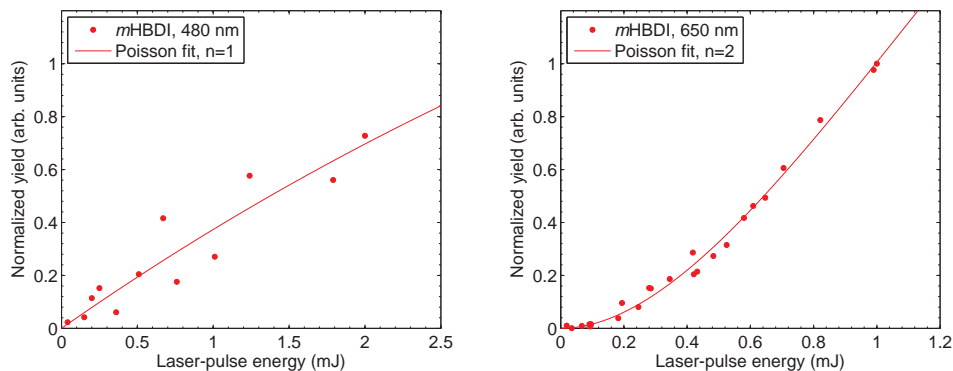


Figure 5.11: The power dependence of deprotonated *m*HBDI performed at 480 nm (left) and 650 nm (right). Only prompt signal was observed. The experimental data at both wavelengths have been fitted to Poisson distributions. At 480 nm the best fit is with $n=1$ and at 650 nm it is best with $n=2$.

peak is performed separately, in order to distinguish between prompt and delayed fragmentation channels. The power dependence for the delayed dissociation on the SED shows, like it was shown with the MCP detector, a clear two-photon dependence. However, the prompt channel shows a one-photon dependence. This can seem somehow counter-intuitive, since dissociation after absorbing one photon normally would be expected to occur slower than after absorption of two. Nonetheless, the experimental results for the prompt channel fits best with a Poisson distribution with $n=1$. The reason for this one-photon dependence as was shown in Sec. 5.2.3 is electron emission.

5.5.2 Action absorption spectra

The experimental data for *p*HBDI is presented in the top part of Fig. 5.13. In the visible region, this figure contains the action spectrum obtained with the MCP detector, which is used to monitor the delayed action, and the spectrum obtained from the prompt action on the SED. The two spectra are clearly different. Both prompt and delayed show the previously observed action absorption maximum at ~ 482 nm, however, while the delayed action has practically vanished below 450 nm, the prompt channel shows clear sign of absorption down to ~ 380 nm. This implies that there is a prompt decay channel for which the decay occurs on a time-scale shorter

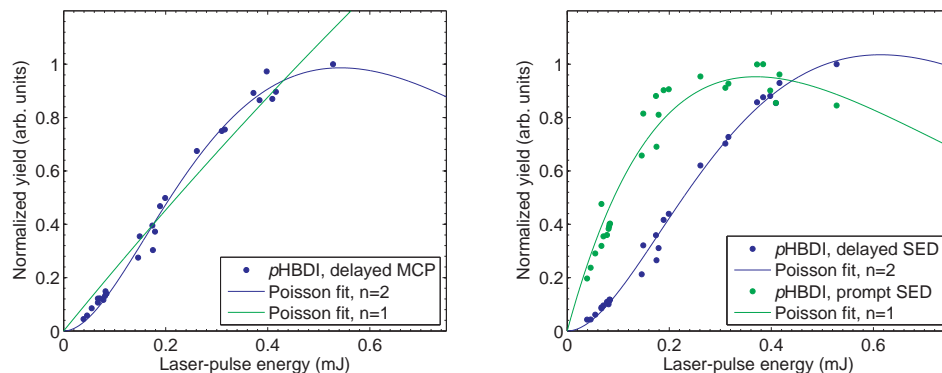


Figure 5.12: The power dependence of deprotonated *p*HBDI performed at 480 nm. The experimental data have been fitted to Poisson distributions. To the left the results from the MCP detector are displayed, to the right the results from the SED. The data match a Poisson distribution with $n=2$ for both the delayed dissociation on SED and the MCP detector, while the prompt action on the SED fit with a $n=1$ Poisson distribution.

than a few μ s. This prompt channel is electron emission, which was the explanation for the one-photon dependence in the prompt channel. This is supported by the spectra measured Forbes *et. al* [97, 99]. They cannot measure the electron directly, but, from the lack of fragment ions, they have inferred the resulting profile for electron detachment. The similarity with the spectra shown in Fig. 5.13 is striking.

The prompt action absorption spectrum for deprotonated *m*HBDI is also presented in the figure. As it shows, the spectra for the *meta*- and *para*-isomers are very different. For *m*HBDI, action is observed in the 420 nm to 500 nm region, similarly to what is seen for *p*HBDI. However, for wavelengths above ~ 520 nm the *para*-isomer does not absorb, whereas the *meta*-isomer does. The action is difficult to observe, due to a combination of a low cross section and the requirement of two photons for action to be seen. In the UV-region both isomers show an absorption maximum somewhat above 300 nm. The relative cross section below and above 355 nm for *p*HBDI should be compared with care, since the spectrum is merged together at this wavelength. The stitching is made harder for *p*HBDI since the cross section is low at this wavelength. For the same reason, the spectrum in the visible and the UV of *m*HBDI should be compared with care since the spectrum is stitched at 420 nm.

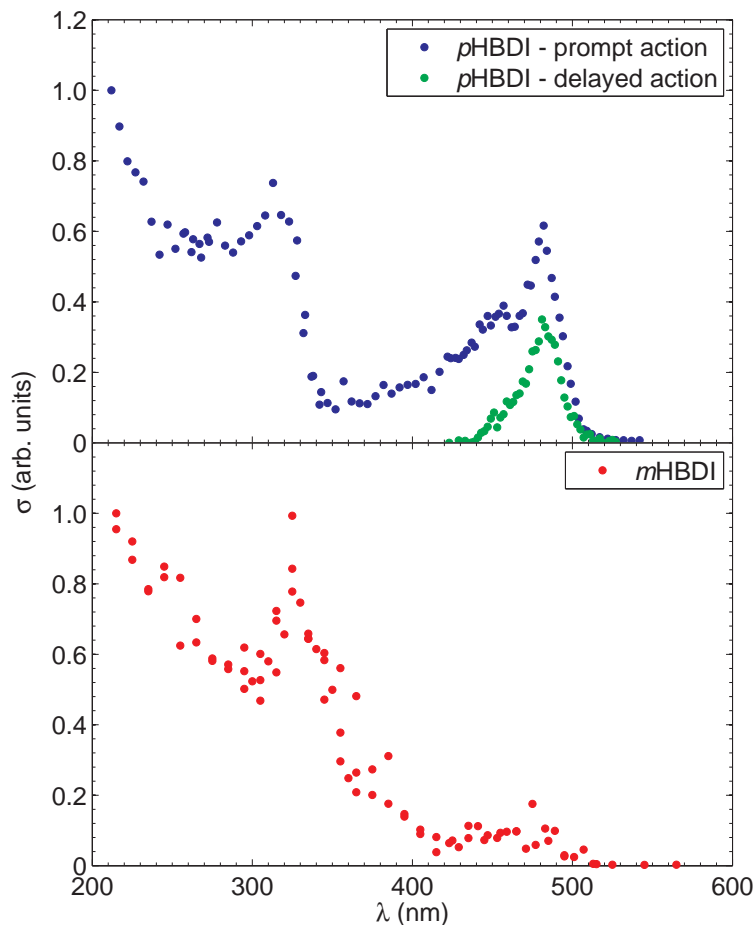


Figure 5.13: Action-absorption spectra of the two deprotonated chromophore samples. The upper graph shows the spectrum for *p*HBDI, the lower displays *m*HBDI.

For *p*HBDI an absorption maximum is observed at 315 nm, while it for *m*HBDI is at 325 nm. At lower wavelengths both isomers show an increase in action towards 210 nm. The observed spectrum for *m*HBDI is in general more scattered than for *p*HBDI. The reason for this is that the *m*HBDI-ions were harder to produce than the *p*HBDI-ions with the ESI process, resulting in lower statistics, which then explains the somewhat more noisy spectrum.

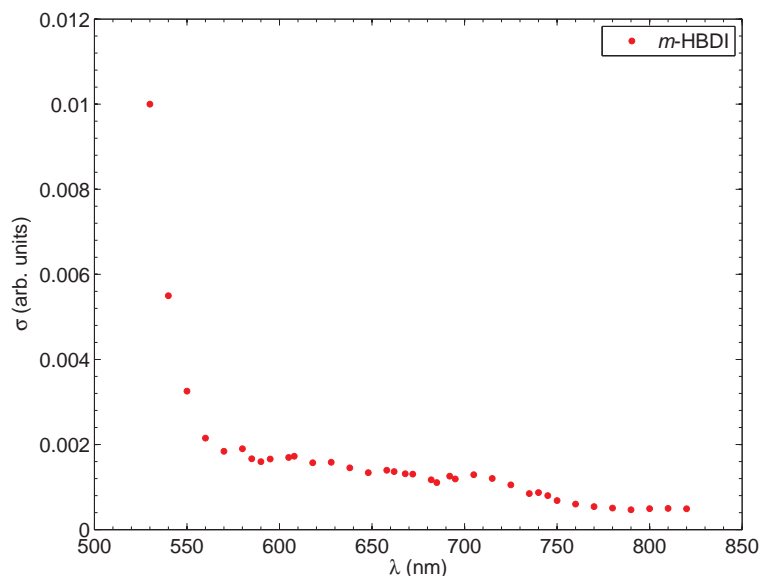


Figure 5.14: High wavelength part of the action-absorption spectra of the *m*HBDI model chromophore.

5.5.3 Discussion

The two action absorption spectra for deprotonated *p*HBDI in the 350 nm to 550 nm region show that the delayed (statistical) dissociation is observable only in the part of the wavelength-range that prompt dissociation is observed. As the power dependences suggest, two photons are required for dissociation in the delayed channels and one photon for prompt action. This suggests that the difference in the action absorption spectra is not because the time-scale of statistical dissociation becomes too fast at lower wavelengths. It is because a competing process is dominant at wavelengths lower than ~ 460 nm. The delayed action is a result of the excited anion leaving the excited S_1 by internal conversion. The movements of the anion on the excited state potential energy surface can lead to a conical intersection where the ground state and the excited state potential energy surfaces cross. In this point a non-adiabatic coupling between electronic energy and nuclear motion facilitates the de-excitation of the electronic energy into nuclear motion (vibrational energy).

This coupling of electronic energy into nuclear energy competes with

the process of electron emission from the excited state. In Sec. 5.2.2 the VDE of deprotonated *p*HBDI is shown to be 2.68 ± 0.1 eV (463 nm). Nevertheless, electrons are emitted at higher wavelengths, similarly to what was found for the model chromophore for the photoactive yellow protein, deprotonated *p*CMe⁻, where electrons are also emitted with photon energies lower than the VDE. Interestingly the explanation for this happening for *p*HBDI appears to be similar. With photon energies below the threshold for electron detachment, energy from nuclear vibrations is needed to emit an electron. At wavelengths above ~ 463 nm the process of electron emission is thus dependent on internal vibrational redistribution for vibrational auto-detachment to occur. This process is like the process of internal conversion also of non-adiabatic nature, although the energy-flow is opposite direction. In the case of electron emission at photon energies below VDE, the energy in nuclear motion has to couple into electronic energy, while in the case of internal conversion, electronic energy is coupled into the energy of nuclear motion.

The delayed action, internal conversion from S_1 to S_0 followed by statistical fragmentation, requires absorption of two photons to happen on the millisecond time-scale as shown in the power dependence. For this action to be observed, means that after absorption of the first photon, the anion leaves the excited state by internal conversion, absorbs a second photon, once again leaves the excited state by internal conversion, and then finally dissociates. This is shown schematically in Fig. 5.15.

That the internal conversion from the excited state occurs in competition with electron emission, signifies that the process leading to the conical intersection point on the excited state potential energy surfaces happens very efficiently. If not, the de-excitation would have occurred earlier by electron emission. This is also the reason that the delayed action vanishes at photon energies above the VDE. With photon energies above VDE, the time required for electron emission is lowered, resulting in a much lower probability of the excited anion to end up in the ground state by internal conversion. This is supported by high level theoretical calculations showing, that above VDE the process of electron emission changes from vibrationally induced electron detachment from the S_1 -state into occurring through electronic resonances in the neutral continuum [94].

The action of deprotonated *p*HBDI becomes less intense for wavelengths going towards 350 nm, however, below this the action absorption spectrum starts to show an increase in action, as shown in Fig. 5.13. This increase in absorption cross section indicates the opening of another resonant ab-

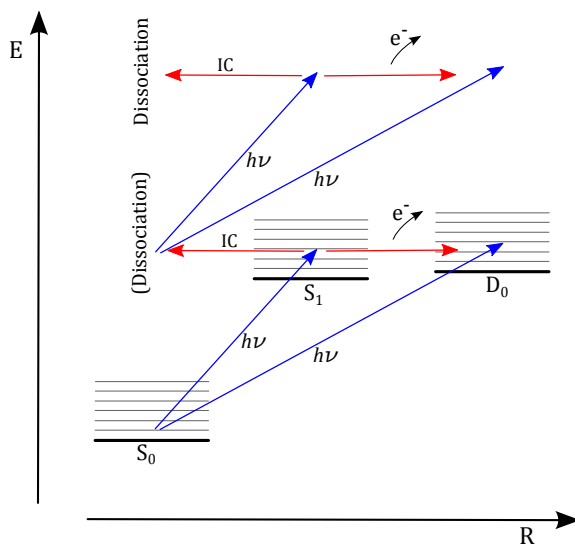


Figure 5.15: The main pathways of the anionic model for the green fluorescent protein chromophore, *p*HBDI. From the ground state, the absorption of a photon can result in either direct detachment or excitation to the S_1 -state. In the excited state, S_1 , de-excitation occurs mainly by internal conversion into S_0 or by electron emission to $D_0 + e^-$. If the anion undergoes internal conversion to the vibrationally hot ground state, S_0 , fragmentation may occur (on a long time-scale) or another photon can be absorbed. Should the anion once again end up in the ground state, then the time-scale for dissociation is much shorter.

sorption channel below 350 nm, similarly to what was shown for *p*CMe⁻. For *p*CMe⁻ the S_2 -state, although lying in the continuum, resulted in an increase in the absorption cross section around 320 nm. For *p*HBDI the maximum appears at 315 nm and according to high level theoretical calculations, this is due to two close-lying excited states in the anion, S_2 and S_3 [102, 103]. Moreover, at around these wavelengths the first excited state in the neutral radical begins to be available as de-excitation channel. At these higher photon energies, electron emission is expected to be the most dominant process, based on the results from the action absorption spectra in the visible region. The second and third excited states of the anion, thus serve as door-way states for electron emission. That is, the resonant nature of these transitions results in a higher probability of electron detachment at a given wavelength in that region, than would be the case if no excited state

in the anion had been present.

When comparing the absorption profile of the deprotonated *p*HBDI with the *meta*-isomer, Fig. 5.13, it appears that the maxima are not too different for the isomers. This is, with the experience from the absorption properties of the PYP model chromophores, somewhat surprising as the photo-physical properties were quite different for the isomers. Although the maxima of the HBDI isomers are similar, the deprotonated *m*HBDI model, shows only very weak absorption in the visible. Moreover, no sign of delayed dissociation was observable at any wavelength. In the 420 nm to 500 nm region, the process is expected to be due to electron emission. According to calculations [102, 103], there is not an excited state in this particular wavelength region, however, the neutral radical ground state is calculated to lie in this region. At the B3LYP 6-311++G(d,p) level of theory, the vertical detachment energy of the *m*HBDI-anion is found to be 2.58 eV (481 nm). This correlates nicely with the observation of an absorption profile in the region from 420 nm to 500 nm with a maximum around \sim 480 nm. The cross section in this wavelength-range is, not surprisingly, quite low. For *p*HBDI, the resonant character of the $S_0 \rightarrow S_1$ transition, serves to increase the probability of observing electrons in this range, whereas for *m*HBDI no such resonant transition is found in the range. Thus, direct detachment is the only emission process. This is supported the energy distribution of electrons emitted from the *meta*-isomer of GFP shown in Fig. 5.16. With higher photon energies, the distribution of energies of the emitted electrons reaches to higher energies. The distributions have some similarity to the one observed for *p*HBDI, however, it is clear that the direct emission process is more prominent for *m*HBDI. The high energy edge of the distributions shifts almost exactly with the difference in photon energy, as would be expected for direct emission.

With this knowledge of direct detachment for *m*HBDI in the 420 nm to 500 nm range, it is interesting to have a glance back at the ELISA action absorption spectrum for *m*CMe⁻. Depending on where the VDE is expected for this model, it should be possible to observe neutral from direct detachment of this model as well. And there is actually also indication of this in the spectrum from \sim 420 nm and down. The calculated VDE is 448 nm (2.77 eV) at the B3LYP 6-311++G(d,p) level, which is not too far from where a small increase in the action absorption spectrum.

The absorption profile in the UV region of deprotonated *m*HBDI, shows maximum at 325 nm with a shoulder around 380 nm. This is due to higher lying states in the anion. The first excited state S_1 lies in the red part of

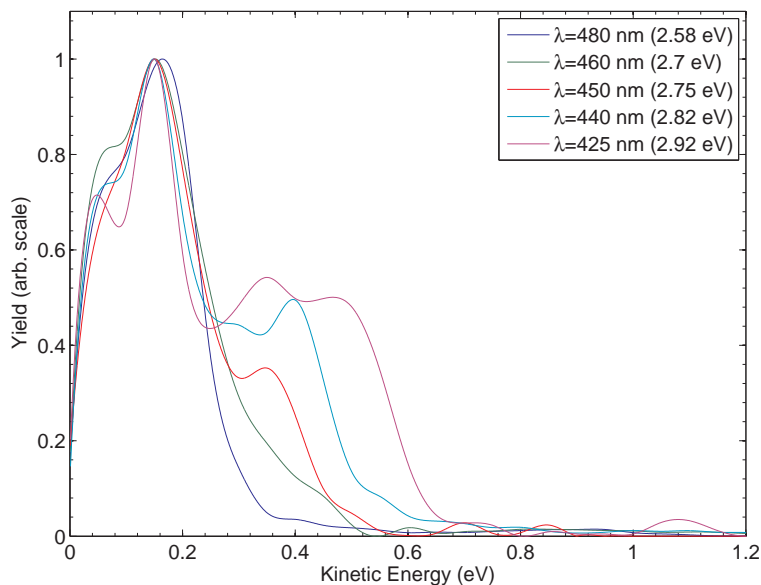


Figure 5.16: The electron energy distribution observed for *m*HBDI.

the visible spectrum, as discussed below. Thus the absorption profile in the UV region is due to excited states lying in the continuum of the neutral radical. These higher lying states, also act as doorway-states for electron emission for these anionic chromophores.

The chromophore models for PYP and GFP show some common tendencies in the absorption properties. The *para*-isomers show absorption in the blue part of the visible spectrum, and have a VDE slightly above this in energy. For the *meta*-isomers the first transition energy is lowered, however, on the cost of oscillator strength. For *mCMe*⁻ this was shown to be due to a lower degree of coupling between the two sub-systems making up the chromophore. The explanation for the changes in absorption properties for *m*HBDI compared to *p*HBDI is the same. Similarly to the *m*- and *pCMe*⁻ chromophores, the *meta*-substitution for HBDI results in a lowering of the electronic conjugation and de-localization. This was visualized by the lack of the possibility of drawing the valence resonance structures for *m*HBDI. It is also clear from the highest occupied molecular orbitals for the HBDI models. These are shown in Fig. 5.17. It is evident that the degree of electronic de-localization is much higher for *p*HBDI.

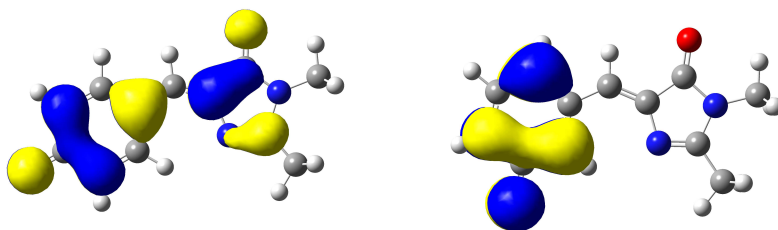


Figure 5.17: The HOMO orbitals of *p*HBDI (left) and *m*HBDI (right). The degree of electronic de-localization is much more pronounced for the *para*-isomer.

5.6 Conclusion

The experiments performed for the two structural isomers, *p*HBDI and *m*HBDI, have shown that the photo-physical properties are quite different for the two, especially in the deprotonated form. The decoupling between the two sub-systems was like for the PYP model chromophores pronounced for the *meta*-isomer, resulting in a redshift of the transition to the first excited state compared to the *para*-isomer. This redshifted transition has a higher degree of charge transfer and thus a lower oscillator strength. For this reason it was quite hard to observe in the absorption spectrum. For *p*HBDI the absorption profile from the prompt channel was shown to contain much more information than the delayed channel. This is due to the possibility of detaching an electron.

This electron detachment channel was examined closer by monitoring the distribution of electron kinetic energies at several wavelengths. From the results at 355 nm it was found that the vertical detachment energy is 2.68 ± 0.1 eV. Moreover, from the spectra in the visible region it was concluded that the process of electron emission in the wavelength region, where the $S_0 \rightarrow S_1$ transition is probable, is primarily from electron emitted from the excited state. With photon-energies lower than the VDE it is still possible to emit photons, however then the lacking energy is taken from the nuclei motion.

For the protonated forms of *p*HBDI and *m*HBDI, the absorption spectrum was the broadest for *m*HBDI. This was attributed to the lower rotational barrier about the C–C single bond in the bridging region combined with the two different rotamers obtained by this rotation and the possible presence of both isomeric forms. For *p*HBDI the two close-lying maxima

was attributed to the *cis* and *trans* forms respectively.

CHAPTER 6

Conclusion and outlook

The experiments presented in this work have focused on the photo-physical properties of the chromophores from the green fluorescent protein and the photoactive yellow protein. This has been studied by experimenting on different structural isomers, more specifically, having the OH-group on the phenol in different positions. The properties has been investigated by performing gas phase action absorption spectroscopy and photo-electron spectroscopy on the models. In the action absorption experiments performed at ELISA, the use of the glass plate detector made it possible to distinguish between prompt and delayed (statistical) action. Without this detector, it would not have been possible to measure the spectra in the UV region for the anionic models, moreover, the additional information gained on the prompt dynamics in the visible region of the *p*HBDI-anion would not have been recorded. The changes made to the photo-electron setup allowed the detection of low energy electrons. As the results have shown, the conclusions drawn without the possibility to measure electrons emitted with low energy would not have been lacking lot of interesting information.

The absorption spectrum for the protonated form of the *p*HBDI chromophore had been measured previously, however, not in the UV region. The spectrum of the cationic *para*-isomer showed two close-lying peaks, attributed to *cis*- and *trans*-forms, in the visible range, while only one was found in a previous experiment. The reason for this apparent discrepancy is most likely due to the laser system used for the previous experiments, with which the peaks could not be resolved. For the cationic *m*HBDI-isomer, the spectrum in the visible range was found to be broader than

for *p*HBDI-isomer. This was explained by a lower rotational barrier for the rotation about the C–C single bond in the bridging region for the *meta*-isomer. Such a rotation, or most likely just the possibility to find the chromophore at wider range of angles, might explain the broader absorption profile for *m*HBDI.

The results for the anionic models were in many aspects shown to be quite similar for both chromophores models for GFP and PYP. It was shown that the absorption properties depend crucially on the electronic coupling between the two sub-units making up the chromophores. For the *meta*-isomers, where the coupling is low, the result is a shift of the transition energies. The transition to the first excited state becomes of charge-transfer character, is redshifted and has a much lower oscillator strength. The transitions with higher oscillator strength are more localized on the separate sub-systems, which results in a blueshift of the transition energy compared to the more coupled systems, *para* and *ortho*.

The photo-electron experiments for the *para*-isomer models from the proteins has shown, that in the wavelength region around the $S_0 \rightarrow S_1$ transition the energy-distribution of the electrons does not change a lot. This is explained by the process of electron emission. In the region where the transition to the first excited state is possible, the electrons are primarily emitted from this excited state, that is $S_1 \rightarrow D_0 + e^-$. Moreover, the results have shown that electrons can be emitted with photon-energies somewhat lower than the vertical detachment energies by the process of internal vibrational redistribution followed vibrational auto-detachment.

From the photo-electron spectra at lower wavelengths, where the transition to S_1 did not disturb the picture, the vertical detachment energy could be determined. For *p*CMe⁻ the VDE is determined to be 2.88 ± 0.1 eV while the value for *p*HBDI is 2.68 ± 0.1 eV. Both of these thresholds lie above the transition to the first excited state. The fact that these two different chromophore systems are so much alike in terms of the relative positions of the vertical excitation energy and the vertical detachment energy makes you wonder if this could be a common feature for anionic chromophore systems or is it just mere coincidence.

For *p*CMe⁻ the electron kinetic energy was also measured at a wavelength where another excited state in the anion comes to play. The result of this is an increase in the probability of electron detachment, owing to the higher oscillator strength of the transition to the anionic excited state. Thus excited states lying in the continuum of the neutral radical serve as doorway states for electron emission.

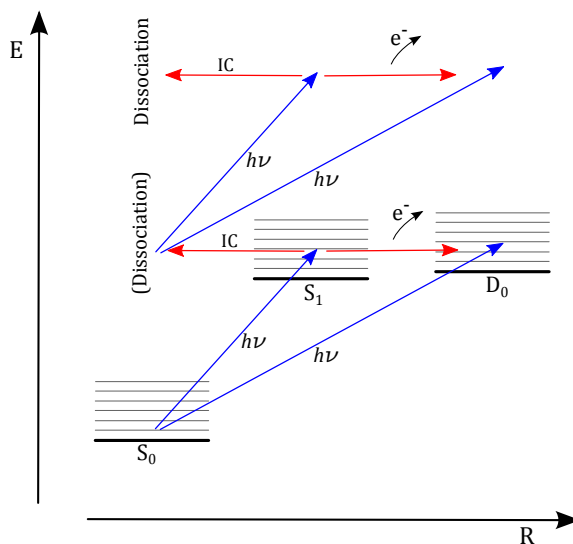


Figure 6.1: The main pathways of the anionic model for the green fluorescent protein chromophore, *p*HBDI. In the excited state, S_1 , de-excitation occur mainly by internal conversion into S_0 or by electron emission to $D_0 + e^-$.

The combined results of the photo-electron experiments and the action absorption spectroscopy together with high level theoretical calculations have shown that in the first excited state of the *p*HBDI anion there are two main de-excitation channels, both of which are of non-adiabatic nature. The first is internal conversion, where electronic energy is coupled into vibrational energy of the nuclei core, while the second is coupling vibrational energy from the nuclear motion into electronic energy, whereby electron emission is facilitated. These pathways are shown in Fig. 6.1. The results show that for photon energies below the VDE, the coupling by internal conversion is the fastest, while the picture changes for photon energies above. These bits of information about the processes occurring when energy is absorbed by systems are important not only for the small community working with these chromophores. And thinking bigger: in a world where the the focus on energy production and consumption is rapidly increasing, the understanding of how energy flows in very small systems may be the key towards more efficient systems on larger scale, both in terms of increased production and lower consumption.

Although the results presented in this work gives new insight in the

photo-physical properties of the chromophores from GFP and PYP, there is still much to be studied. For the model of the green fluorescent protein it would be very interesting to study the dynamics in the first excited state of the anion by means of femtosecond pump-probe spectroscopy. This might shed light on the time-scales for internal conversion and electron emission and the competition between the two processes.

For the photoactive yellow protein it would be interesting to study the distribution of electron kinetic energies of the $mCMe^-$ model. This would show if the small increase in the action absorption spectrum at ~ 420 nm is really due to the opening of the direct electron detachment channel.

Another interesting experiment, would be to study the effect on the absorption spectrum of the temperature of the gas phase ions. This can be studied by cooling the trap in the ESI-source and have been done for a retinal model chromophore. Similarly it is possible to perform photo-electron spectroscopy on cold ions. Such experiments may give insight in the ground state dynamics of the chromophores, and the importance of vibrational energy for electron emission from the first excited state.

References

- [1] R. Heim, D. C. Prasher, and R. Y. Tsien, *Wavelength mutations and posttranslational autoxidation of green fluorescent protein*, Proceedings of the National Academy of Sciences of the United States of America **91**, 12501 (1994).
- [2] R. Y. Tsien, *The green fluorescent protein*, Annual Review of Biochemistry **67**, 509 (1998).
- [3] M. V. Matz, A. F. Fradkov, Y. A. Labas, A. P. Savitsky, A. G. Zaraisky, M. L. Markelov, and S. A. Lukyanov, *Fluorescent proteins from nonbioluminescent Anthozoa species*, Nature Biotechnology **17**, 969 (1999).
- [4] R. Brudler, T. E. Meyer, U. K. Genick, S. Devanathan, T. T. Woo, D. P. Millar, K. Gerwert, M. A. Cusanovich, G. Tollin, and E. D. Getzoff, *Coupling of hydrogen bonding to chromophore conformation and function in photoactive yellow protein*, Biochemistry **39**, 13478 (2000).
- [5] T. E. Meyer, S. Devanathan, T. Woo, E. D. Getzoff, G. Tollin, and M. A. Cusanovich, *Site-specific mutations provide new insights into the origin of pH effects and alternative spectral forms in the photoactive yellow protein from Halorhodospira halophila*, Biochemistry **42**, 3319 (2003).
- [6] N. C. Shaner, G. H. Patterson, and M. W. Davidson, *Advances in fluorescent protein technology*, Journal of Cell Science **120**, 4247 (2007).
- [7] A. F. Philip, K. T. Eisenman, G. A. Papadantonakis, and W. D. Hoff, *Functional tuning of photoactive yellow protein by active site residue 46*, Biochemistry **47**, 13800 (2008).
- [8] H. Niwa, S. Inouye, T. Hirano, T. Matsuno, S. Kojima, M. Kubota, M. Ohashi, and F. I. Tsuji, *Chemical nature of the light emitter of the Ae-*

- quorea green fluorescent protein*, Proceedings of the National Academy of Sciences of the United States of America **93**, 13617 (1996).
- [9] P. Changenet-Barret, A. Espagne, N. Katsonis, S. Charier, J. B. Baudin, L. Jullien, P. Plaza, and M. M. Martin, *Excited-state relaxation dynamics of a PYP chromophore model in solution: Influence of the thioester group*, Chemical Physics Letters **365**, 285 (2002).
- [10] D. S. Larsen, M. Vengris, I. H. M. van Stokkum, M. A. van der Horst, F. L. De Weerd, K. J. Hellingwerf, and R. van Grondelle, *Photoisomerization and Photoionization of the Photoactive Yellow Protein Chromophore in Solution*, Biophysical Journal **86**, 2538 (2004).
- [11] D. S. Larsen and R. van Grondelle, *Initial photoinduced dynamics of the photoactive yellow protein*, ChemPhysChem **6**, 828 (2005).
- [12] J. Dong, K. M. Solntsev, and L. M. Tolbert, *Solvatochromism of the green fluorescence protein chromophore and its derivatives*, Journal of the American Chemical Society **128**, 12038 (2006).
- [13] A. Espagne, D. H. Paik, P. Changenet-Barret, M. M. Martin, and A. H. Zewail, *Ultrafast photoisomerization of photoactive yellow protein chromophore analogues in solution: Influence of the protonation state*, ChemPhysChem **7**, 1717 (2006).
- [14] K. M. Solntsev, O. Poizat, J. Dong, J. Rehaut, Y. Lou, C. Burda, and L. M. Tolbert, *Meta and para effects in the ultrafast excited-state dynamics of the green fluorescent protein chromophores*, Journal of Physical Chemistry B **112**, 2700 (2008).
- [15] A. Sergi, M. Grüning, M. Ferrario, and F. Buda, *Density Functional Study of the Photoactive Yellow Protein's Chromophore*, The Journal of Physical Chemistry B **105**, 4386 (2001).
- [16] M. A. L. Marques, X. López, D. Varsano, A. Castro, and A. Rubio, *Time-dependent density-functional approach for biological chromophores: The case of the green fluorescent protein*, Physical Review Letters **90**, 2581011 (2003).
- [17] T. Laino, R. Nifosì, and V. Tozzini, *Relationship between structure and optical properties in green fluorescent proteins: A quantum mechanical study of the chromophore environment*, Chemical Physics **298**, 17 (2004).

- [18] E. V. Gromov, I. Burghardt, J. T. Hynes, H. Koeppe, and L. S. Cederbaum, *Electronic structure of the photoactive yellow protein chromophore: Ab initio study of the low-lying excited singlet states*, *Journal of Photochemistry and Photobiology A: Chemistry* **190**, 241 (2007).
- [19] E. V. Gromov, I. Burghardt, H. Koeppe, and L. S. Cederbaum, *Electronic structure of the PYP chromophore in its native protein environment*, *Journal of the American Chemical Society* **129**, 6798 (2007).
- [20] L. H. Andersen and A. V. Bochenkova, *The photophysics of isolated protein chromophores*, *European Physical Journal D* **51**, 5 (2009).
- [21] D. Zuev, K. B. Bravaya, T. D. Crawford, R. Lindh, and A. I. Krylov, *Electronic structure of the two isomers of the anionic form of p-coumaric acid chromophore*, *Journal of Chemical Physics* **134**, 034310 (2011).
- [22] F. O. Talbot, T. Tabarin, R. Antoine, M. Broyer, and P. Dugourd, *Photodissociation spectroscopy of trapped protonated tryptophan*, *Journal of Chemical Physics* **122** (2005).
- [23] Q. Bian, M. W. Forbes, F. O. Talbot, and R. A. Jockusch, *Gas-phase fluorescence excitation and emission spectroscopy of mass-selected trapped molecular ions*, *Physical Chemistry Chemical Physics* **12**, 2590 (2010).
- [24] J. C. Marcum, A. Halevi, and J. M. Weber, *Photodamage to isolated mononucleotides-photodissociation spectra and fragment channels*, *Physical Chemistry Chemical Physics* **11**, 1740 (2009).
- [25] N. C. Polfer, J. Oomens, D. T. Moore, G. von Helden, G. Meijer, and R. C. Dunbar, *Infrared Spectroscopy of Phenylalanine Ag(I) and Zn(II) Complexes in the Gas Phase*, *Journal of the American Chemical Society* **128**, 517 (2006).
- [26] T. R. Rizzo, J. A. Stearns, and O. V. Boyarkin, *Spectroscopic studies of cold, gas-phase biomolecular ions*, *International Reviews in Physical Chemistry* **28**, 481 (2009).
- [27] S. Smolarek, A. Vdovin, D. L. Perrier, J. P. Smit, M. Drabbels, and W. J. Buma, *High-resolution excitation and absorption spectroscopy of gas-phase p-coumaric acid: Unveiling an elusive chromophore*, *Journal of the American Chemical Society* **132**, 6315 (2010).

- [28] S. Smolarek, A. Vdovin, E. M. M. Tan, M. De Groot, and W. J. Buma, *Spectroscopy and dynamics of methyl-4-hydroxycinnamate: The influence of isotopic substitution and water complexation*, *Physical Chemistry Chemical Physics* **13**, 4393 (2011).
- [29] I. R. Lee, W. Lee, and A. H. Zewail, *Primary steps of the photoactive yellow protein: Isolated chromophore dynamics and protein directed function*, *Proceedings of the National Academy of Sciences of the United States of America* **103**, 258 (2006).
- [30] C. R. S. Mooney, M. Eugenia Sanz, A. R. McKay, R. J. Fitzmaurice, A. E. Aliev, S. Caddick, and H. H. Fielding, *Photodetachment Spectra of Deprotonated Fluorescent Protein Chromophore Anions*, *Journal of the American Chemical Society* (2012).
- [31] D. A. Horke and J. R. R. Verlet, *Photoelectron spectroscopy of the model GFP chromophore anion*, *Physical Chemistry Chemical Physics* **14**, 8511 (2012).
- [32] J. B. Fenn, M. Mann, C. K. Meng, S. F. Wong, and C. M. Whitehouse, *Electrospray Ionization for Mass-Spectrometry of Large Biomolecules*, *Science* **246**, 64 (1989).
- [33] P. Kebarle and L. Tang, *From ions in solution to ions in the gas phase - the mechanism of electrospray mass spectrometry*, *Analytical Chemistry* **65**, 972A (1993).
- [34] S. P. Møller, *ELISA, an electrostatic storage ring for atomic physics*, *Nuclear Instruments and Methods in Physics Research Section A: Accelerators, Spectrometers, Detectors and Associated Equipment* **394**, 281 (1997).
- [35] S. P. Møller and U. V. Pedersen, *Small electrostatic storage rings; also for highly charged ions?*, *Physica Scripta* **T92**, 105 (2001).
- [36] L. H. Andersen, A. Lapierre, S. B. Nielsen, I. B. Nielsen, S. U. Pedersen, U. V. Pedersen, and S. Tomita, *Chromophores of the green fluorescent protein studied in the gas phase*, *European Physical Journal D* **20**, 597 (2002).
- [37] L. H. Andersen, H. Bluhme, S. Boye, T. J. D. Jørgensen, H. Krogh, I. B. Nielsen, S. B. Nielsen, and A. Svendsen, *Experimental studies of*

- the photophysics of gas-phase fluorescent protein chromophores*, Physical Chemistry Chemical Physics **6**, 2617 (2004).
- [38] H. B. Pedersen, M. J. Jensen, C. P. Safvan, X. Urbain, and L. H. Andersen, *Fast beam photofragment apparatus for studies of electronic and nuclear dynamics*, Review of Scientific Instruments **70**, 3289 (1999).
- [39] Y. Toker, D. B. Rahbek, B. Klærke, A. V. Bochenkova, and L. H. Andersen, *Direct and indirect electron emission from the green fluorescent protein chromophore*, Submitted to Physical Review Letters (2012).
- [40] *Simion V8.0*.
- [41] A. Svendsen, *Electron- and photon-induced fragmentation of molecular ions*, Ph.D. thesis, Department of Physics and Astronomy, Aarhus University (2006).
- [42] M. J. Frisch, G. W. Trucks, H. B. Schlegel et al., *Gaussian 03*, Gaussian, Inc., Wallingford, CT, 2004.
- [43] M. J. Frisch, G. W. Trucks, H. B. Schlegel et al., *Gaussian 09*, Gaussian, Inc., Wallingford, CT, 2009.
- [44] P. Hohenberg and W. Kohn, *Inhomogeneous Electron Gas*, Physical Review B **136**, 864 (1964).
- [45] W. Kohn and L. J. Sham, *Self-Consistent Equations Including Exchange and Correlation Effects*, Physical Review **140**, 1133 (1965).
- [46] C. Lee, W. Yang, and R. G. Parr, *Development of the Colle-Salvetti correlation-energy formula into a functional of the electron density*, Physical Review B **37**, 785 (1988).
- [47] A. D. Becke, *Density-functional thermochemistry. III. The role of exact exchange*, The Journal of Chemical Physics **98**, 5648 (1993).
- [48] A. D. Becke, *Density-functional exchange-energy approximation with correct asymptotic behavior*, Physical Review A **38**, 3098 (1988).
- [49] E. Runge and E. K. U. Gross, *Density-functional theory for time-dependent systems*, Physical Review Letters **52**, 997 (1984).

- [50] K. Burke, J. Werschnik, and E. K. U. Gross, *Time-dependent density functional theory: Past, present, and future*, *Journal of Chemical Physics* **123**, 1 (2005).
- [51] J. B. Foresman and A. Frisch, *Exploring Chemistry with Electronic Structure Methods*, second edition.
- [52] T. E. Meyer, *Isolation and characterization of soluble cytochromes, ferredoxins and other chromophoric proteins from the halophilic phototrophic bacterium Ectothiorhodospira halophila*, *BBA - Bioenergetics* **806**, 175 (1985).
- [53] W. W. Sprenger, W. D. Hoff, J. P. Armitage, and K. J. Hellingwerf, *The Eubacterium Ectothiorhodospira halophila Is Negatively Phototactic, with a Wavelength Dependence That Fits the Absorption Spectrum of the Photoactive Yellow Protein*, *Journal of Bacteriology* **175**, 3096 (1993).
- [54] P. D. Coureux, Z. P. Fan, V. Stojanoff, and U. K. Genick, *Picometer-Scale Conformational Heterogeneity Separates Functional from Nonfunctional States of a Photoreceptor Protein*, *Structure* **16**, 863 (2008).
- [55] U. K. Genick, S. M. Soltis, P. Kuhn, I. L. Canestrelli, and E. D. Getzoff, *Structure at 0.85 Å resolution of an early protein photocycle intermediate*, *Nature* **392**, 206 (1998).
- [56] P. Changenet-Barret, P. Plaza, M. M. Martin, H. Chosrowjan, S. Taniguchi, N. Mataga, Y. Imamoto, and M. Kataoka, *Structural Effects on the Ultrafast Photoisomerization of Photoactive Yellow Protein. Transient Absorption Spectroscopy of Two Point Mutants*, *Journal of Physical Chemistry C* **113**, 11605 (2009).
- [57] P. Changenet-Barret, A. Espagne, P. Plaza, K. J. Hellingwerf, and M. M. Martin, *Investigations of the primary events in a bacterial photoreceptor for photomotility: photoactive yellow protein (PYP)*, *New Journal of Chemistry* **29**, 527 (2005).
- [58] M. Baca, G. E. O. Borgstahl, M. Boissinot, P. M. burke, D. R. Williams, K. A. Slater, and E. D. Getzoff, *Complete Chemical Structure of Photoactive Yellow Protein: Novel Thioester-Linked 4-Hydroxycinnamyl Chromophore and Photocycle Chemistry*, *Biochemistry* **33**, 14369 (1994).

- [59] T. E. Meyer, E. Yakali, M. A. Cusanovich, and G. Tollin, *Properties of a water-soluble, yellow protein isolated from a halophilic phototrophic bacterium that has photochemical activity analogous to sensory rhodopsin*, *Biochemistry* **26**, 418 (1987).
- [60] W. D. Hoff, I. H. M. van Stokkum, H. J. van Ramesdonk, M. E. van Brederode, A. M. Brouwer, J. C. Fitch, T. E. Meyer, R. van Grondelle, and K. J. Hellingwerf, *Measurement and global analysis of the absorbance changes in the photocycle of the photoactive yellow protein from *Ectothiorhodospira halophila**, *Biophysical Journal* **67**, 1691 (1994).
- [61] R. Kort, H. Vonk, X. Xu, W. D. Hoff, W. Crielaard, and K. J. Hellingwerf, *Evidence for trans-cis isomerization of the p-coumaric acid chromophore as the photochemical basis of the photocycle of photoactive yellow protein*, *FEBS Letters* **382**, 73 (1996).
- [62] A. Xie, W. D. Hoff, A. R. Kroon, and K. J. Hellingwerf, *Glu46 donates a proton to the 4-hydroxycinnamate anion chromophore during the photocycle of photoactive yellow protein*, *Biochemistry* **35**, 14671 (1996).
- [63] J. Vreede, W. Crielaard, K. J. Hellingwerf, and P. G. Bolhuis, *Predicting the signaling state of photoactive yellow protein*, *Biophysical Journal* **88**, 3525 (2005).
- [64] T. E. Meyer, G. Tollin, J. H. Hazzard, and M. A. Cusanovich, *Photoactive yellow protein from the purple phototrophic bacterium, *Ectothiorhodospira halophila*. Quantum yield of photobleaching and effects of temperature, alcohols, glycerol, and sucrose on kinetics of photobleaching and recovery.*, *Biophysical Journal* **56**, 559 (1989).
- [65] G. Rubinstenn, G. W. Vuister, F. A. A. Mulder, P. E. Düx, R. Boelens, K. J. Hellingwerf, and R. Kaptein, *Structural and dynamic changes of photoactive yellow protein during its photocycle in solution*, *Nature Structural Biology* **5**, 568 (1998).
- [66] K. J. Hellingwerf, J. Hendriks, and T. Gensch, *Photoactive Yellow Protein, a new type of photoreceptor protein: Will this "yellow lab" bring us where we want to go?*, *Journal of Physical Chemistry A* **107**, 1082 (2003).
- [67] D. Zuev, K. B. Bravaya, M. V. Makarova, and A. I. Krylov, *Effect of microhydration on the electronic structure of the chromophores of the photoac-*

- tive yellow and green fluorescent proteins*, *Journal of Chemical Physics* **135** (2011).
- [68] T. Rocha-Rinza, O. Christiansen, D. B. Rahbek, B. Klærke, L. H. Andersen, K. Lincke, and M. B. Nielsen, *Spectroscopic Implications of the Electron Donor-Acceptor Effect in the Photoactive Yellow Protein Chromophore*, *Chemistry: A European Journal* **16**, 11977 (2010).
- [69] T. Rocha-Rinza, O. Christiansen, J. Rajput, A. Gopalan, D. B. Rahbek, L. H. Andersen, A. V. Bochenkova, A. A. Granovsky, K. B. Bravaya, A. V. Nemukhin, K. L. Christiansen, and M. B. Nielsen, *Gas Phase Absorption Studies of Photoactive Yellow Protein Chromophore Derivatives*, *Journal of Physical Chemistry A* **113**, 9442 (2009).
- [70] M.-B. S. Kirketerp, *Photophysical properties of pi-conjugated molecular ions in the gas phase*, Ph.D. thesis, Department of Physics and Astronomy, Aarhus University (2011).
- [71] O. Shimomura, F. H. Johnson, and Y. Saigi, *Extraction, purification and properties of aequorin, a bioluminescent protein from the luminous hydromedusan, Aequorea*, *Journal of Cellular and Comparative Physiology* **59**, 223 (1962).
- [72] C. W. Cody, D. C. Prasher, W. M. Westler, F. G. Prendergast, and W. W. Ward, *Chemical structure of the hexapeptide chromophore of the aequorea green-fluorescent protein*, *Biochemistry* **32**, 1212 (1993).
- [73] M. Chalfie, Y. Tu, G. Euskirchen, W. W. Ward, and D. C. Prasher, *Green Fluorescent Protein as a Marker for Gene-Expression*, *Science* **263**, 802 (1994).
- [74] R. M. Hoffman, *The multiple uses of fluorescent proteins to visualize cancer in vivo*, *Nature Reviews Cancer* **5**, 796 (2005).
- [75] K. Stoletov, V. Montel, R. D. Lester, S. L. Gonias, and R. Klemke, *High-resolution imaging of the dynamic tumor cell-vascular interface in transparent zebrafish*, *Proceedings of the National Academy of Sciences of the United States of America* **104**, 17406 (2007).
- [76] K. I. Willig, R. R. Kellner, R. Medda, B. Hein, S. Jakobs, and S. W. Hell, *Nanoscale resolution in GFP-based microscopy*, *Nature Methods* **3**, 721 (2006).

- [77] A. Chiocchetti, E. Tolosano, E. Hirsch, L. Silengo, and F. Altruda, *Green fluorescent protein as a reporter of gene expression in transgenic mice*, *Biochimica et Biophysica Acta - Gene Structure and Expression* **1352**, 193 (1997).
- [78] <http://www.glofish.com> (2012).
- [79] M. Ormö, A. B. Cubitt, K. Kallio, L. A. Gross, R. Y. Tsien, and S. J. Remington, *Crystal structure of the Aequorea victoria green fluorescent protein*, *Science* **273**, 1392 (1996).
- [80] <http://nobelprize.org> (2008).
- [81] O. Shimomura, *Structure of the chromophore of Aequorea green fluorescent protein*, *FEBS Letters* **104**, 220 (1979).
- [82] A. B. Cubitt, R. Heim, S. R. Adams, A. E. Boyd, L. A. Gross, and R. Y. Tsien, *Understanding, improving and using green fluorescent proteins*, *Trends in Biochemical Sciences* **20**, 448 (1995).
- [83] T. D. Craggs, *Green fluorescent protein: Structure, folding and chromophore maturation*, *Chemical Society Reviews* **38**, 2865 (2009).
- [84] R. Heim and R. Y. Tsien, *Engineering green fluorescent protein for improved brightness, longer wavelengths and fluorescence resonance energy transfer*, *Current Biology* **6**, 178 (1996).
- [85] S. R. Meech, *Excited state reactions in fluorescent proteins*, *Chemical Society Reviews* **38**, 2922 (2009).
- [86] M. Chattoraj, B. A. King, G. U. Bublitz, and S. G. Boxer, *Ultra-fast excited state dynamics in green fluorescent protein: Multiple states and proton transfer*, *Proceedings of the National Academy of Sciences of the United States of America* **93**, 8362 (1996).
- [87] S. Olsen and S. C. Smith, *Bond selection in the photoisomerization reaction of anionic green fluorescent protein and kindling fluorescent protein chromophore models*, *Journal of the American Chemical Society* **130**, 8677 (2008).
- [88] I. V. Polyakov, B. L. Grigorenko, E. M. Epifanovsky, A. I. Krylov, and A. V. Nemukhin, *Potential Energy Landscape of the Electronic States of*

- the GFP Chromophore in Different Protonation Forms: Electronic Transition Energies and Conical Intersections*, *Journal of Chemical Theory and Computation* **6**, 2377 (2010).
- [89] S. Wan, S. Liu, G. Zhao, M. Chen, K. Han, and M. Sun, *Photoabsorption of green and red fluorescent protein chromophore anions in vacuo*, *Biophysical Chemistry* **129**, 218 (2007).
- [90] K. Bravaya, A. Bochenkova, A. Granovskii, and A. Nemukhin, *Modeling of the structure and electronic spectra of green fluorescent protein chromophore*, *Russian Journal of Physical Chemistry B, Focus on Physics* **2**, 671 (2008).
- [91] E. Epifanovsky, I. Polyakov, B. Grigorenko, A. Nemukhin, and A. I. Krylov, *Quantum chemical benchmark studies of the electronic properties of the green fluorescent protein chromophore. 1. Electronically excited and ionized states of the anionic chromophore in the gas phase*, *Journal of Chemical Theory and Computation* **5**, 1895 (2009).
- [92] E. Epifanovsky, I. Polyakov, B. Grigorenko, A. Nemukhin, and A. I. Krylov, *The effect of oxidation on the electronic structure of the green fluorescent protein chromophore*, *Journal of Chemical Physics* **132** (2010).
- [93] K. B. Bravaya, M. G. Khrenova, B. L. Grigorenko, A. V. Nemukhin, and A. I. Krylov, *Effect of protein environment on electronically excited and ionized states of the green fluorescent protein chromophore*, *Journal of Physical Chemistry B* **115**, 8296 (2011).
- [94] A. V. Bochenkova, J. Rajput, D. B. Rahbek, B. Klærke, and L. H. Andersen, *Nuclei versus electrons: a striking ultrafast dual photoresponse of biochromophores prompted by nature*, Submitted to *Nature Chemistry* (2012).
- [95] A. M. Bogdanov, A. S. Mishin, I. V. Yampolsky, V. V. Belousov, D. M. Chudakov, F. V. Subach, V. V. Verkhusha, S. Lukyanov, and K. A. Lukyanov, *Green fluorescent proteins are light-induced electron donors*, *Nature Chemical Biology* **5**, 459 (2009).
- [96] S. B. Nielsen, A. Lapierre, J. U. Andersen, U. V. Pedersen, S. Tomita, and L. H. Andersen, *Absorption spectrum of the green fluorescent protein chromophore anion in vacuo*, *Physical Review Letters* **87** (2001).

- [97] M. W. Forbes and R. A. Jockusch, *Deactivation Pathways of an Isolated Green Fluorescent Protein Model Chromophore Studied by Electronic Action Spectroscopy*, *Journal of the American Chemical Society* **131**, 17038 (2009).
- [98] K. Lincke, T. Sølling, L. H. Andersen, B. Klærke, D. B. Rahbek, J. Rajput, C. B. Oehlenschläger, M. A. Petersen, and M. B. Nielsen, *On the absorption of the phenolate chromophore in the green fluorescent protein-role of individual interactions*, *Chemical Communications* **46**, 734 (2010).
- [99] M. W. Forbes, A. M. Nagy, and R. A. Jockusch, *Photofragmentation of and electron photodetachment from a GFP model chromophore in a quadrupole ion trap*, *International Journal of Mass Spectrometry* **308**, 155 (2011).
- [100] T. Tanabe, M. Saito, and K. Noda, *Relaxation of green fluorescent protein chromophore anion observed by photodissociation in an electrostatic storage ring*, *European Physical Journal D* **62**, 191 (2011).
- [101] J. Rajput, D. B. Rahbek, L. H. Andersen, T. Rocha-Rinza, O. Christiansen, K. B. Bravaya, A. V. Erokhin, A. V. Bochenkova, K. M. Solntsev, J. Dong, J. Kowalik, L. M. Tolbert, M. A. Petersen, and M. B. Nielsen, *Photoabsorption studies of neutral green fluorescent protein model chromophores in vacuo*, *Physical Chemistry Chemical Physics* **11**, 9996 (2009).
- [102] A. V. Bochenkova, *Private Communication*.
- [103] Y. Toker (2012).